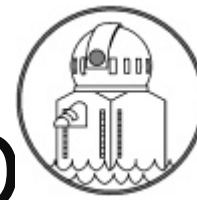


THE NEAR-INFRARED IMAGING SPECTROPOLARIMETER



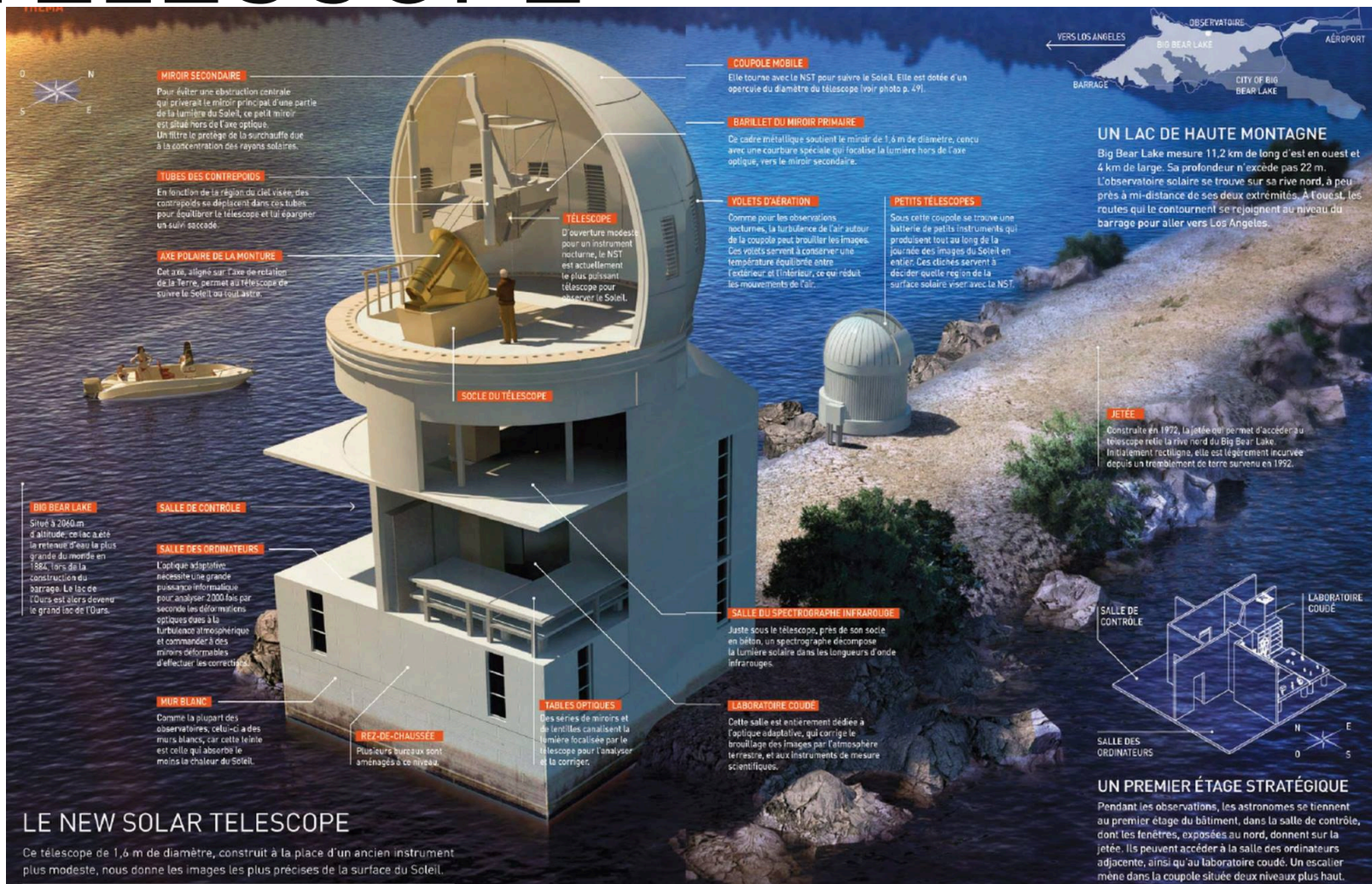
NJIT
New Jersey's Science &
Technology University
THE EDGE IN KNOWLEDGE

Kwangsu Ahn (安洸洸)
Big Bear Solar Observatory

10/31/2018
Kunming, China



THE GOODE SOLAR TELESCOPE



MIROIR SECONDAIRE

Pour éviter une obstruction centrale qui priverait le miroir principal d'une partie de la lumière du Soleil, ce petit miroir est placé hors de l'axe optique. Un litra le préleve de la surface due à la concentration des rayons solaires.

TUBES DES CONTREPOIDS

En fonction de la région du ciel visée, des contrepois se déplacent dans ces tubes pour équilibrer le télescope et lui épargner un suivi saccadé.

AXE POLAIRE DE LA MONTURE

Cet axe, aligné sur l'axe de rotation de la Terre, permet au télescope de suivre le Soleil au tout astr.

TÉLESCOPE

D'ouverture modeste pour un instrument nocturne, le NST est actuellement le plus puissant télescope pour observer le Soleil.

COUPOLE MOBILE

Elle tourne avec le NST pour suivre le Soleil. Elle est dotée d'un opercule du diamètre du télescope (voir photo p. 49).

BARILLET DU MIROIR PRIMAIRE

Le cadre métallique soutient le miroir de 1,6 m de diamètre, tenu avec une courbure spéciale qui focalise la lumière hors de l'axe optique, vers le miroir secondaire.

VOILETS D'AÉRATION

Comme pour les observations nocturnes, la turbulence de l'air autour de la coupole peut brouiller les images. Des voilets servent à conserver une température équilibrée entre l'extérieur et l'intérieur, ce qui réduit les mouvements de l'air.

PETITS TÉLESCOPES

Sous cette coupole se trouve une batterie de petits instruments qui produisent tout au long de la journée des images du Soleil en entier. Ces clichés servent à décider quelle région de la surface solaire viser avec le NST.

UN LAC DE HAUTE MONTAGNE

Big Bear Lake mesure 11,2 km de long d'est en ouest et 4 km de large. Sa profondeur n'excède pas 22 m. L'observatoire solaire se trouve sur sa rive nord, à peu près à mi-distance de ses deux extrémités. À l'ouest, les routes qui le contournent se rejoignent au niveau du barrage pour aller vers Los Angeles.

JETÉE

Construite en 1972, la jetée qui permet d'accéder au télescope relie la rive nord du Big Bear Lake. Initialement rectiligne, elle est légèrement incurvée depuis un tremblement de terre survenu en 1992.

BIG BEAR LAKE

Situé à 2060 m d'altitude, ce lac fait la réputation d'être la réserve d'eau la plus grande du monde en 1884, lors de la construction du barrage. Le lac de 10 ans est alors devenu le grand lac de l'Ours.

SALLE DE CONTRÔLE

L'optique adaptative nécessite une grande puissance informatique pour analyser 2000 fois par seconde les déformations optiques dues à la turbulence atmosphérique et commander à des miroirs déformables d'effectuer les corrections.

SALLE DES ORDINATEURS

Plusieurs bureaux sont aménagés à ce niveau.

MUR BLANC

Comme la plupart des observatoires, celui-ci a des murs blancs, car cette teinte est celle qui absorbe le moins la chaleur du Soleil.

REF-DE-CHAUSSEE

Plusieurs bureaux sont aménagés à ce niveau.

SOCLE DU TÉLESCOPE

TABLES OPTIQUES

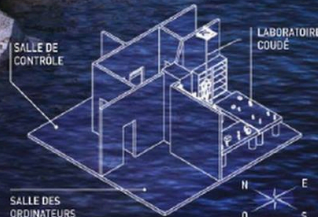
Des séries de miroirs et de lentilles canalisent la lumière focalisée par le télescope pour l'analyser et la corriger.

SALLE DU SPECTROGRAPHE INFRAROUGE

Juste sous le télescope, près de son socle en béton, un spectrographe décompose la lumière solaire dans les longueurs d'onde infrarouges.

LABORATOIRE COUDÉ

Cette salle est entièrement dédiée à l'optique adaptative, qui corrige le brouillage des images par l'atmosphère terrestre, et aux instruments de mesure scientifiques.

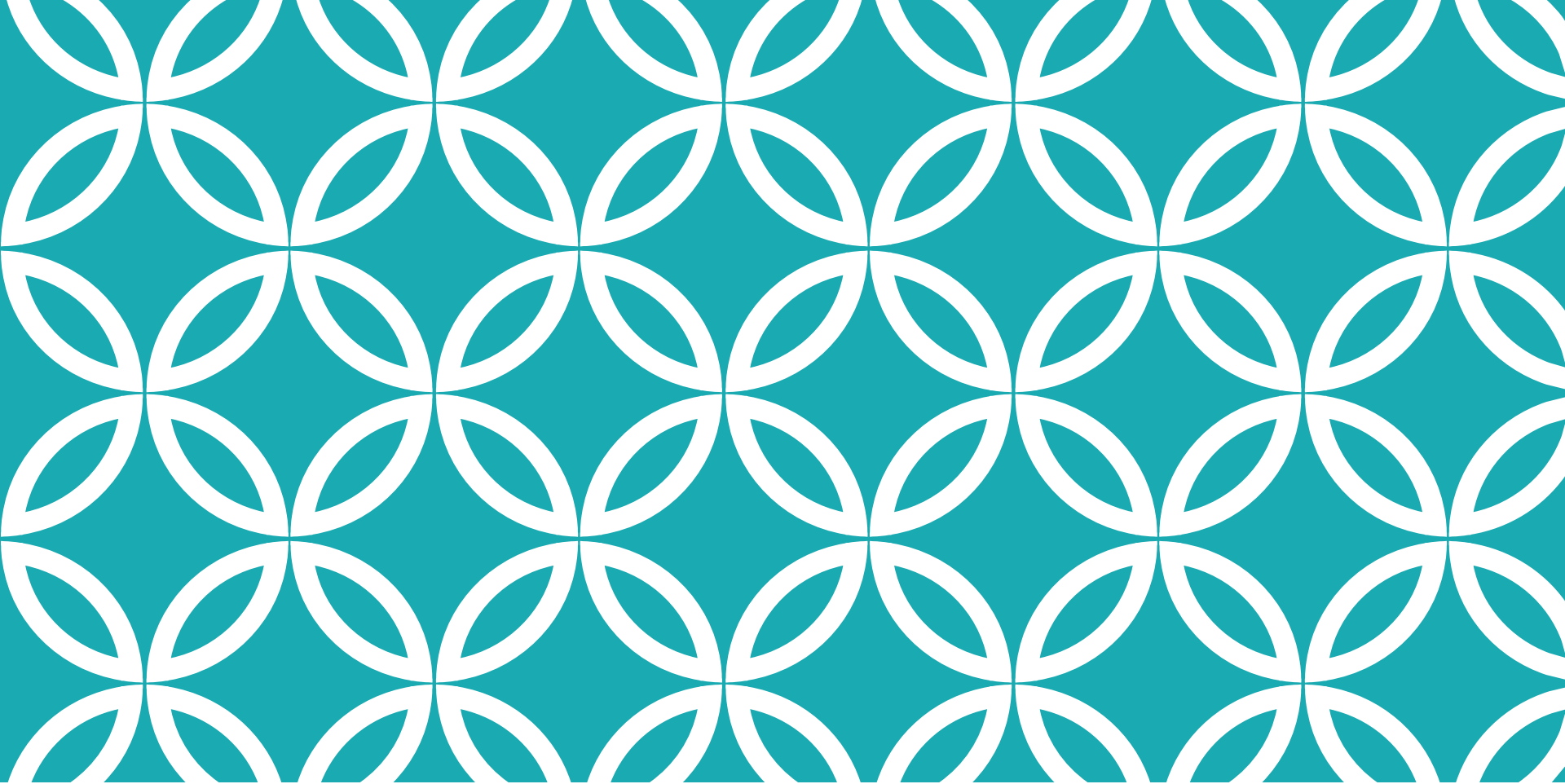


UN PREMIER ÉTAGE STRATÉGIQUE

Pendant les observations, les astronomes se tiennent au premier étage du bâtiment, dans la salle de contrôle, dont les fenêtres, exposées au nord, donnent sur la jetée. Ils peuvent accéder à la salle des ordinateurs adjacente, ainsi qu'au laboratoire coudé. Un escalier mène dans la coupole située deux niveaux plus haut.

LE NEW SOLAR TELESCOPE

Ce télescope de 1,6 m de diamètre, construit à la place d'un ancien instrument plus modeste, nous donne les images les plus précises de la surface du Soleil.



POLARIMETRY BASICS



ELECTRON IN MAGNETIC FIELD

Charged particles move in perpendicular to B field direction

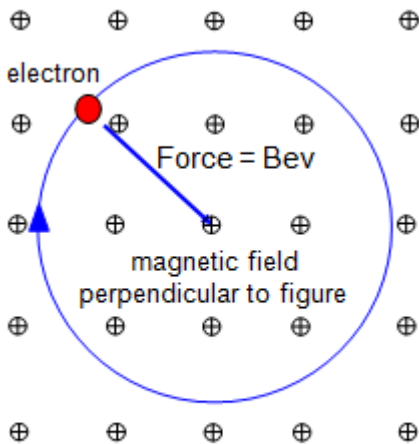
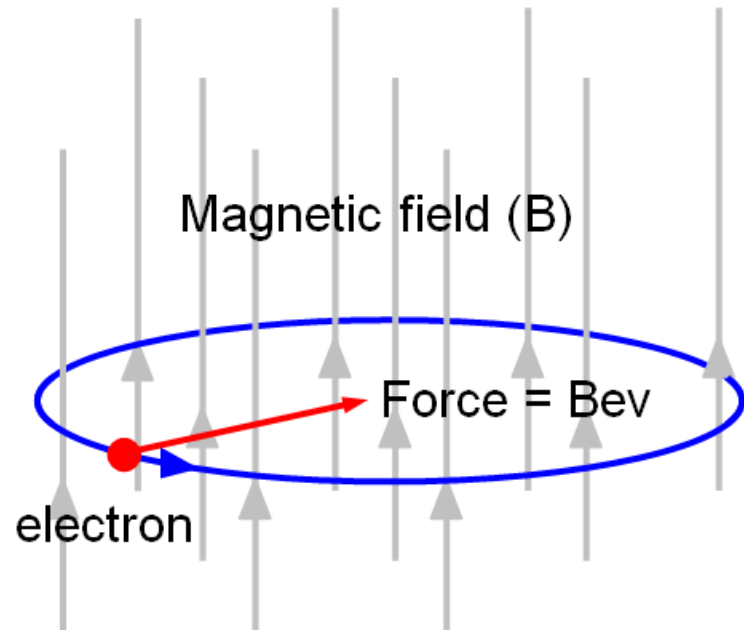


Figure 1



STOKES PARAMETERS

180 deg. Ambiguity in linear polarization \rightarrow x2 faster angular space

Stokes vectors for linearly polarized light

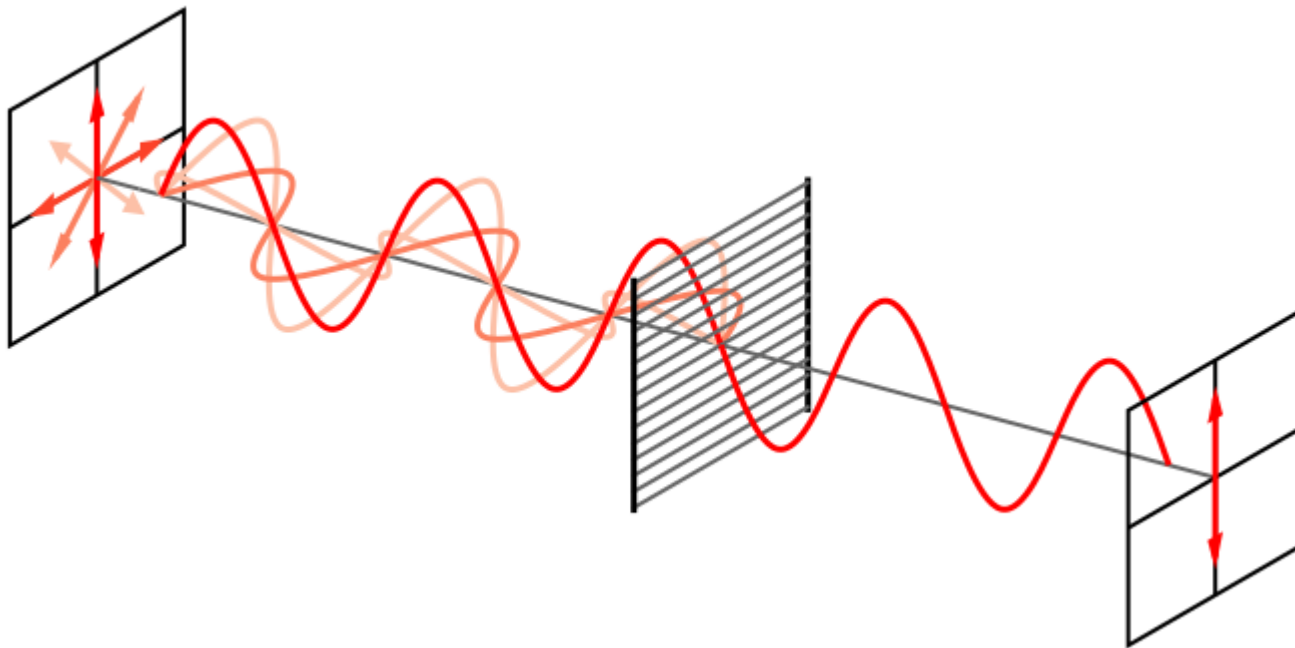
\leftrightarrow	\updownarrow	\nearrow	\nwarrow
+Q	-Q	+U	-U
$\theta = 0$	$\theta = \pi/2$	$\theta = \pi/4$	$\theta = -\pi/4$
$\begin{pmatrix} 1 \\ 1 \\ 0 \\ 0 \end{pmatrix}$	$\begin{pmatrix} 1 \\ -1 \\ 0 \\ 0 \end{pmatrix}$	$\begin{pmatrix} 1 \\ 0 \\ 1 \\ 0 \end{pmatrix}$	$\begin{pmatrix} 1 \\ 0 \\ -1 \\ 0 \end{pmatrix}$

Stokes vectors for circularly-polarized light

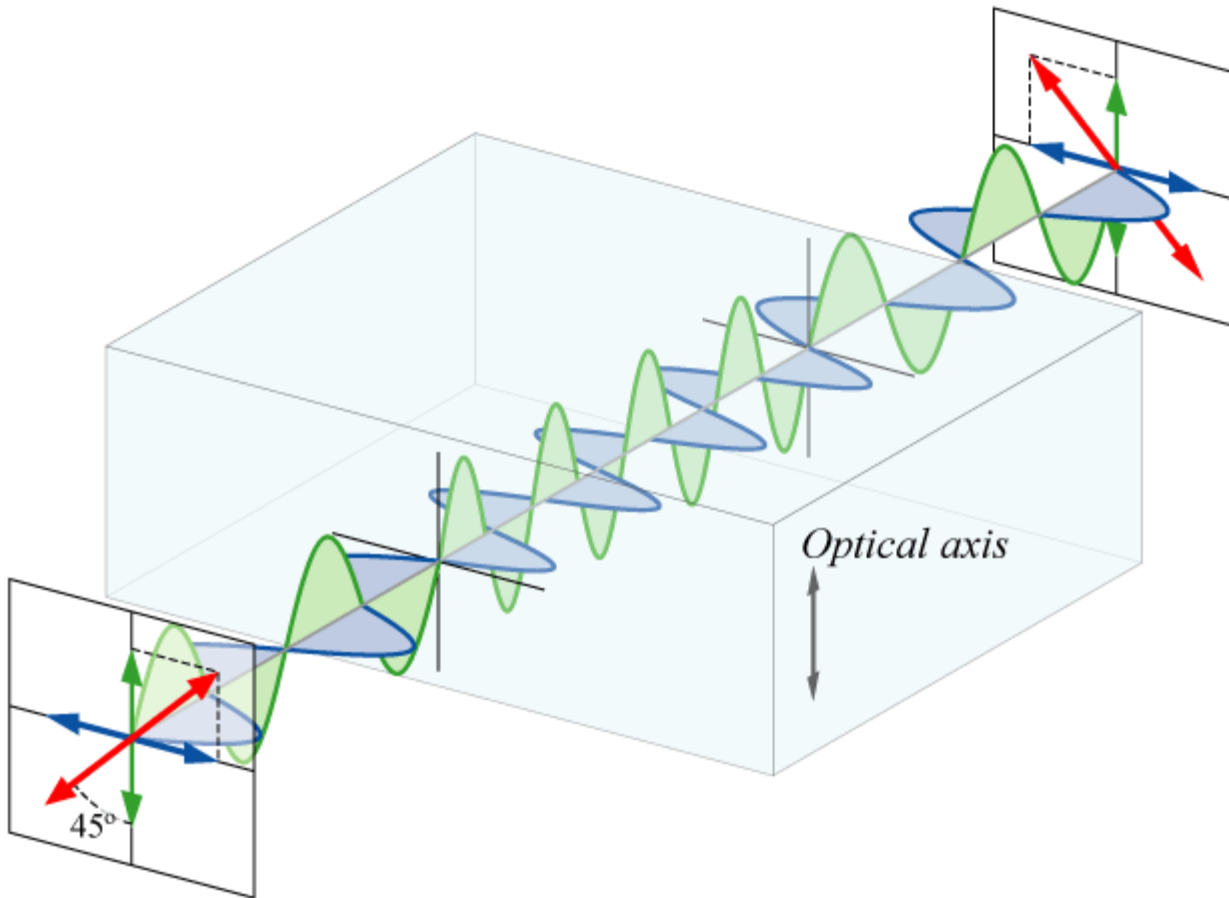
\odot	\otimes
+V	-V
Right Circular Polarization	Left Circular Polarization
$\begin{pmatrix} 1 \\ 0 \\ 0 \\ 1 \end{pmatrix}$	$\begin{pmatrix} 1 \\ 0 \\ 0 \\ -1 \end{pmatrix}$

LINEAR POLARIZER

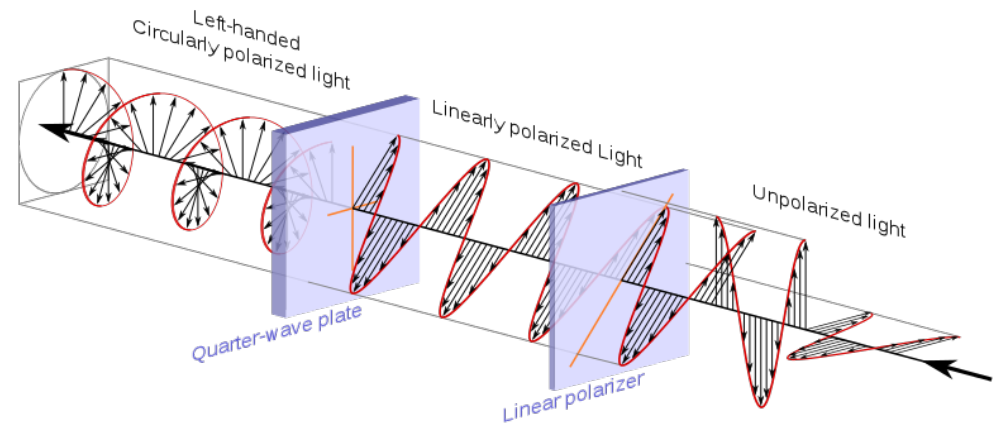
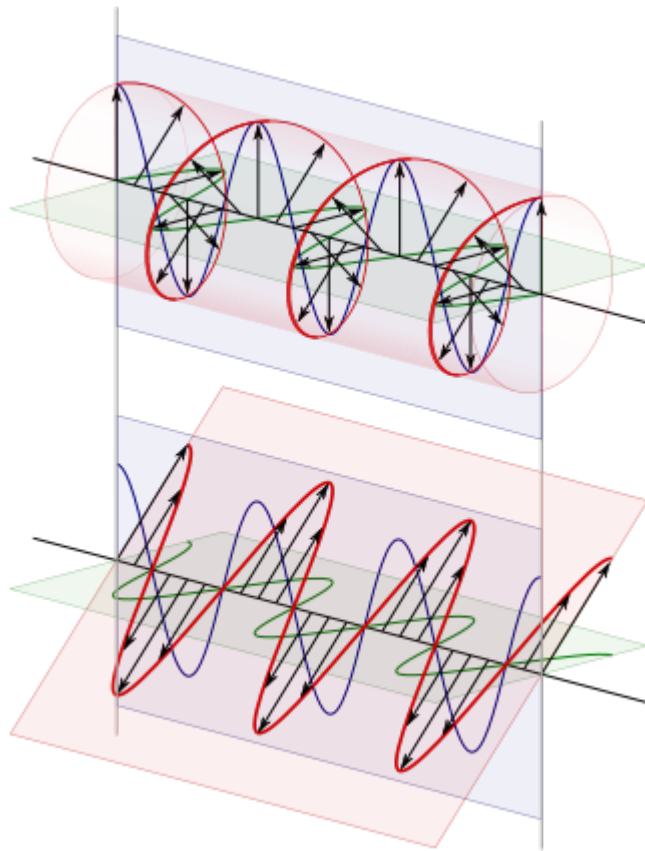
Absorbs one part of linear polarizations



RETARDER – $\frac{1}{2}$ WAVE PLATE

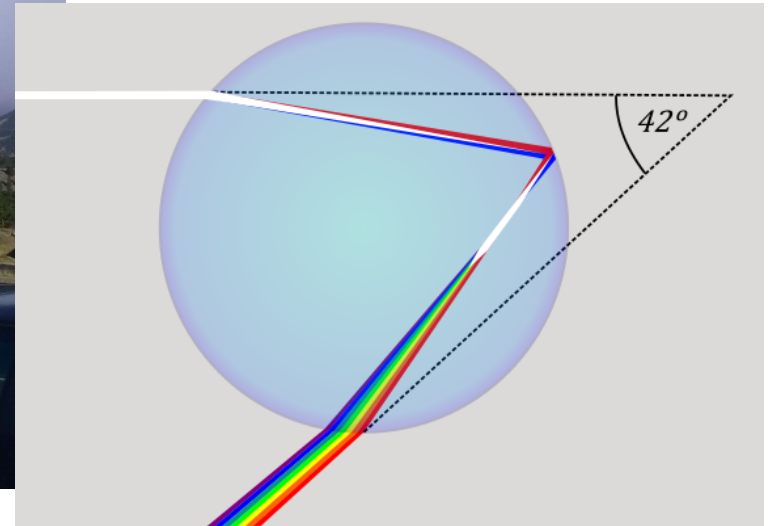


RETARDER - $\frac{1}{4}$ WAVE PLATE





RAINBOW



LINEAR POLARIZATION IN THE RAINBOW



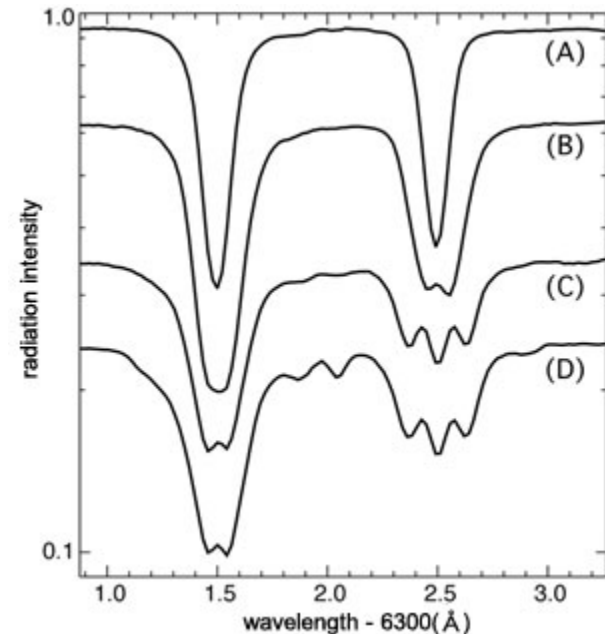
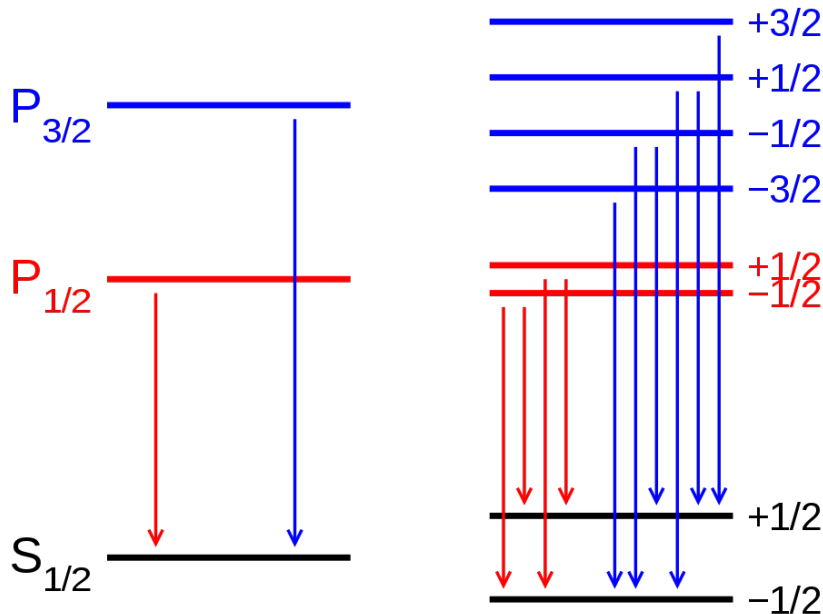
ZEEMAN E

Elements	wavelength	Landé g factor	$g\lambda$	Height
Fe I	6302.5	2.5	1.57	photosphere
Ca II	10830	1.22	1.32	chromosphere
Fe I	1.5648	3.0	4.69	photosphere

Table 3.1: A list of spectral lines that have strong Zeeman splitting (Bhatnagar, 2005).

A state where energy degeneracy is broken due to magnetic field

$$\Delta\lambda = \frac{e}{4\pi m} \frac{e c g \lambda^2 B}{c} = 46.7 \text{ m}\text{\AA} g \left(\frac{\lambda}{1\mu\text{m}} \right)^2 \left(\frac{B}{1000 \text{ G}} \right)$$

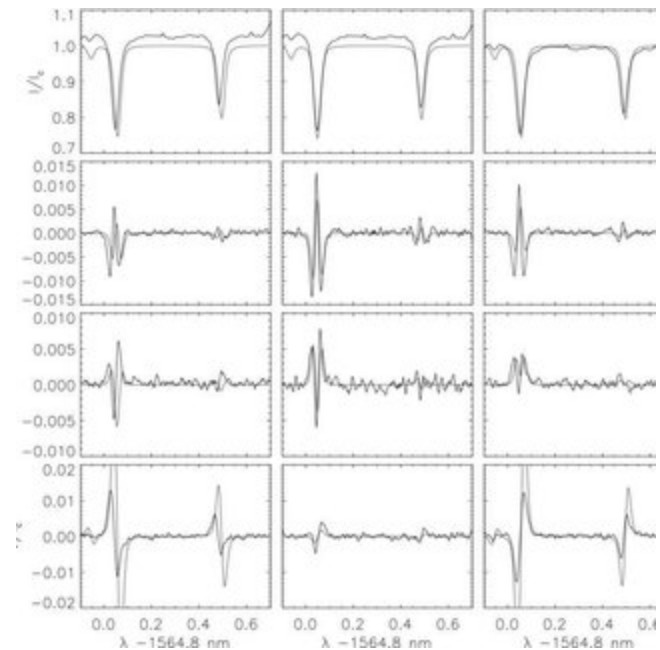
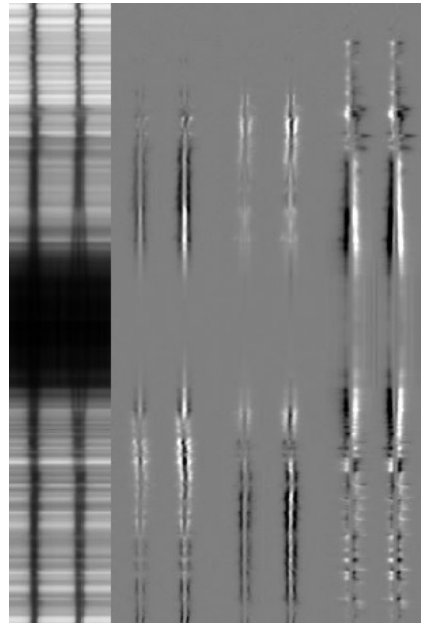


STOKES PROFILES (I, Q, U, V)

For a triplet,

Sigma component: circular polarization

Pi component: linear

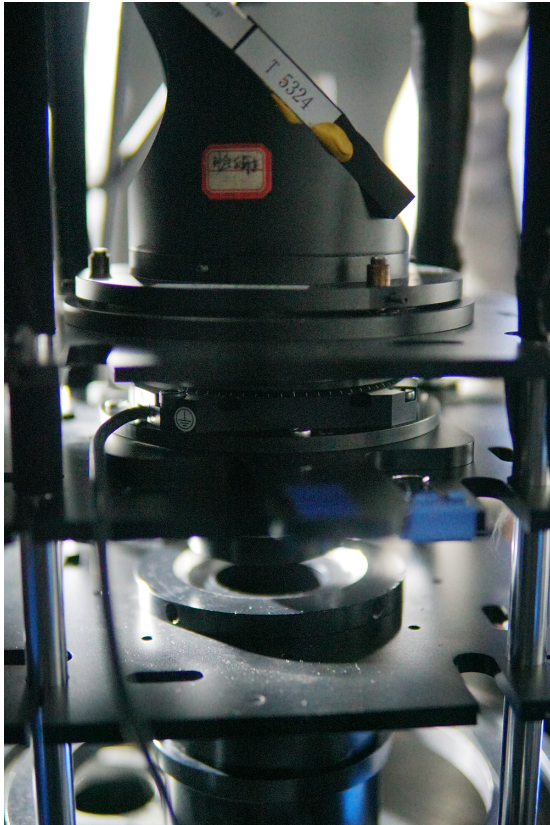


MUELLER MATRIX M

A 4 x 4 matrix that describes the polarization properties of the optics

- $(I' \ Q' \ U' \ V')^T = M (I \ Q \ U \ V)^T$
- If there are multiple optics in the beam train, M is the multiplication of Mueller matrix for each optical component.
 - $M = M_n \ M_{n-1} \ M_{n-2} \ \dots \ M_3 \ T$
- $(I \ Q \ U \ V)^T = M^{-1} (I' \ Q' \ U' \ V')^T$

NVST



TRADITIONAL SETUP



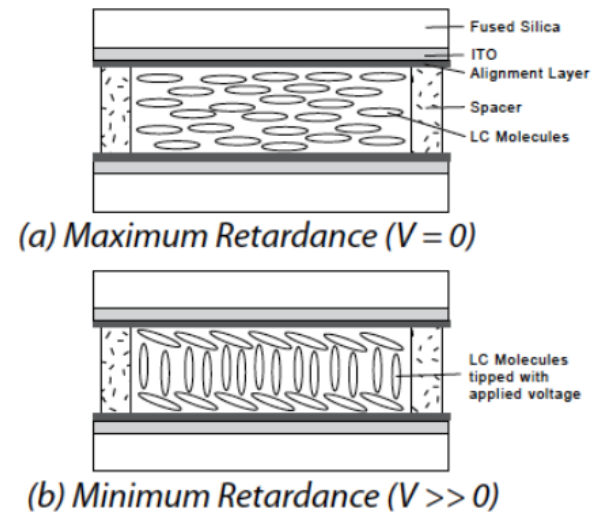
LVCR (LIQUID VARIABLE CRYSTAL RETARDER)

Voltage input to control retardation

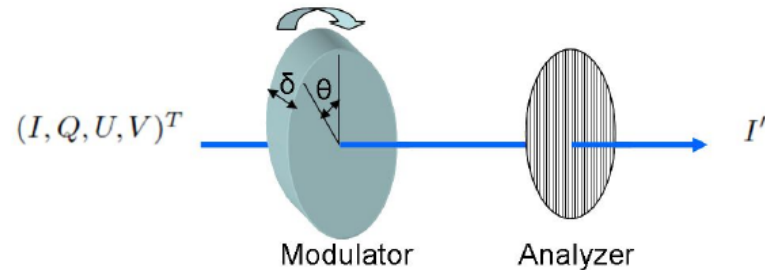
Relatively faster modulation

Non-linear retardation vs. voltage

Temperature sensitivity



MECHANICALLY-ROTATING MODULATOR



$$\mathbf{M}_{\text{ret}}(\delta) = \begin{pmatrix} 1 & 0 & 0 & 0 \\ 0 & 1 & 0 & 0 \\ 0 & 0 & \cos \delta & -\sin \delta \\ 0 & 0 & \sin \delta & \cos \delta \end{pmatrix},$$

$$\mathbf{R}(\theta) = \begin{pmatrix} 1 & 0 & 0 & 0 \\ 0 & \cos 2\theta & \sin 2\theta & 0 \\ 0 & -\sin 2\theta & \cos 2\theta & 0 \\ 0 & 0 & 0 & 1 \end{pmatrix}.$$

$$\mathbf{M}_{\text{mod}} = \mathbf{R}(-\theta)\mathbf{M}_{\text{ret}}(\delta)\mathbf{R}(\theta),$$

$$\mathbf{M}_{\text{mod}} = \begin{pmatrix} 1 & 0 & 0 & 0 \\ 0 & \cos^2 2\theta + \cos \delta \sin^2 2\theta & \cos 2\theta \sin 2\theta - \cos 2\theta \cos \delta \sin 2\theta & \sin 2\theta \sin \delta \\ 0 & \cos 2\theta \sin 2\theta - \cos 2\theta \cos \delta \sin 2\theta & \cos \delta \cos^2 2\theta + \sin^2 2\theta & -\cos 2\theta \sin \delta \\ 0 & -\sin 2\theta \sin \delta & \cos 2\theta \sin \delta & \cos \delta \end{pmatrix}.$$

$$\mathbb{M}_{\text{ana}} = \frac{1}{2} \begin{pmatrix} p_x^2 + p_y^2 & p_x^2 - p_y^2 & 0 & 0 \\ p_x^2 - p_y^2 & p_x^2 + p_y^2 & 0 & 0 \\ 0 & 0 & 2p_x p_y & 0 \\ 0 & 0 & 0 & 2p_x p_y \end{pmatrix} \simeq \frac{1}{2} \begin{pmatrix} 1 & 1 & 0 & 0 \\ 1 & 1 & 0 & 0 \\ 0 & 0 & 0 & 0 \\ 0 & 0 & 0 & 0 \end{pmatrix}.$$

$$I' = \frac{1}{2} \left(I + \frac{Q}{2} ((I + \cos \delta) + (1 - \cos \delta) \cos 4\theta) + \frac{U}{2} (1 - \cos \delta) \sin 4\theta - V \sin \delta \sin 2\theta \right),$$

Double check the sign conventions

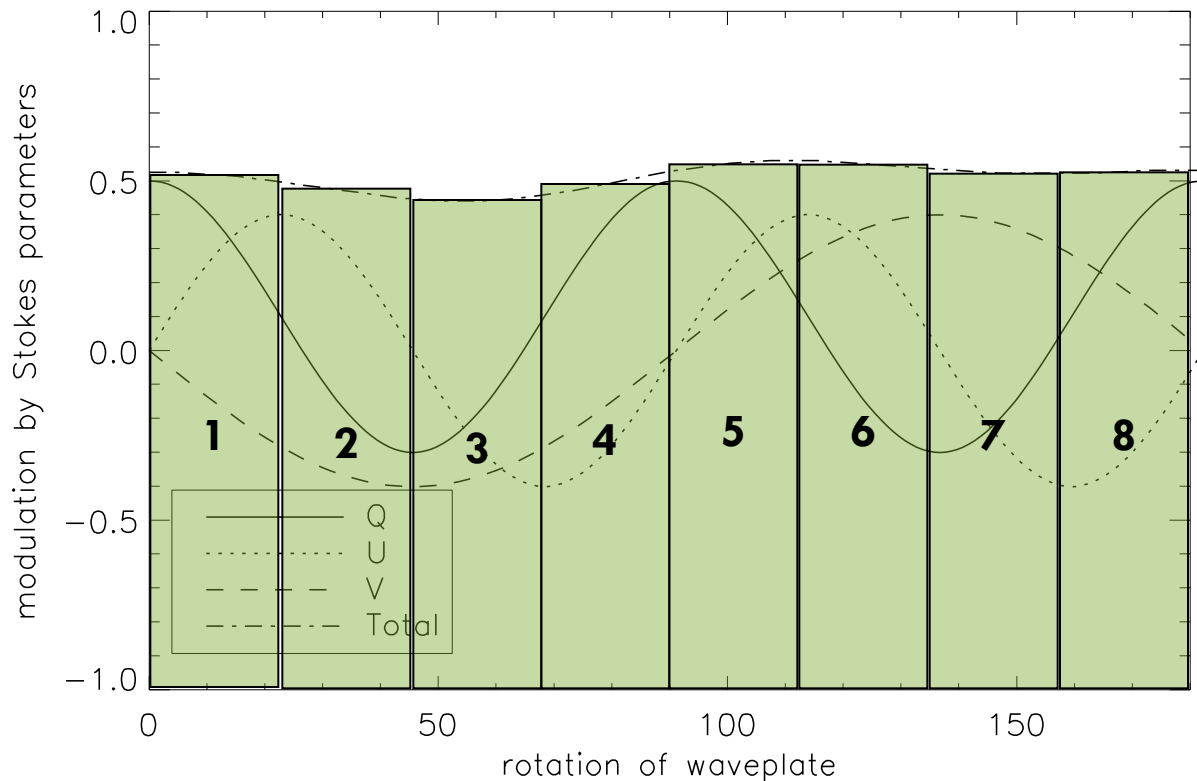
$$\mathbb{M}_{\text{mod}} = \begin{pmatrix} 1 & 0 & 0 & 0 \\ 0 & \cos^2 2\theta + \cos \delta \sin^2 2\theta & \cos 2\theta \sin 2\theta - \cos 2\theta \cos \delta \sin 2\theta & \sin 2\theta \sin \delta \\ 0 & \cos 2\theta \sin 2\theta - \cos 2\theta \cos \delta \sin 2\theta & \cos \delta \cos^2 2\theta + \sin^2 2\theta & -\cos 2\theta \sin \delta \\ 0 & -\sin 2\theta \sin \delta & \cos 2\theta \sin \delta & \cos \delta \end{pmatrix}.$$

MODULATION

Modulated intensity after passing through analyzer:

- $\delta=127$ gives the same modulation amplitude for Q, U, V.
- Dividing modulation by 8 segments then applying different combination gives different Stokes parameters.

$$I' = \frac{1}{2} \left(I + \frac{Q}{2} ((I + \cos \delta) + (1 - \cos \delta) \cos 4\theta) + \frac{U}{2} (1 - \cos \delta) \sin 4\theta - V \sin \delta \sin 2\theta \right)$$



Parameter	Combination
I	1+2+3+4+5+6+7+8
Q	1-2-3+4+5-6-7+8
U	1+2-3-4+5+6-7-8
V	-1-2-3-4+5+6+7+8

SYNCHRONIZATION BETWEEN MODULATOR & CAMERA

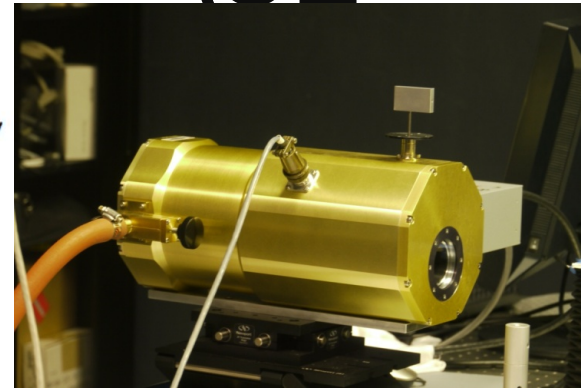
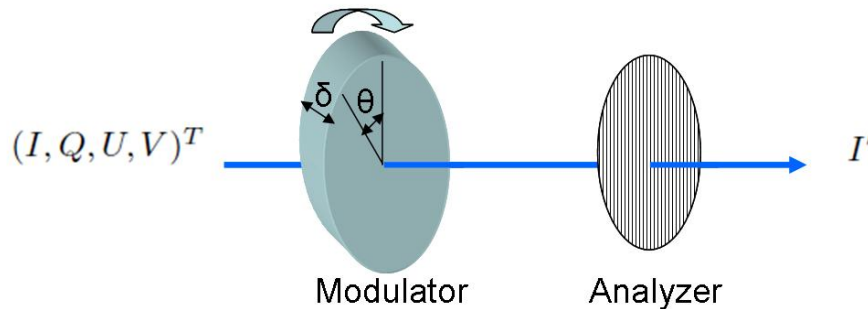
Modulation is a function of time, 8 segments mean 8 frames from camera.

- The timing of the camera exposure should match with the rotation of the modulator.

Controlling modulator from the camera signal is difficult.

Triggering camera exposure from the modulator gives exposure timing error.

COMPROMISE: MATCHING MODULATION RATE, RANDOMIZING PHASE



The modulator rotates at a fixed rate, the camera's exposure time is determined at the same rate.

The camera continuously takes image when it is on. Modulator initializes when software initializes

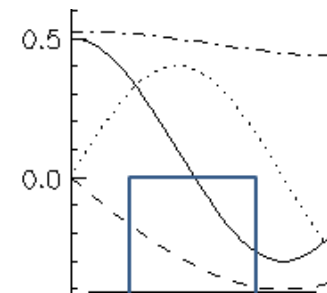
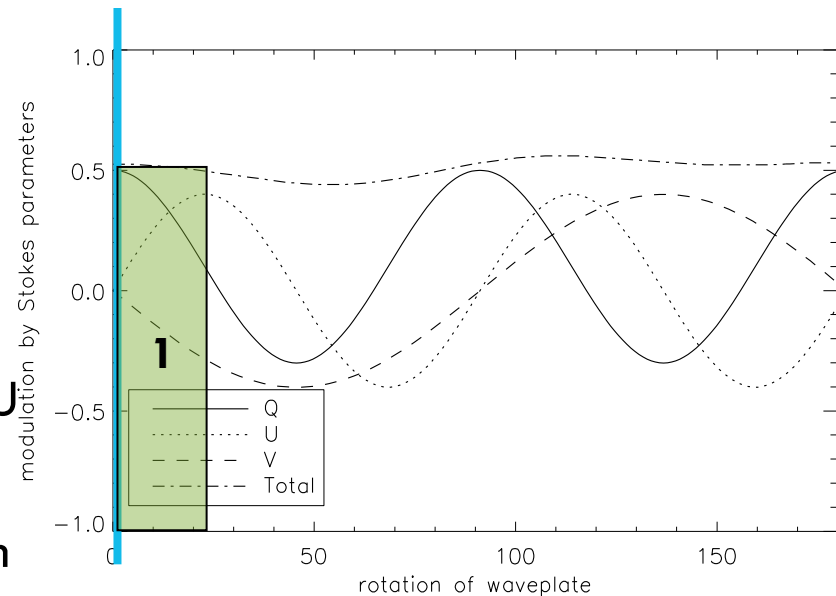
- The phase of the modulator is random w.r.t. the framing.

TROUBLES WITH RANDOM PHASE OFFSET

Simply combining the 8 segments by the combination rule assumes that the 1st frame start at 0 modulation angle. Random phase offset moves the starting position to any angle between 0 & 360°.

Q & U mixture: Q, U have the same period but different phase. With offset $\phi=22.5^\circ$, U signal will look as Q signal.

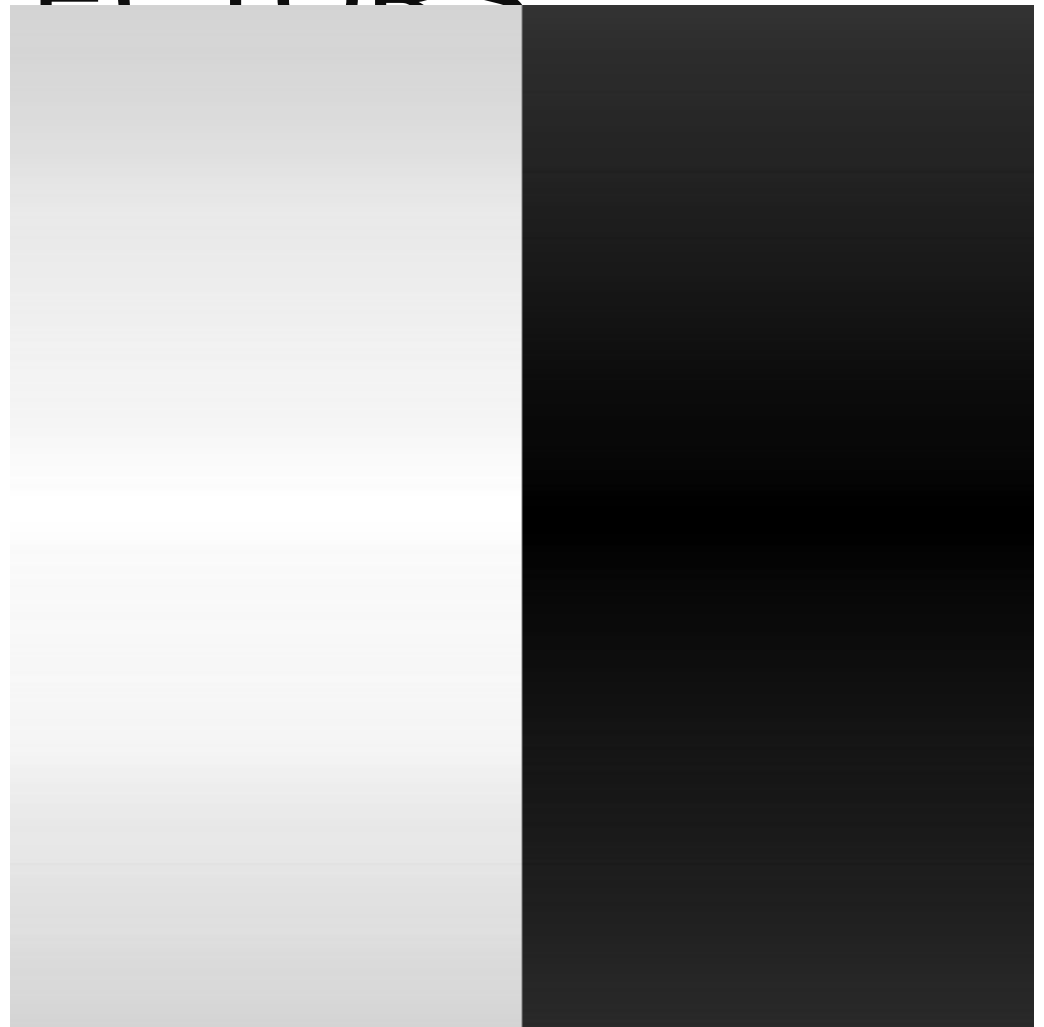
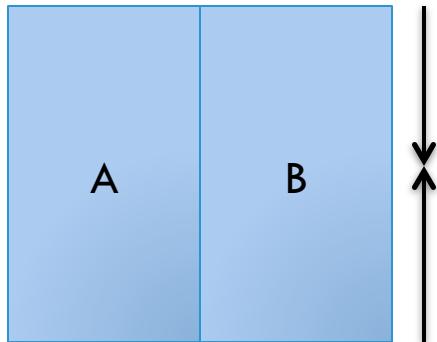
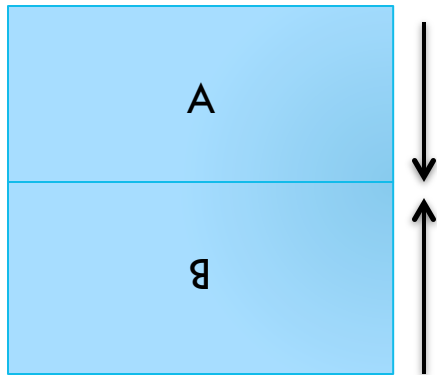
Each segment from pure Q, U, V modulation only have single sign. With a random phase, some segment will contain both signs. → signal reduction by cancellation



READOUT TIMING ISSUE



RIPPLE READOUT OF CMOS DETECTORS



CROSSTALK & EFFICIENCY LOSS DUE TO ϕ

Modulation signal

$$I' = \frac{1}{2} \left(I + \frac{Q}{2} ((I + \cos \delta) + (1 - \cos \delta) \cos 4\theta) + \frac{U}{2} (1 - \cos \delta) \sin 4\theta - V \sin \delta \sin 2\theta \right)$$

Segmentation

$$\int_0^{\frac{\pi}{8}} I' d\theta - \int_{\frac{\pi}{8}}^{\frac{\pi}{4}} I' d\theta - \int_{\frac{\pi}{4}}^{\frac{3\pi}{8}} I' d\theta + \int_{\frac{3\pi}{8}}^{\frac{\pi}{2}} I' d\theta + \int_{\frac{\pi}{2}}^{\frac{5\pi}{8}} I' d\theta - \int_{\frac{5\pi}{8}}^{\frac{3\pi}{4}} I' d\theta - \int_{\frac{3\pi}{4}}^{\frac{7\pi}{8}} I' d\theta + \int_{\frac{7\pi}{8}}^{\pi} I' d\theta = 0.8Q$$

With a random offset ϕ

- Q':

$$\int_{\phi}^{\frac{\pi}{8}+\phi} I' d\theta - \int_{\frac{\pi}{8}+\phi}^{\frac{\pi}{4}+\phi} I' d\theta - \int_{\frac{\pi}{4}+\phi}^{\frac{3\pi}{8}+\phi} I' d\theta + \int_{\frac{3\pi}{8}+\phi}^{\frac{\pi}{2}+\phi} I' d\theta + \int_{\frac{\pi}{2}+\phi}^{\frac{5\pi}{8}+\phi} I' d\theta - \int_{\frac{5\pi}{8}+\phi}^{\frac{3\pi}{4}+\phi} I' d\theta - \int_{\frac{3\pi}{4}+\phi}^{\frac{7\pi}{8}+\phi} I' d\theta + \int_{\frac{7\pi}{8}+\phi}^{\pi+\phi} I' d\theta = 0.8(Q \cos 4\phi - U \sin 4\phi)$$

- V':

$$-\int_{\phi}^{\frac{\pi}{8}+\phi} I' d\theta - \int_{\frac{\pi}{8}+\phi}^{\frac{\pi}{4}+\phi} I' d\theta - \int_{\frac{\pi}{4}+\phi}^{\frac{3\pi}{8}+\phi} I' d\theta - \int_{\frac{3\pi}{8}+\phi}^{\frac{\pi}{2}+\phi} I' d\theta + \int_{\frac{\pi}{2}+\phi}^{\frac{5\pi}{8}+\phi} I' d\theta + \int_{\frac{5\pi}{8}+\phi}^{\frac{3\pi}{4}+\phi} I' d\theta + \int_{\frac{3\pi}{4}+\phi}^{\frac{7\pi}{8}+\phi} I' d\theta + \int_{\frac{7\pi}{8}+\phi}^{\pi+\phi} I' d\theta = 0.8 V \cos 2\phi$$

RESTORING THE ORIGINAL SIGNAL

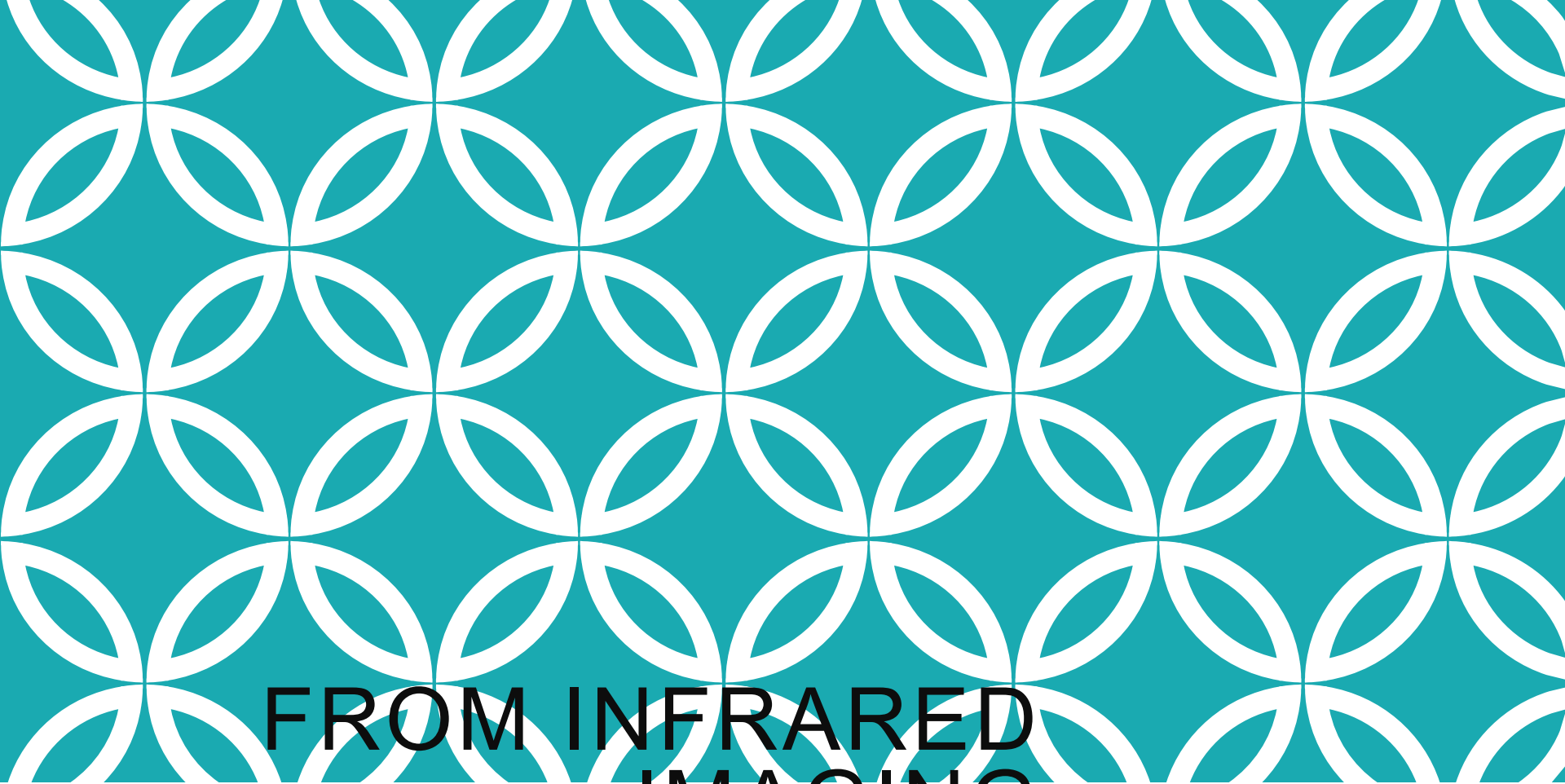
Restoration matrix

$$\begin{bmatrix} I \\ Q \\ U \\ V \end{bmatrix} = \begin{bmatrix} 1 & 0 & 0 & 0 \\ 0 & \cos 4\phi & \sin 4\phi & 0 \\ 0 & -\sin 4\phi & \cos 4\phi & 0 \\ 0 & 0 & 0 & \sec 2\phi \end{bmatrix} \begin{bmatrix} I' \\ Q' \\ U' \\ V' \end{bmatrix}$$

ϕ information is stored in a text file for every burst.

- If $|\phi| > 11.25^\circ$, the following sign convention table shifts accordingly so that $-11.25 \leq \phi < 11.25$.

Parameter	Camera 1	Camera 2
<i>I</i>	+++++	+++++
<i>Q</i>	+--++--	-++--++-
<i>U</i>	++--++--	--++--++
<i>V</i>	----++++	++++----



**FROM INFRARED
IMAGING
MAGNETOGRAPH
TO NEAR-INFRARED
IMAGING
SPECTROPOLARIMETRY**



INFRARED IMAGING MAGNETOGRAPH (IRIM)

Fabry-Perot based, wavelength
scanning magnetograph

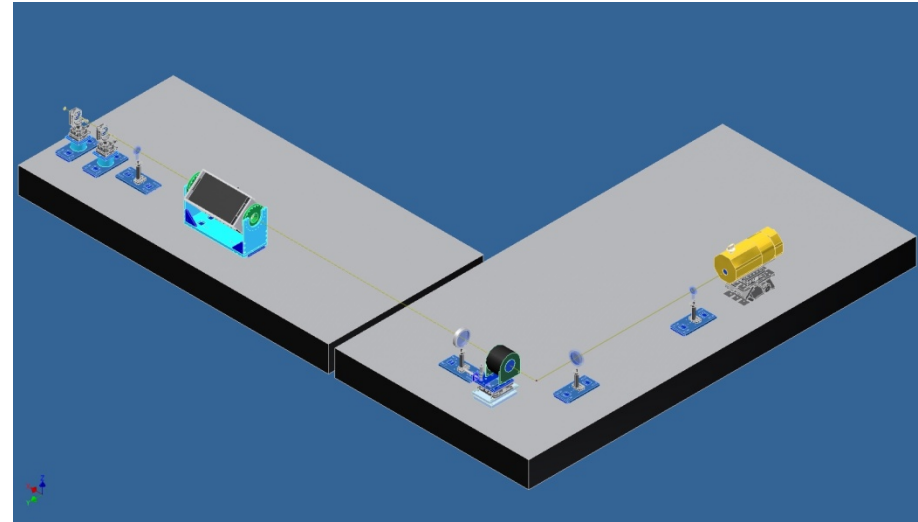
Spatial resolution: 0.2" at Fe I 1.56 μm

Bandwidth: 0.1 \AA

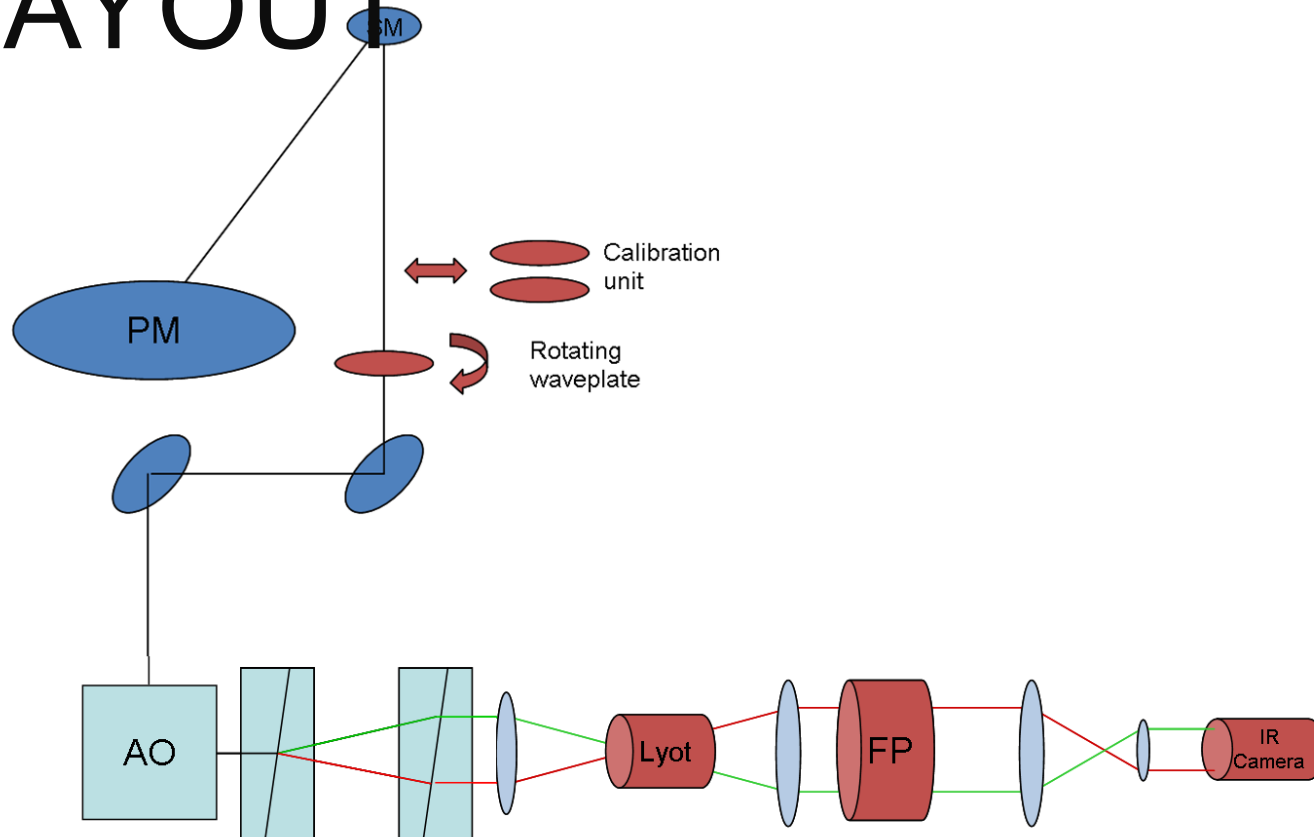
Temporal resolution: 50 secs

Dual-beam imaging

Field of view: 50" x 25"



IRIM (1ST GENERATION) LAYOUT



IRIM COMPONENTS

Modulator

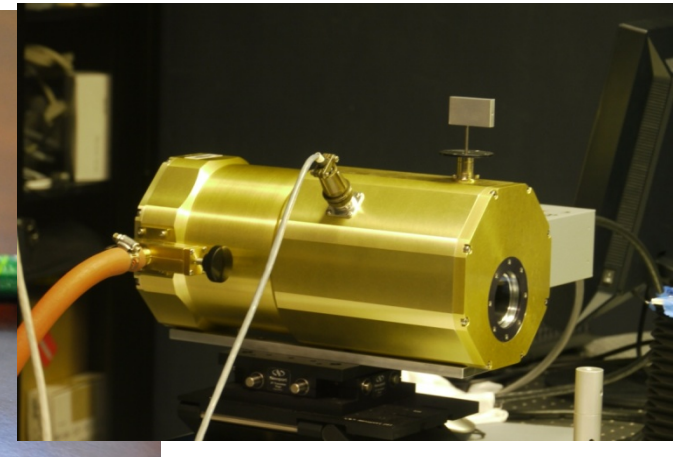
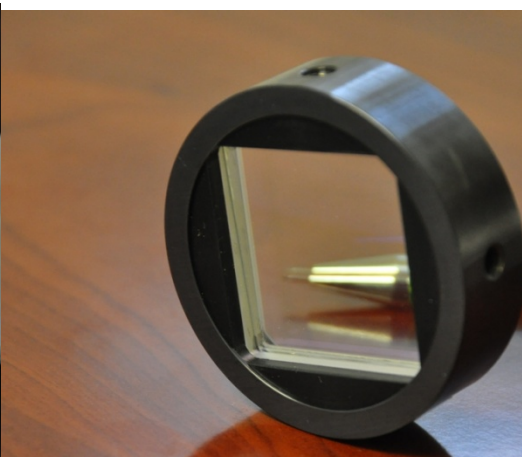
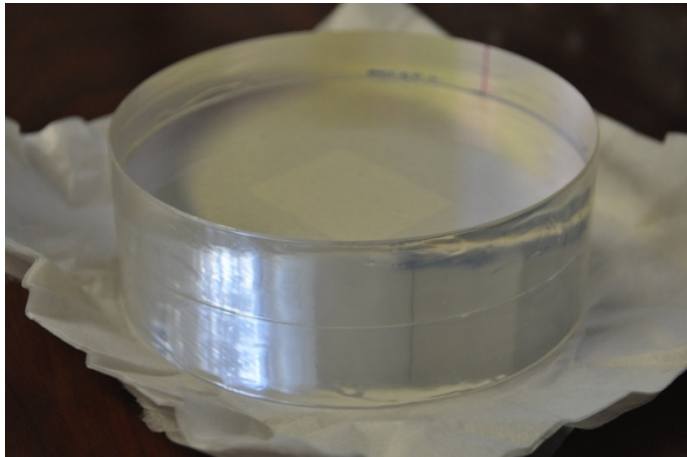
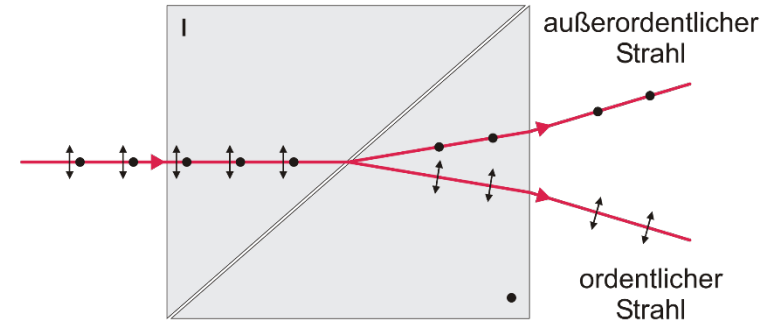
- Mechanically rotating birefringent polymer
- 5" aperture, 2" thickness

Analyzer

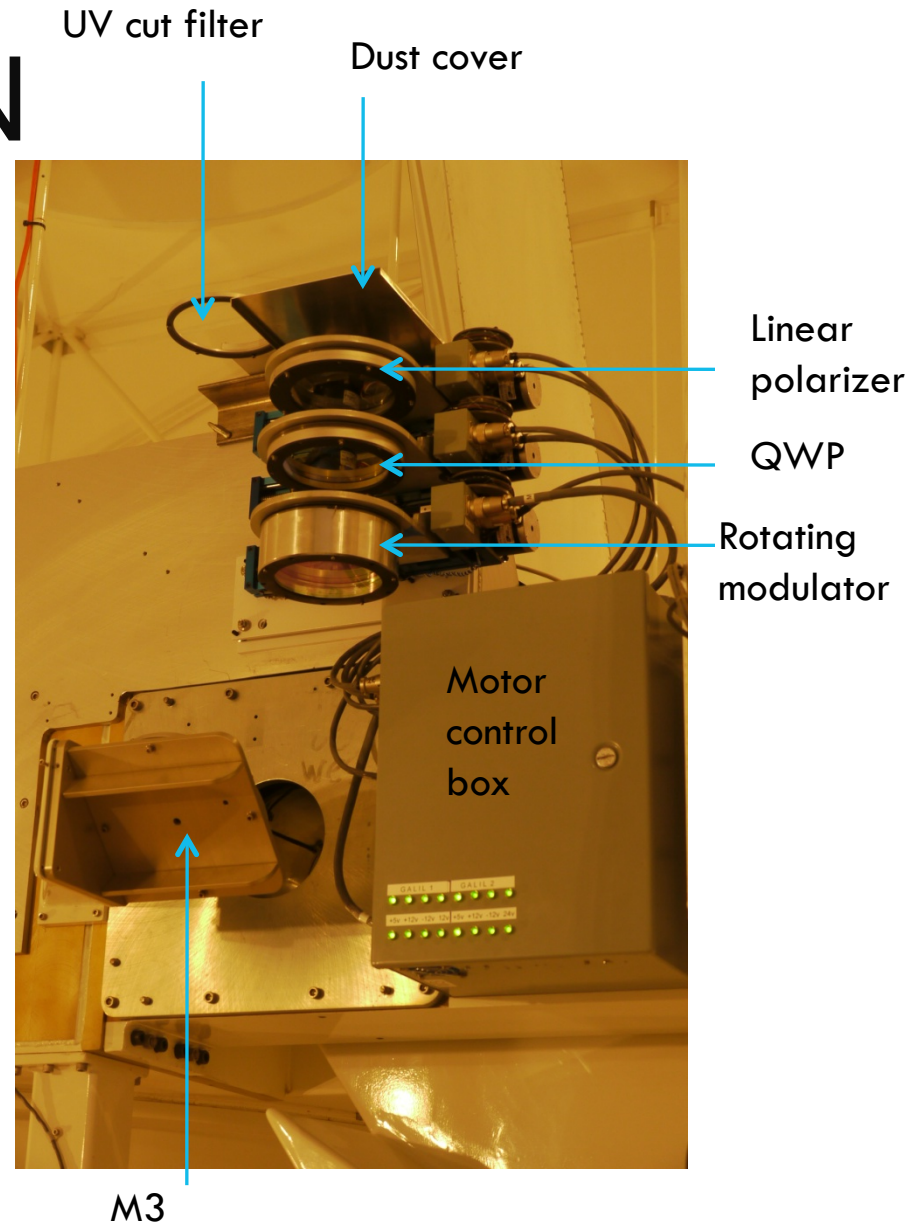
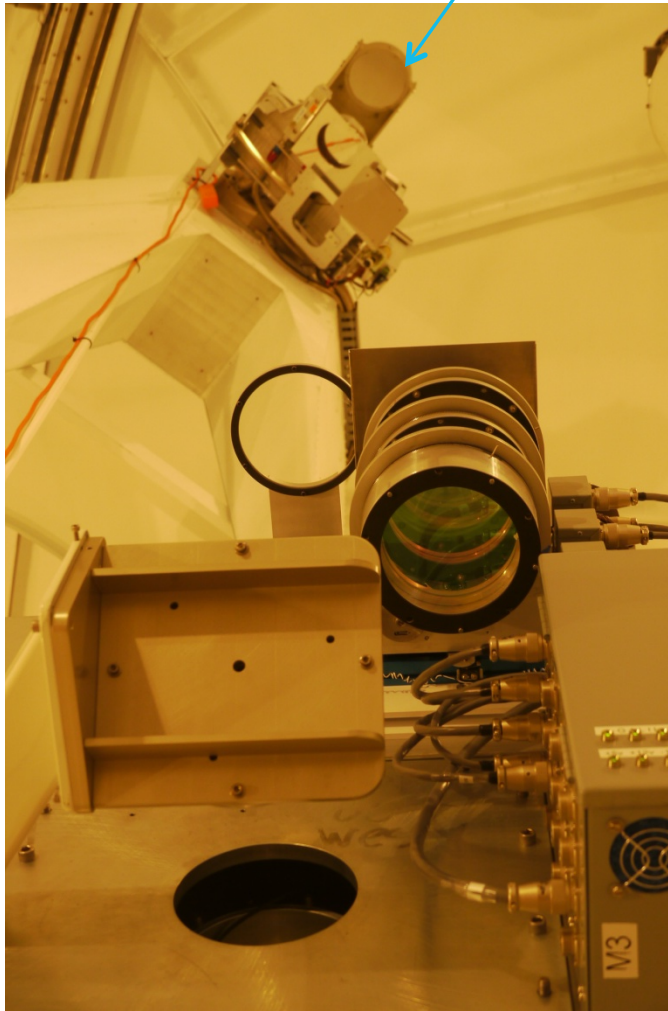
- Two Wollaston prisms (40 mm x 40 mm)

Camera

- CMOS camera w/ ripple readout
- Maximum 30 fps, optimal at 20 fps



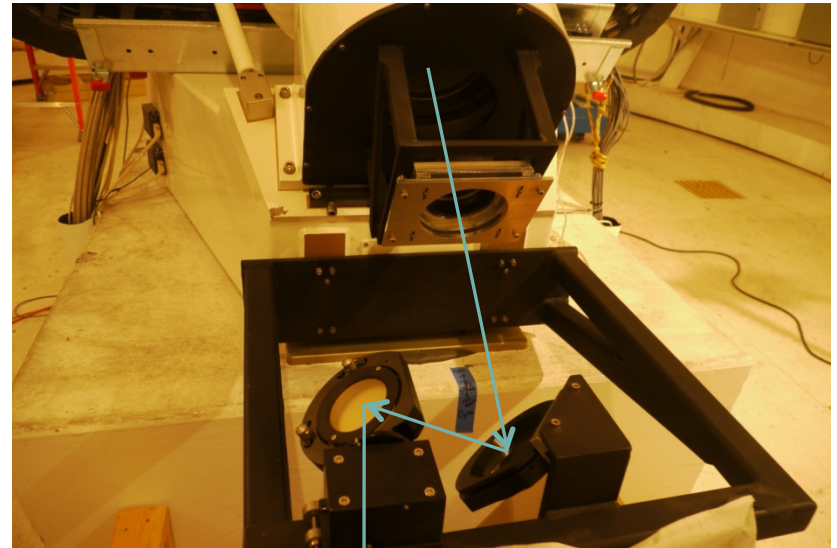
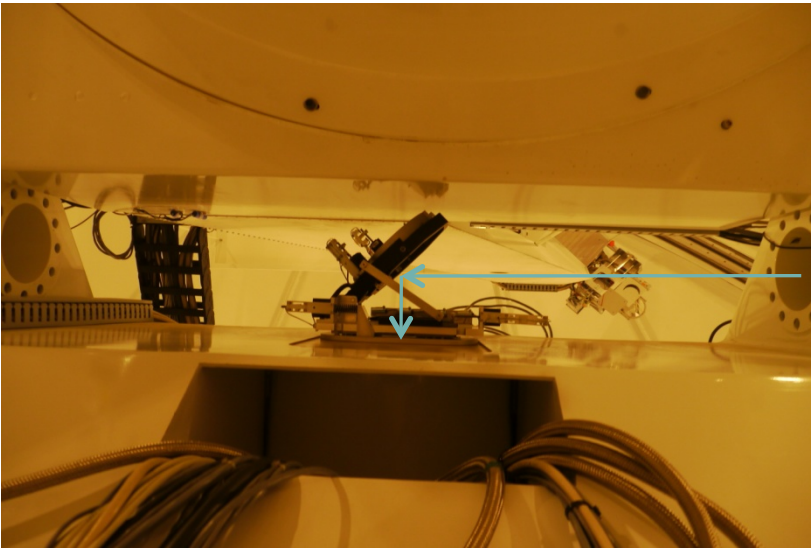
INSTALLATION



M4-M6

Dec rotation between M3 & M4

RA rotation between M4 & M5



IRIM BEAM PATHS

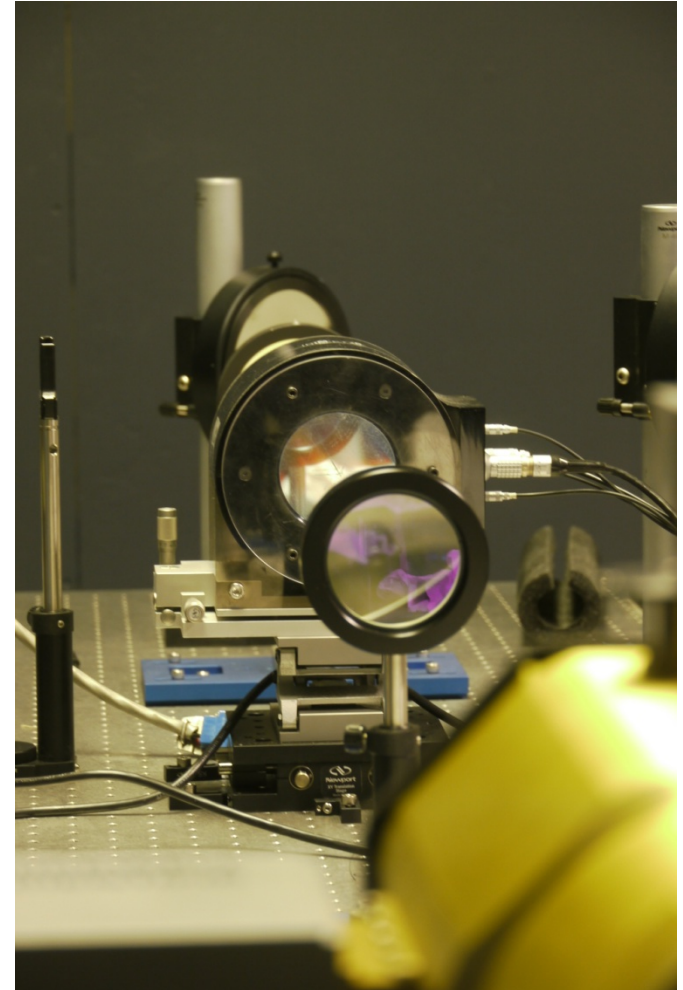
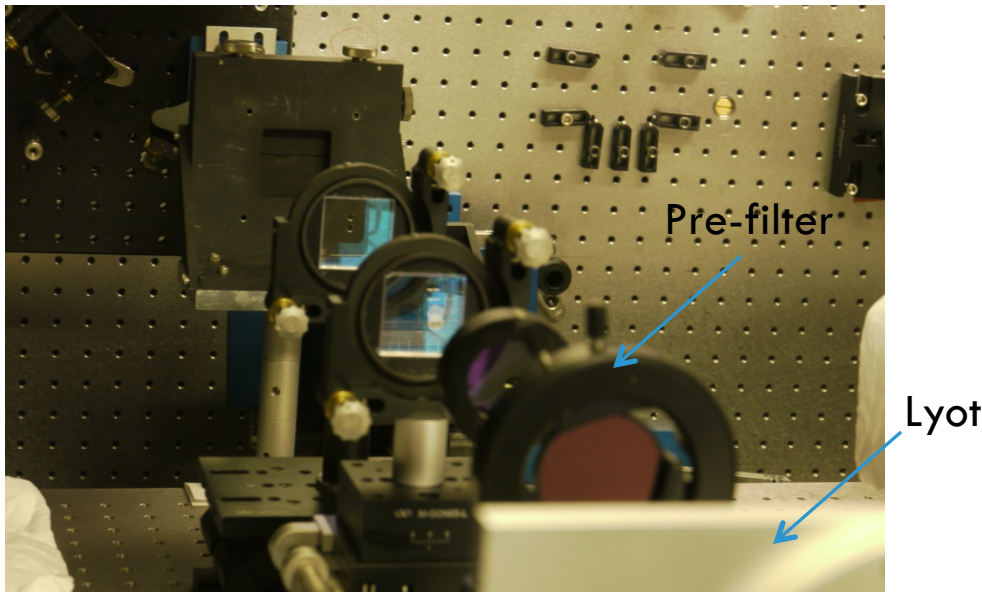
Two Wollaston prisms

Pre-filter: FWHM 25 Å

Lyot: FWHM 2.5 Å

- Tilted by ~ 45 deg. due to intrinsic linear polarizer
- Transmission: 0.1
- To be replaced to another F-P

F-P: FWHM 0.1 Å



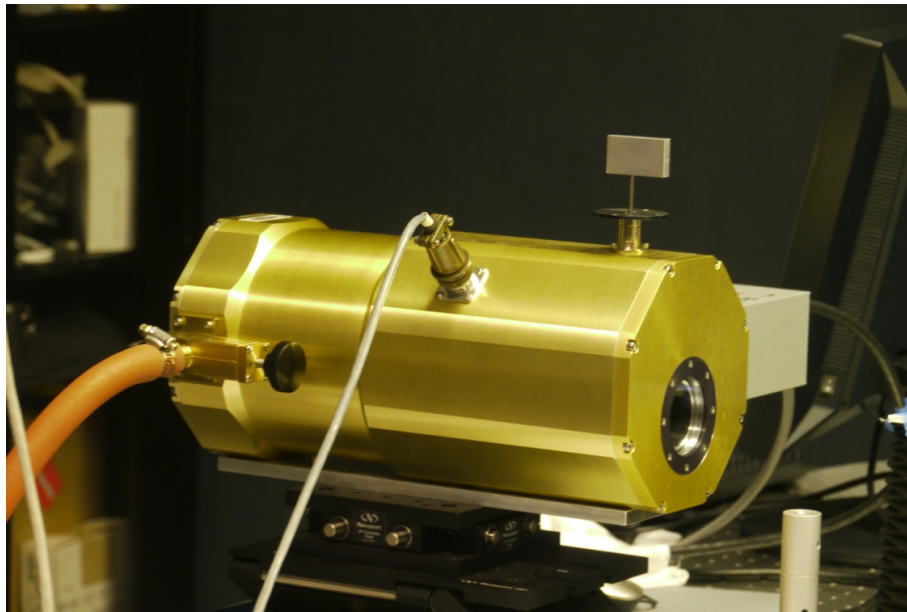
CAMERA

Manufacturer: Rockwell

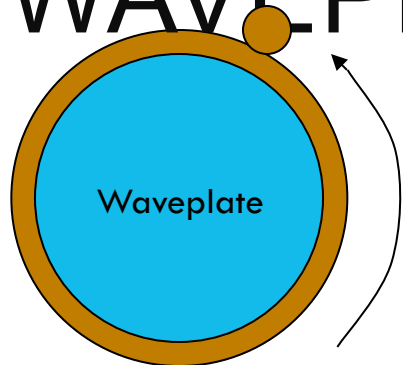
1024×1024, 14 bit HgCdTe CMOS

Max 30 fps

1k × 1k chip is divided by two halves to accommodate dual beams with different polarizations.



OPERATION OF WAVEPLATE & CAMERA



Waveplate rotates with 1 rps.

Camera is free running, collecting frames in the frame grabber.

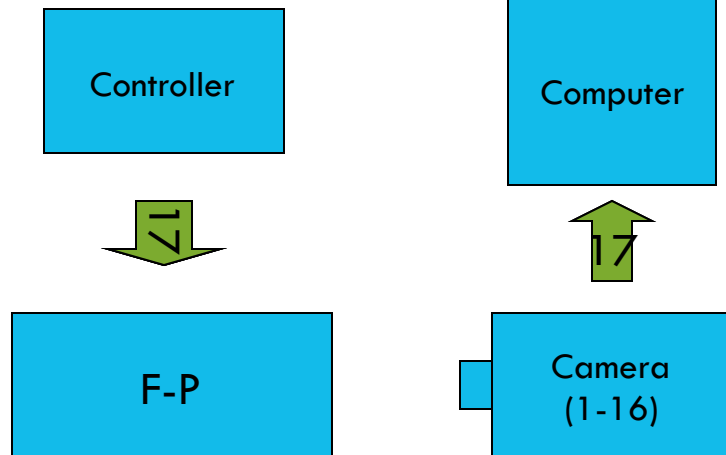
- 16 successive signals

After one rotation, wavelength tuning of F-P and data retrieval to computer occur.

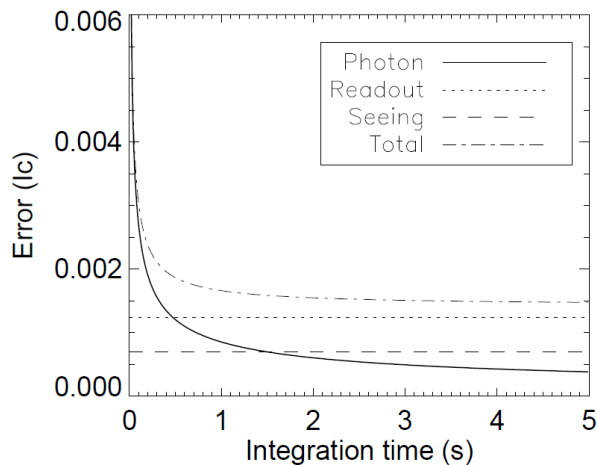
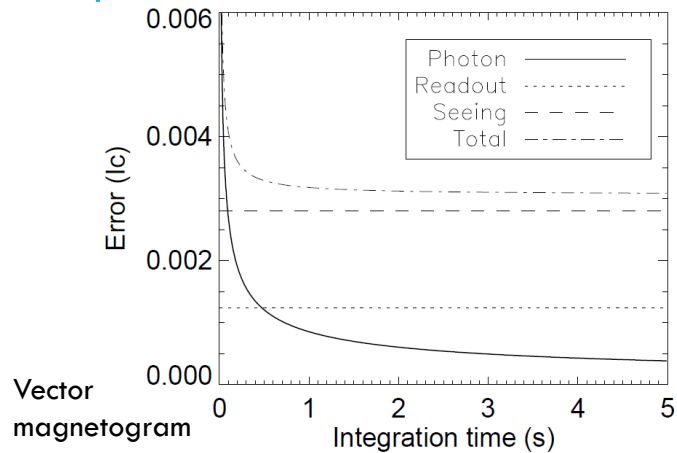
- 17th frame will be discarded.

From the 18th frame, the second burst begins.

13 wavelength sampling, 221 frames per burst



ERROR ESTIMATE



Stokes V only

Possible sources of noise

- Poisson noise
- Readout noise (75e- per frame)
- Seeing-induced crosstalk
- Instrumental residual crosstalk

Total error estimate

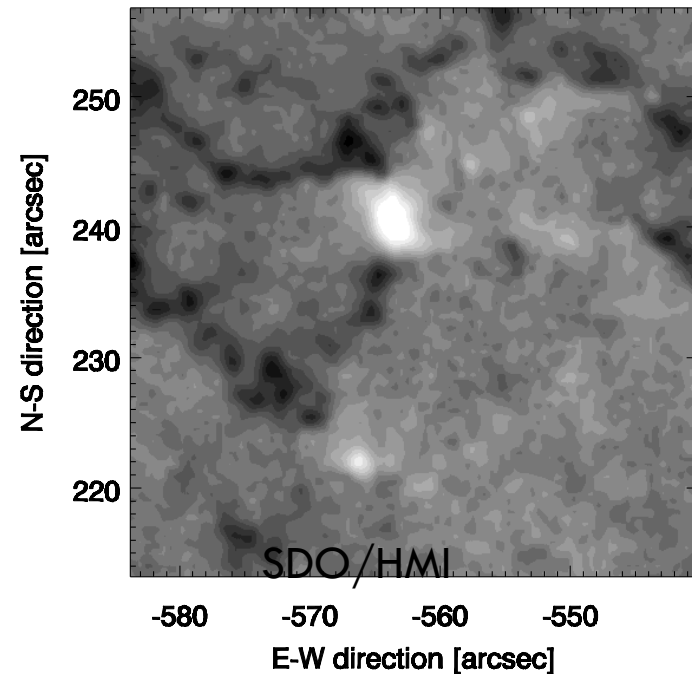
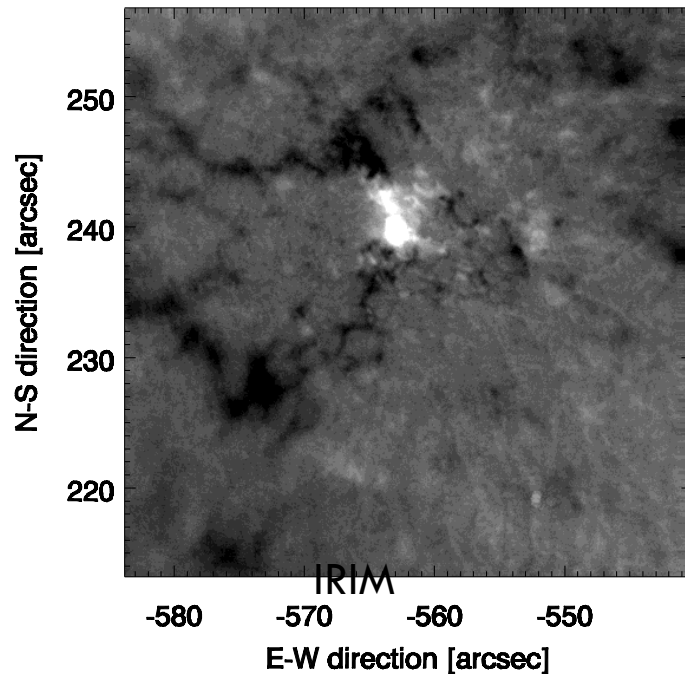
- 3×10^{-3} Ic for vector magnetogram (1 rps of waveplate rotation)
- 1.5×10^{-3} Ic for longitudinal field measurement (4 rps)

FIRST LIGHT

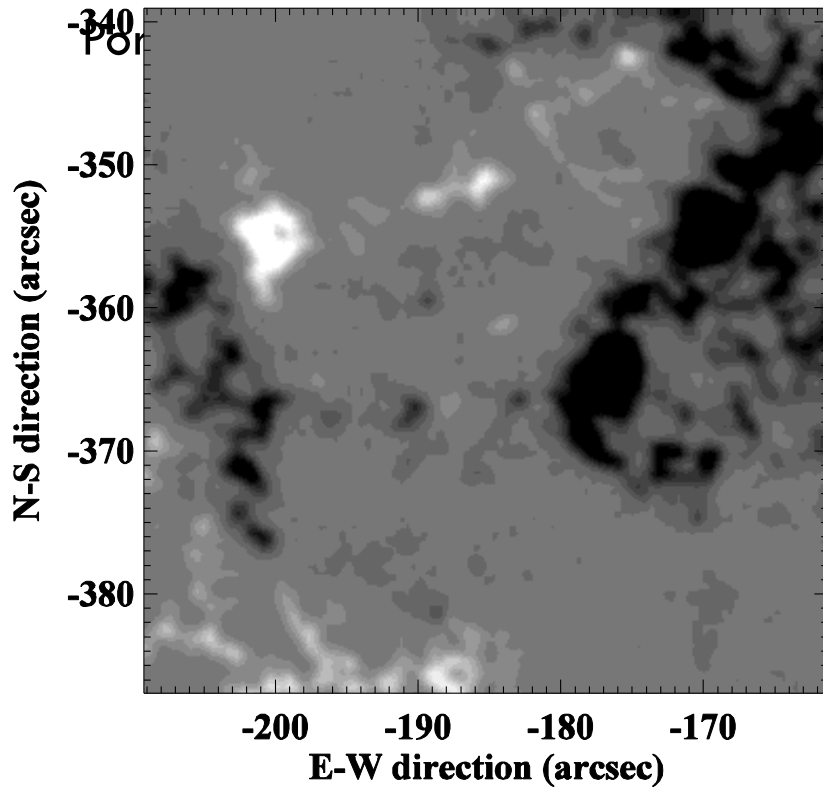
Under poor seeing, single beam, LCVRs

Exp: 90 ms

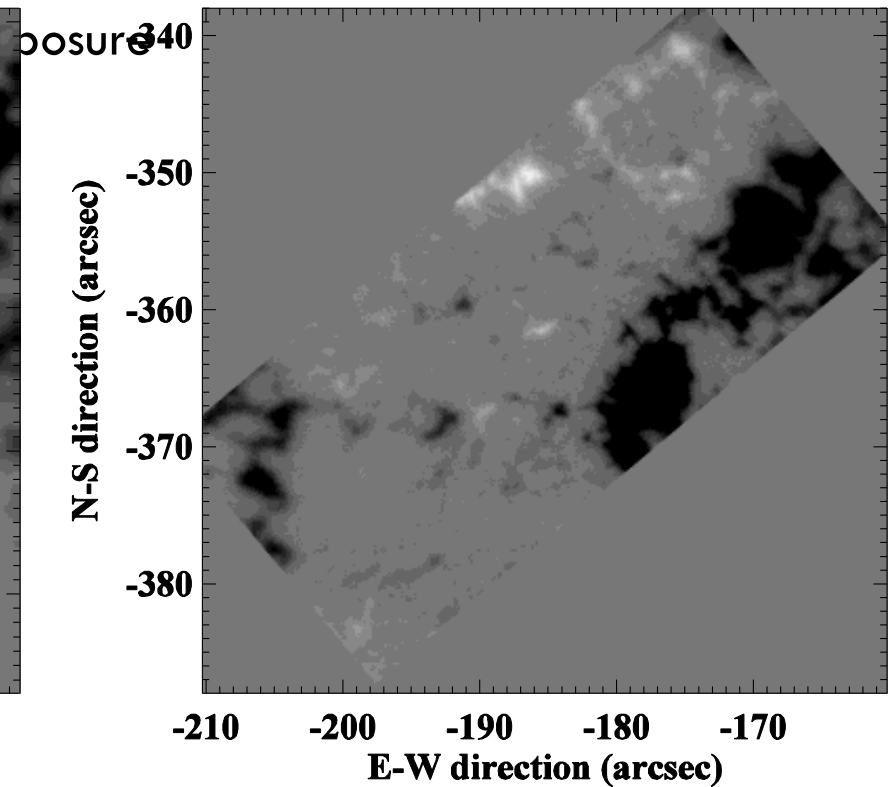
$$14/160 * 1.56/0.63 = 0.21$$



DUAL-BEAM TEST



SDO/HMI

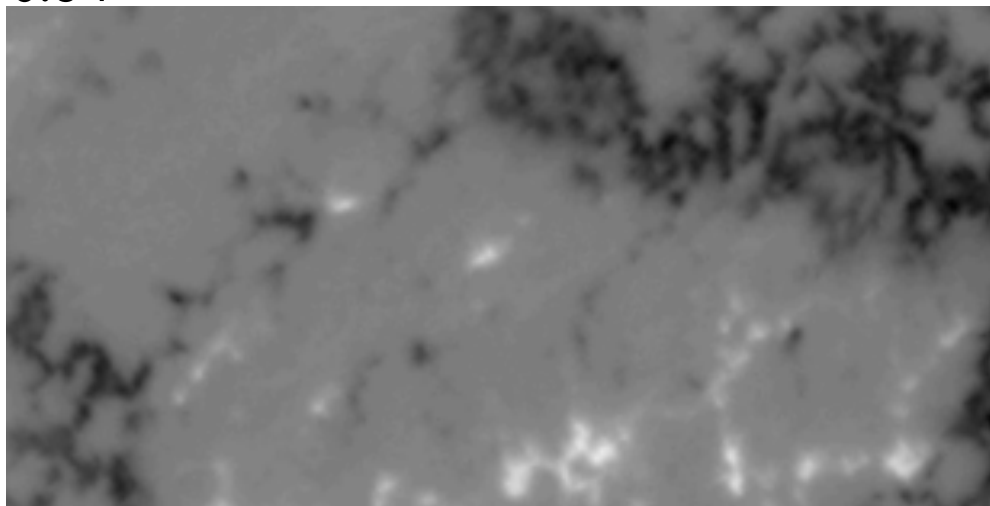


IRIM

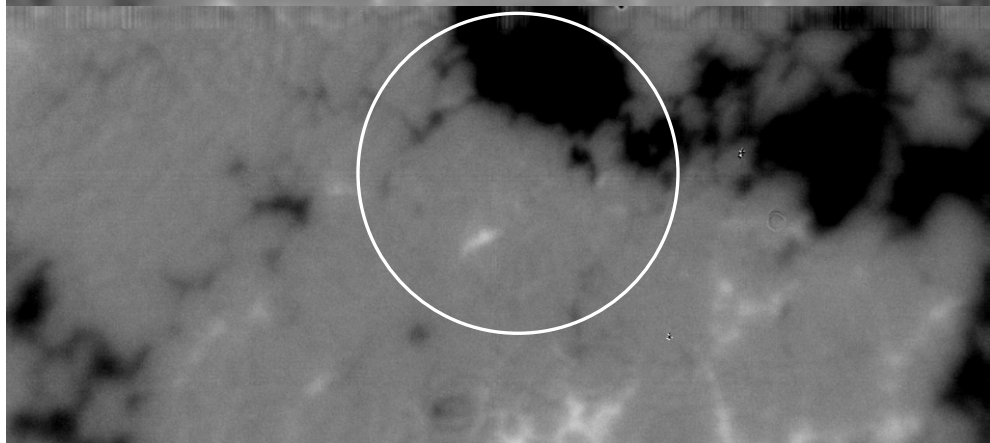


$$50/160 * 1.56/0.58 = 0.84$$

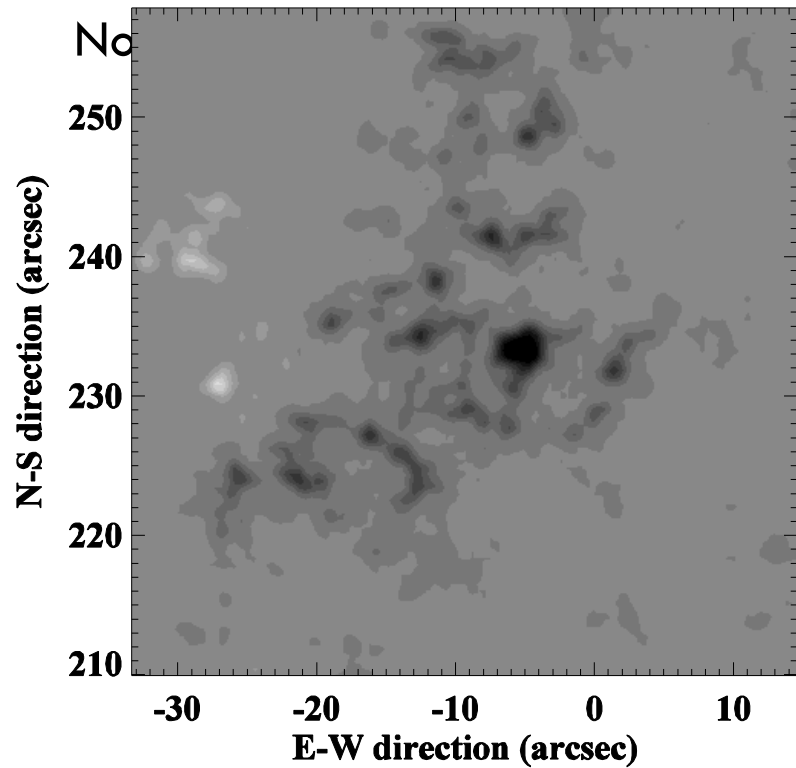
Hinode/FG



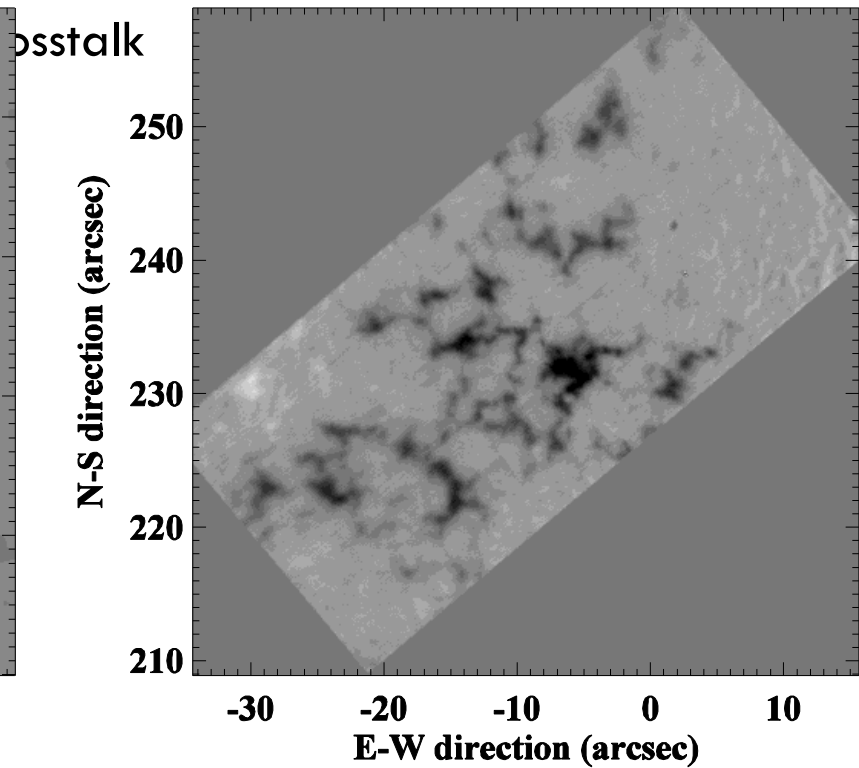
IRIM



PORE UNDER FAIR SEEING

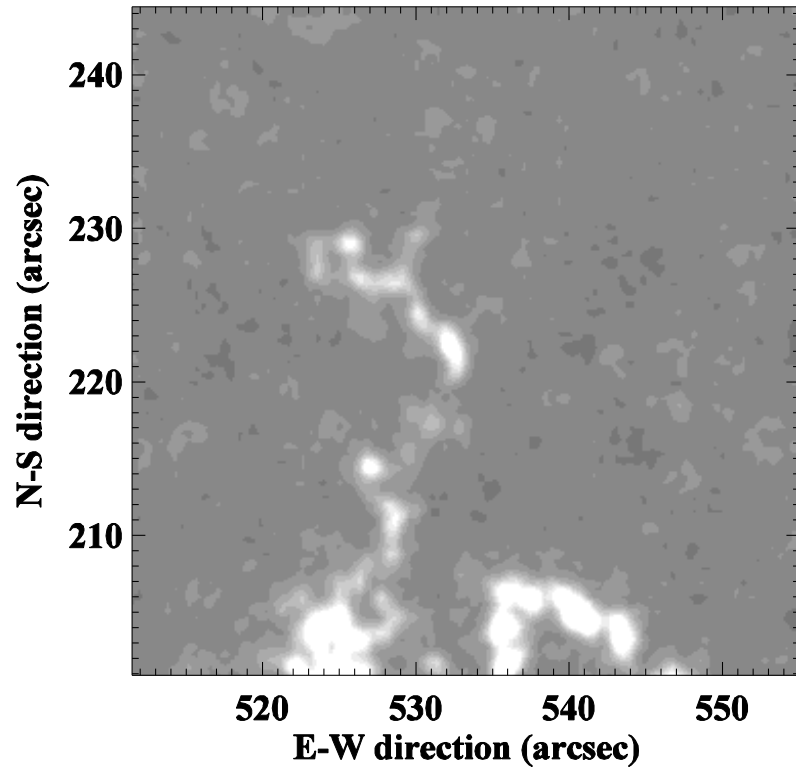


SDO/HMI

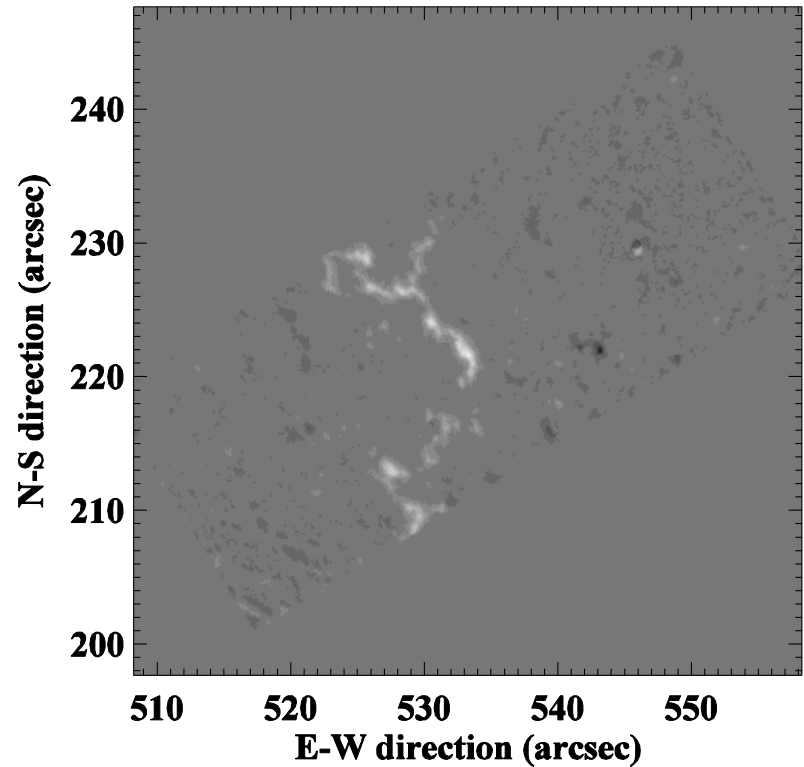


IRIM

NETWORK UNDER GOOD SEEING

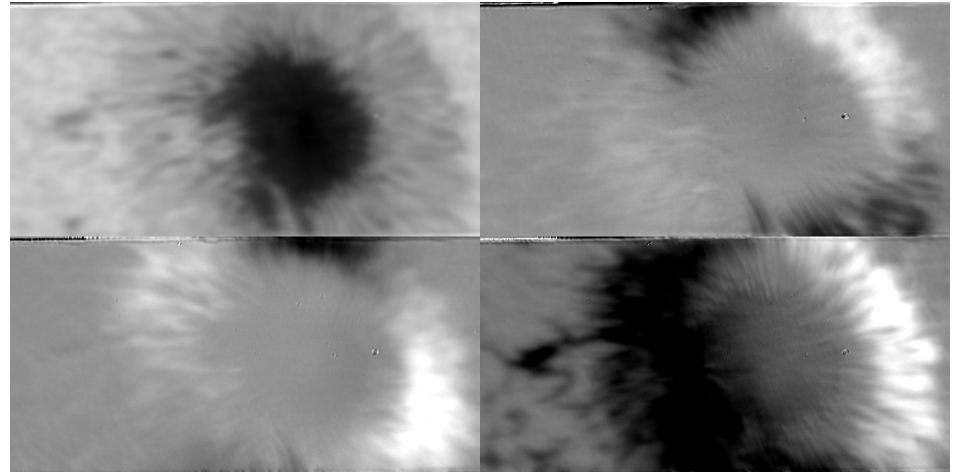
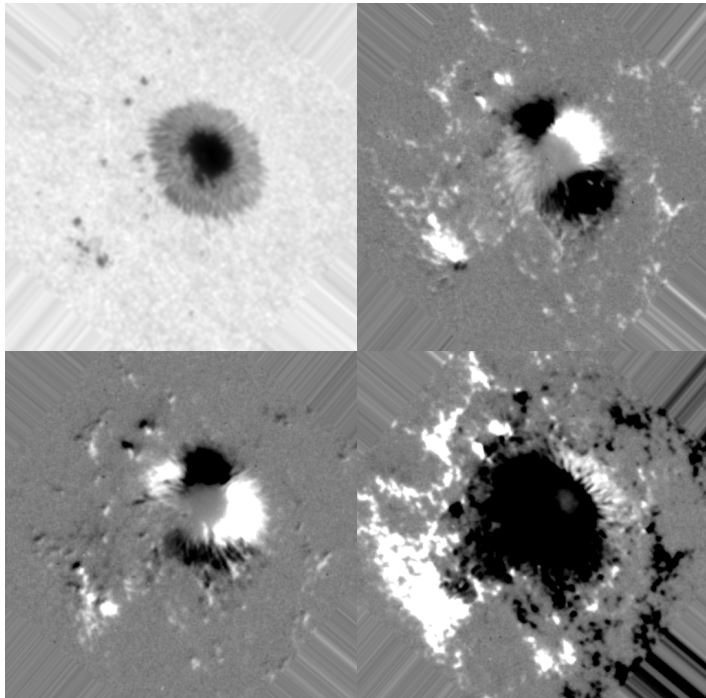


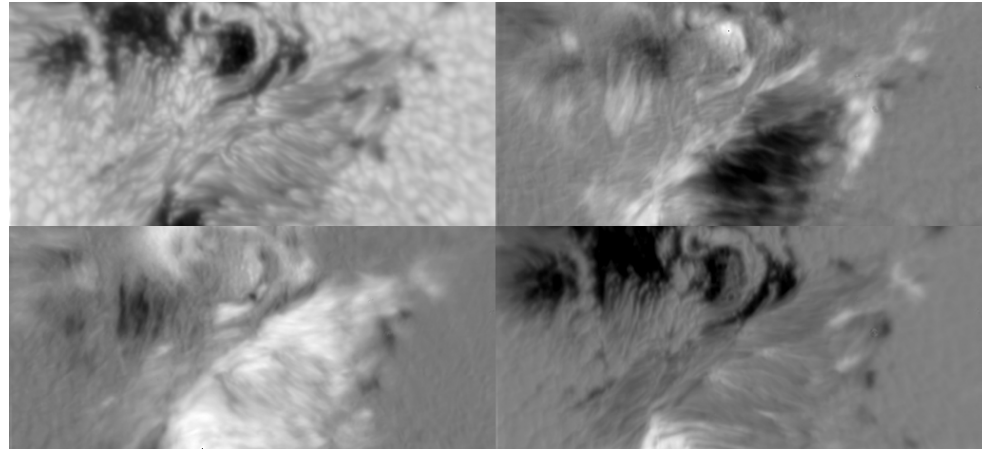
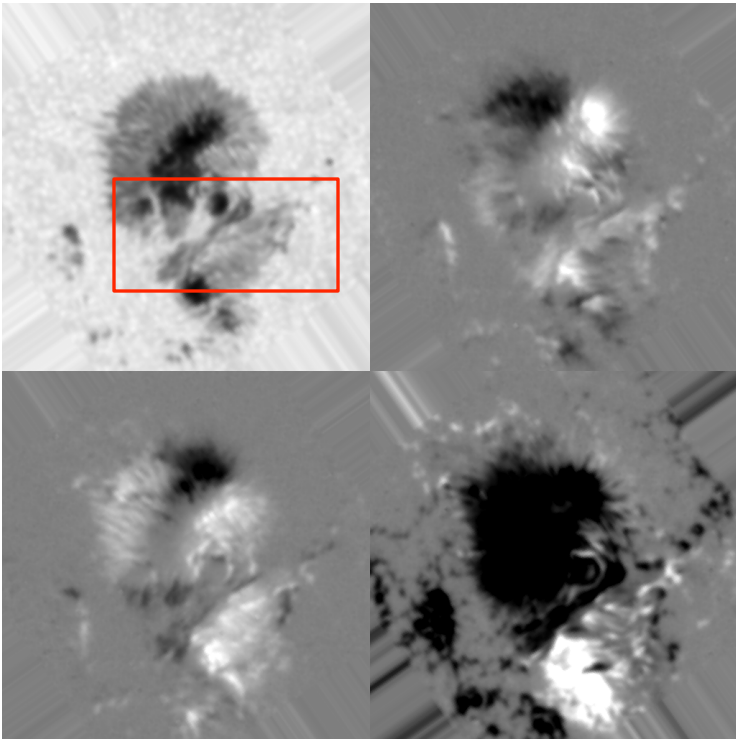
SDO/HMI



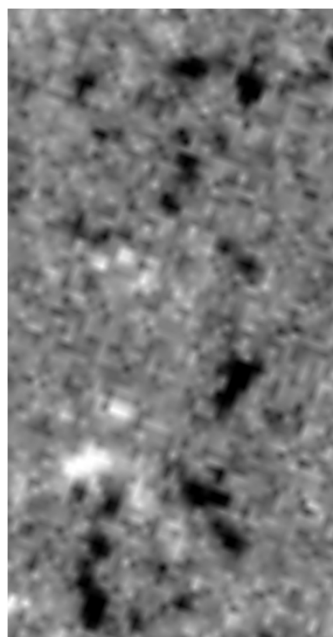
IRIM

COMPARISON WITH HMI

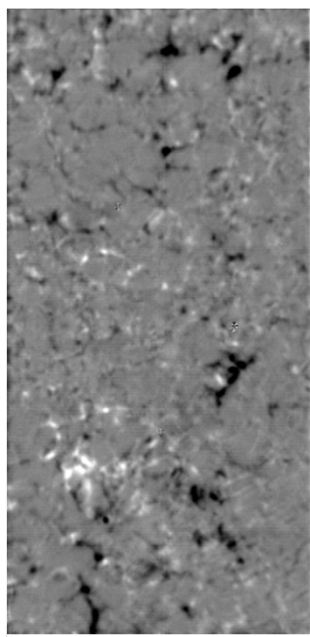




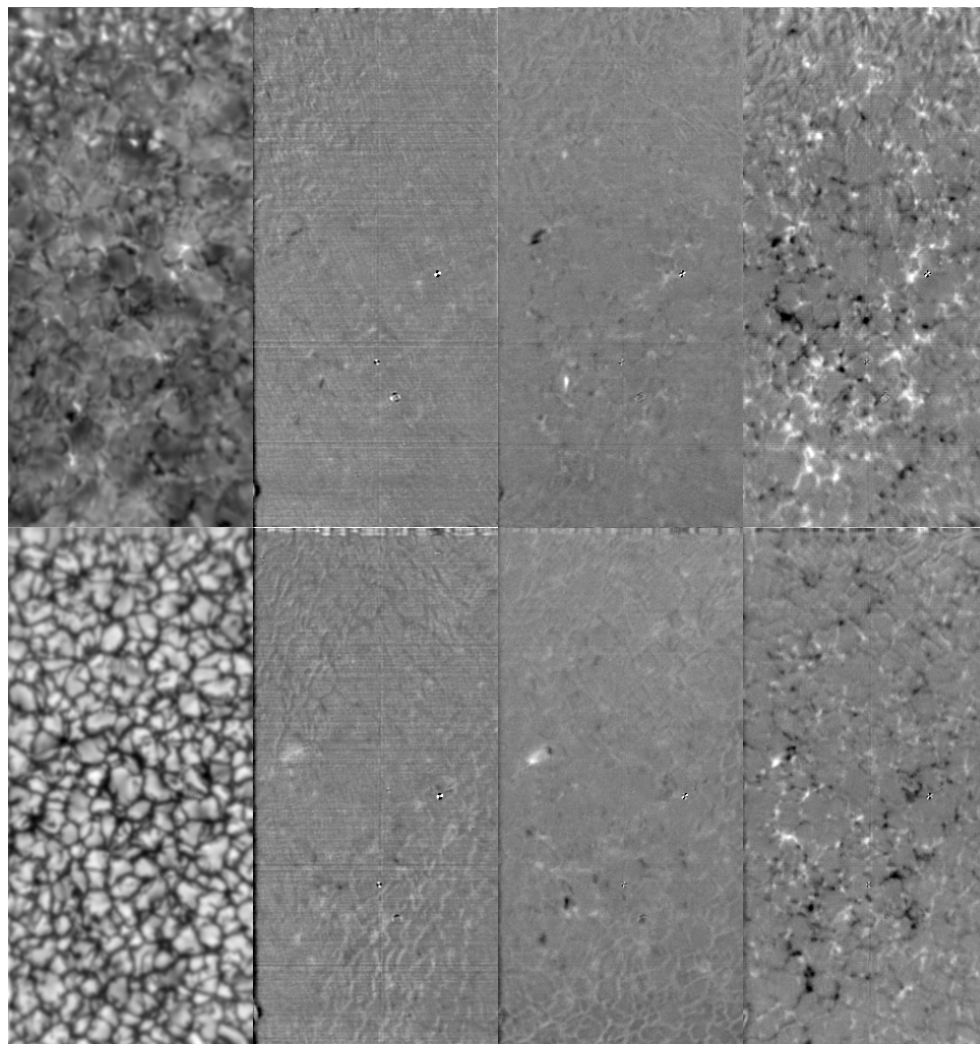
HIGH RESOLUTION POLARIMETRY



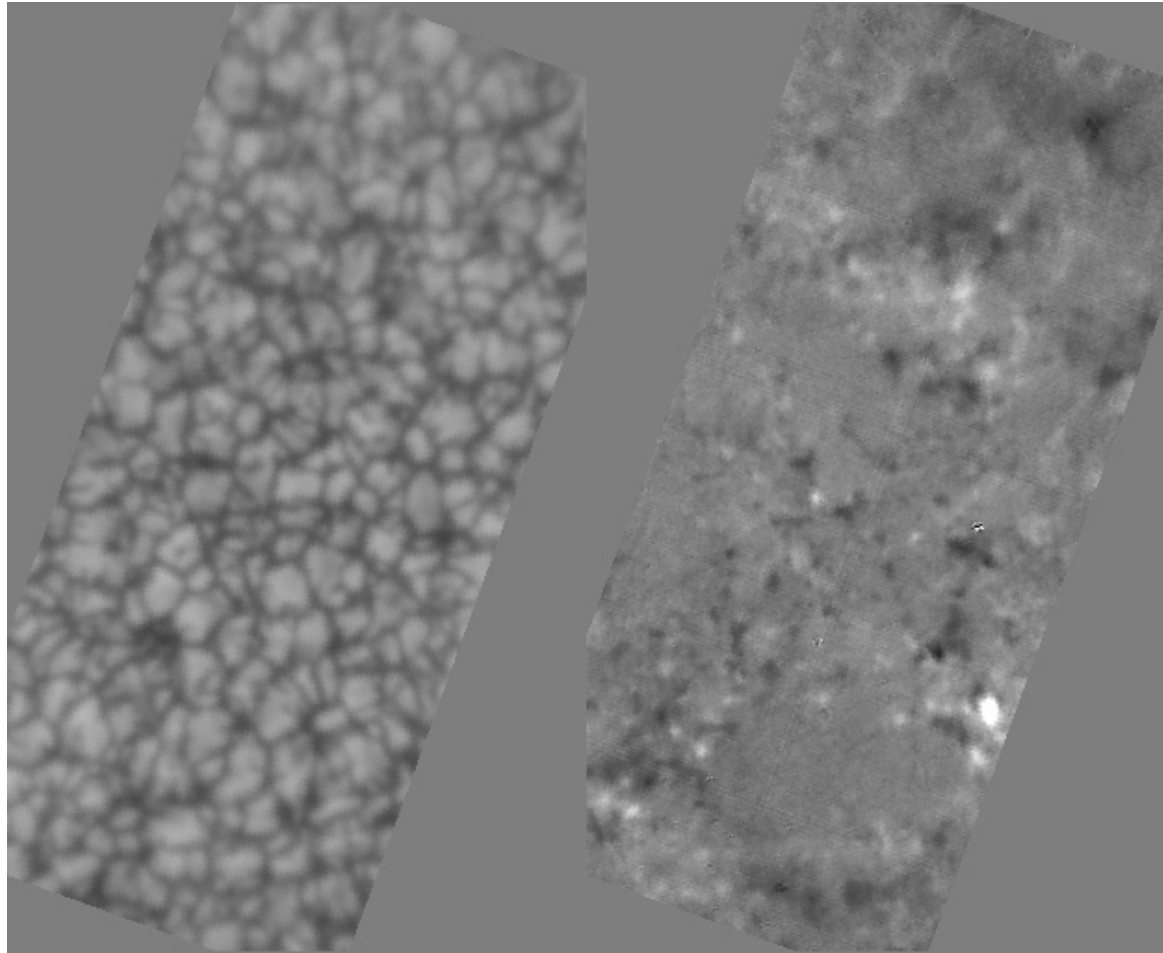
SDO/HMI



IRIM



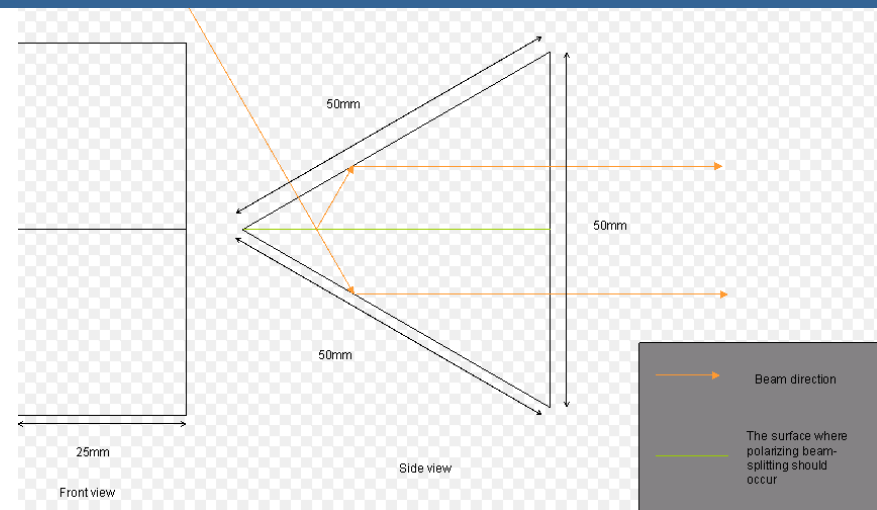
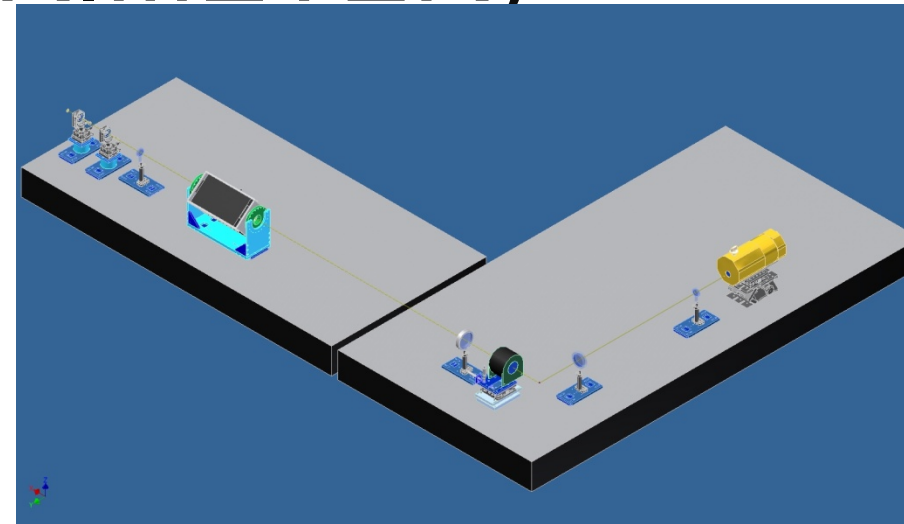
06/04/2012



NIRIS (NEAR-INFRARED IMAGING SPECTROPOLARIMETER)

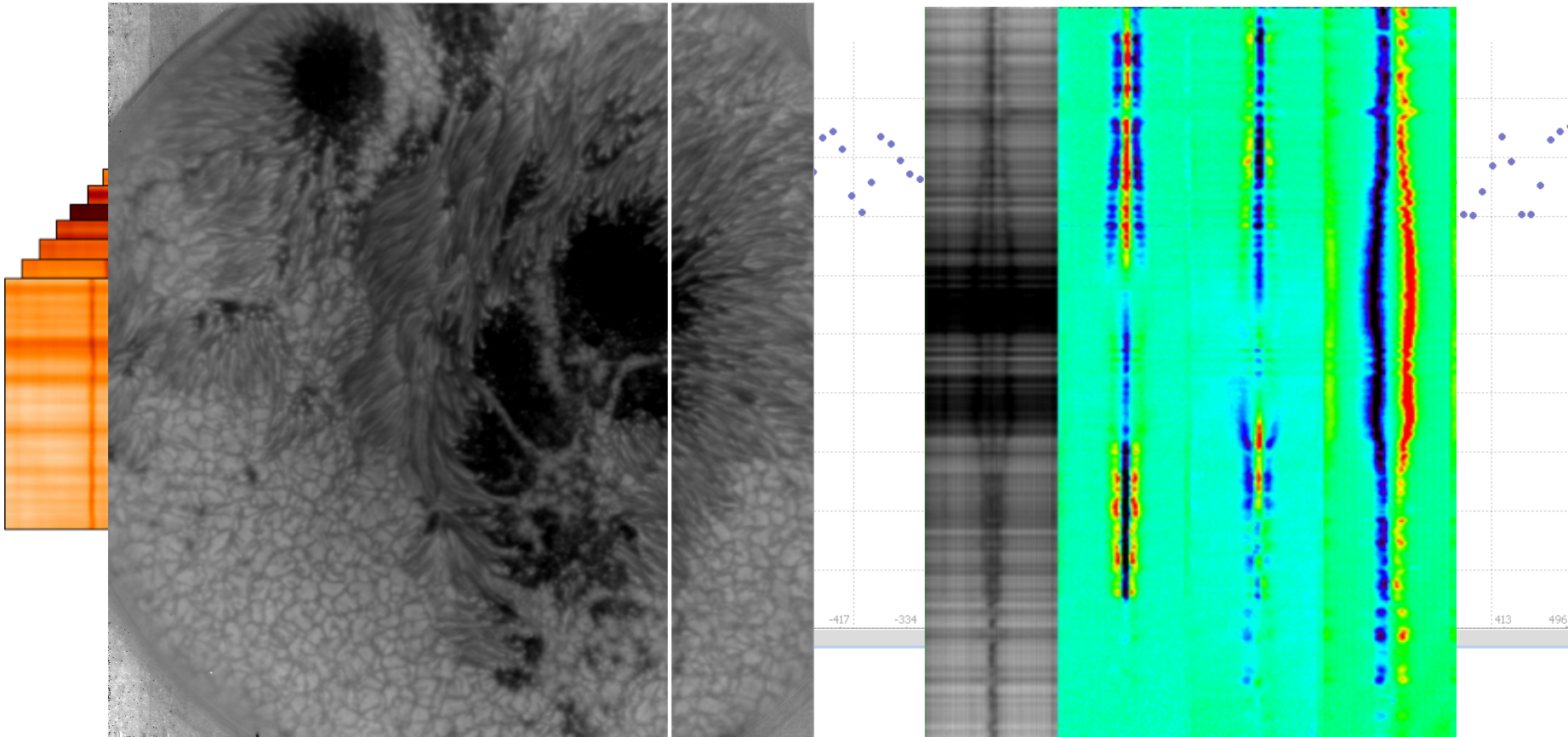
- Dual-beam imaging for minimal seeing crosstalk
- Field of view: 85" round
- Modulator: 2 rev/s
- Cadence: 40 s for 60 wv
- Accuracy: 10 G for B_l and 100 G for B_t

Observe 6 hrs per day throughout the year with many good seeing days!



SPECTROGRAPH VS. FILTER IMAGING

FISS

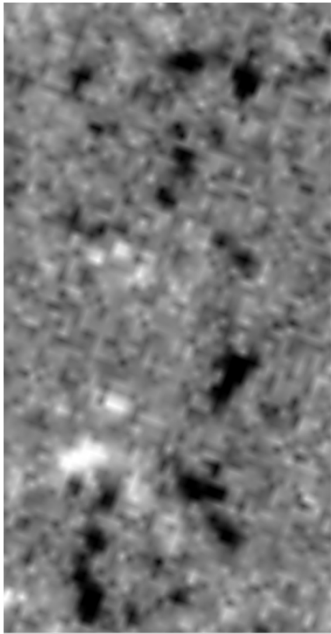


HIGH SPATIAL RESOLUTION W/ WIDER FIELD

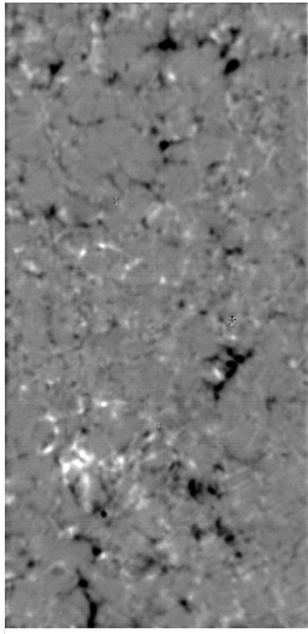
Diffraction limit: 0.25 arcsec

NIRIS

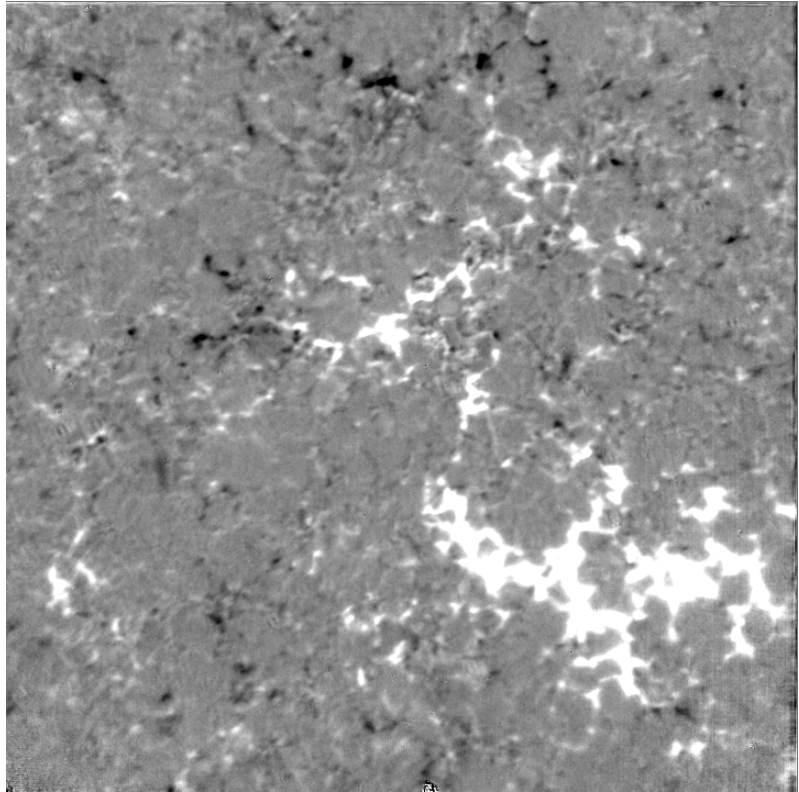
Typical resolution: 0.35 arcsec



SDO/HMI



IRIM



HIGH SPECTRAL RESOLUTION

Spectral bandwidth: 0.01 nm

Spectral sampling: typically 30-60 wavelengths, but flexible

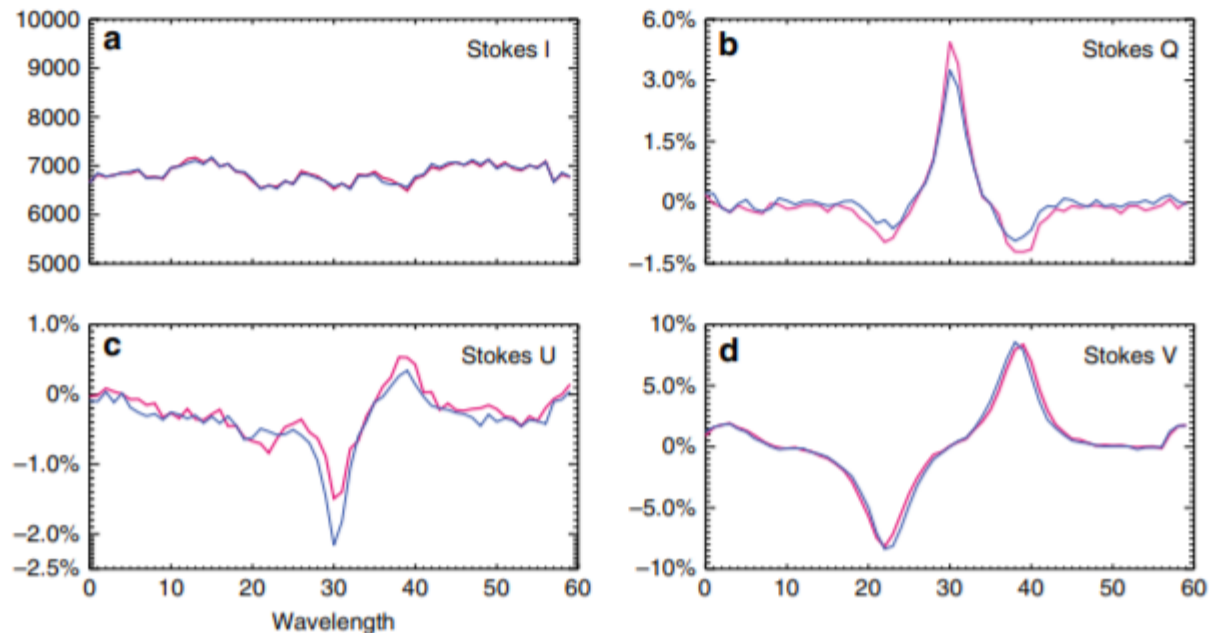
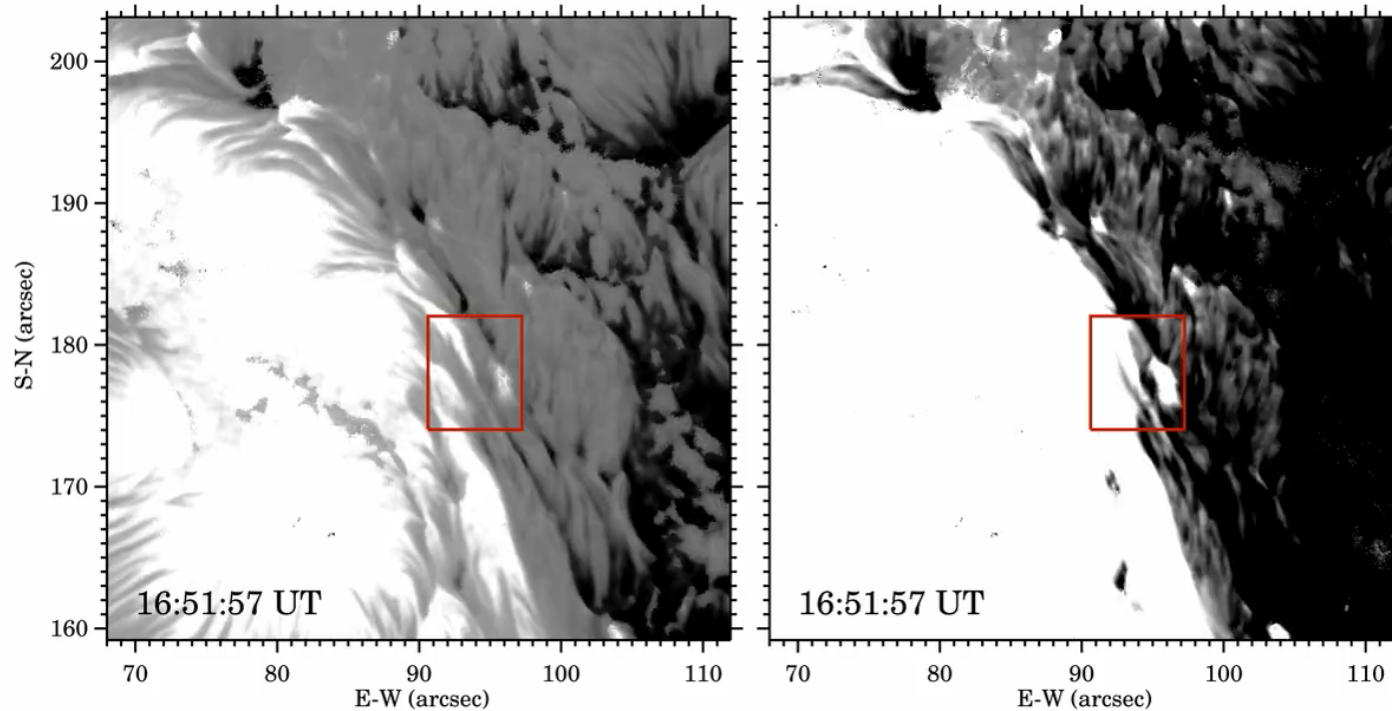


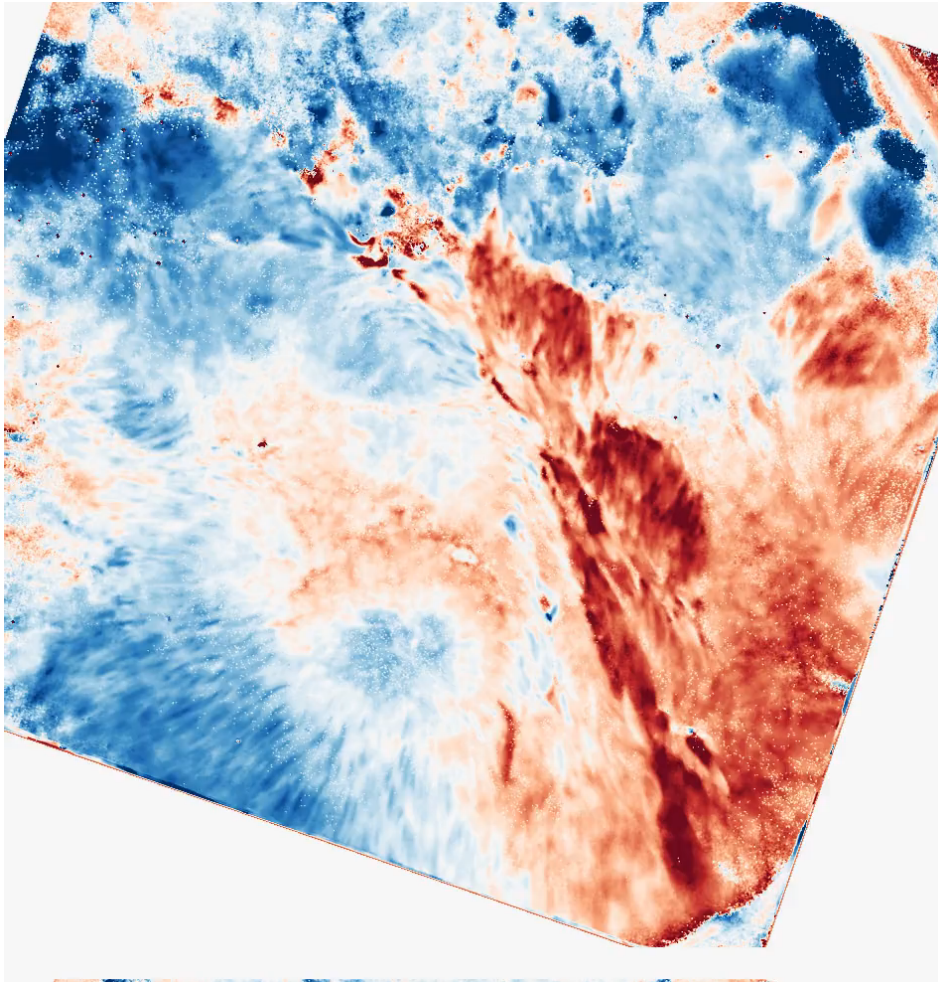
Fig. 5 Stokes profiles before and during the flare. Stokes components (I, Q, U, and V) taken near R3 before (blue) and during (pink) the flare. **a** Stokes I. **b** Stokes Q. **c** Stokes U. **d** Stokes V. It is clear that the Stokes I and V components remain almost unchanged but Q and U components are significantly affected during the flare

HIGH TEMPORAL RESOLUTION

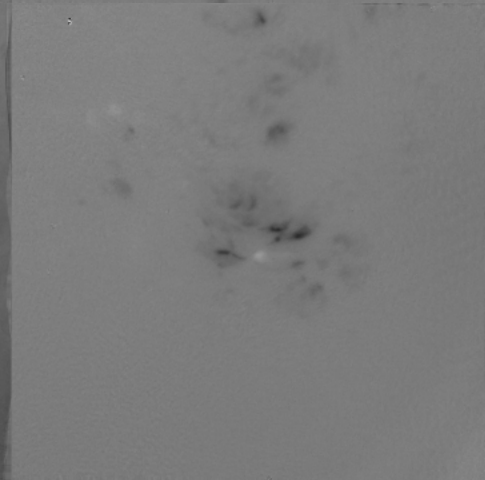
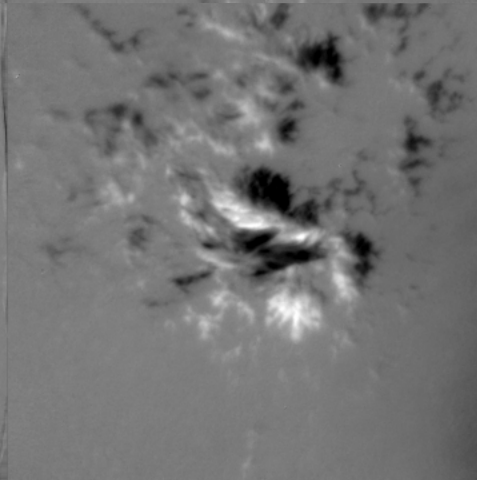
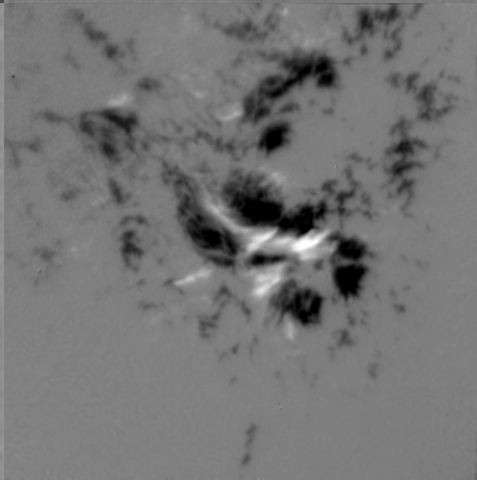
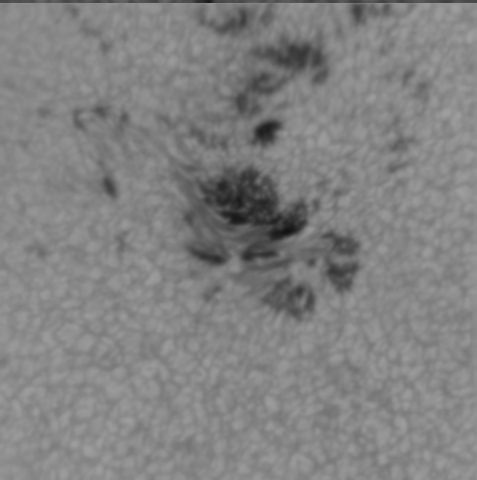
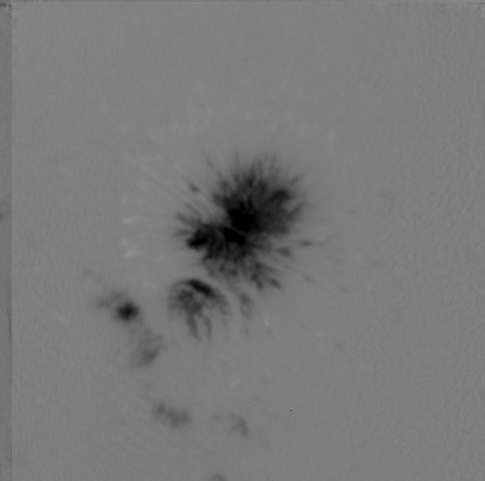
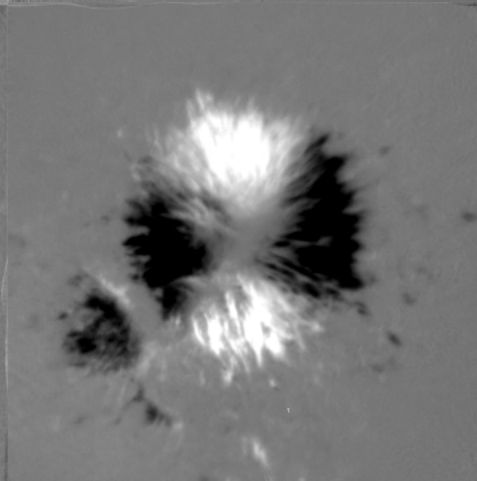
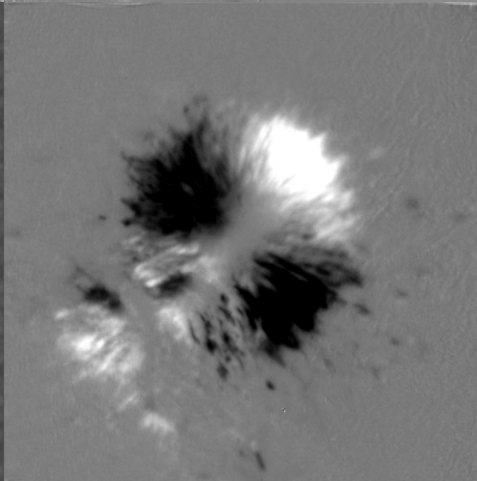
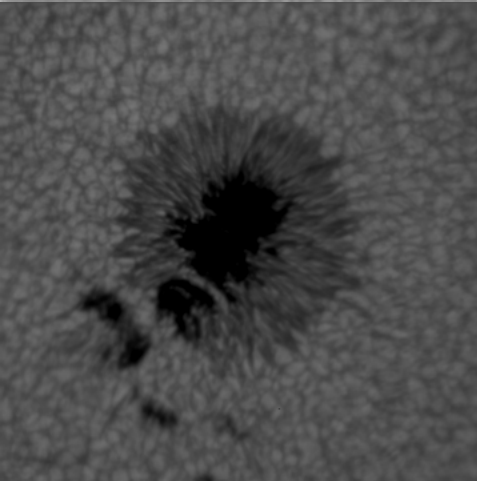
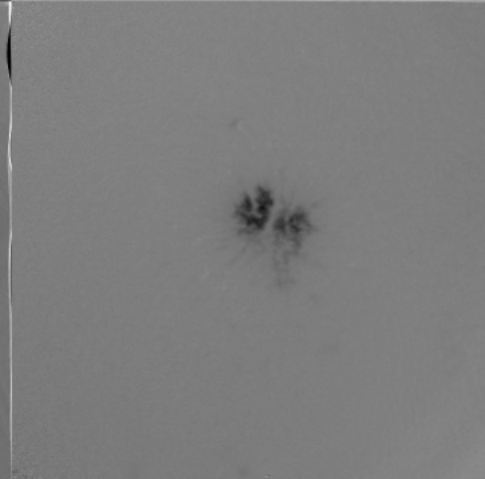
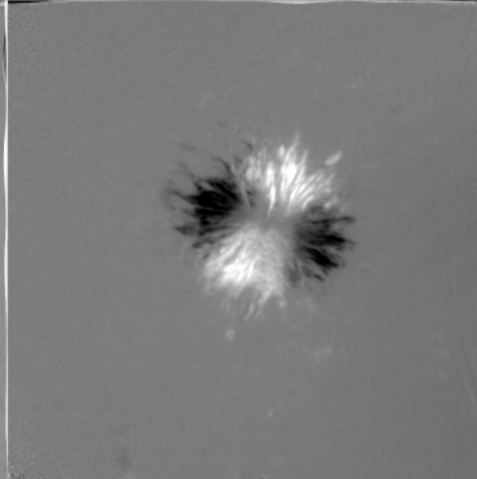
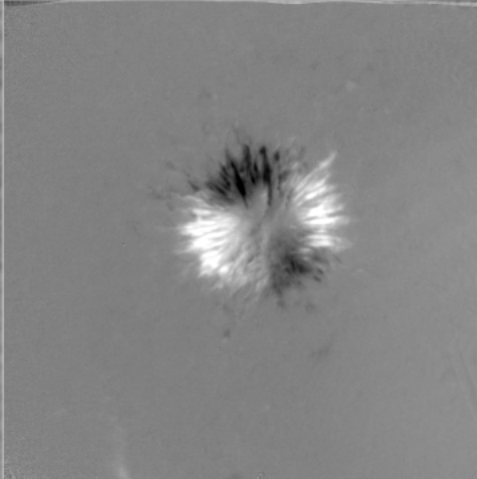
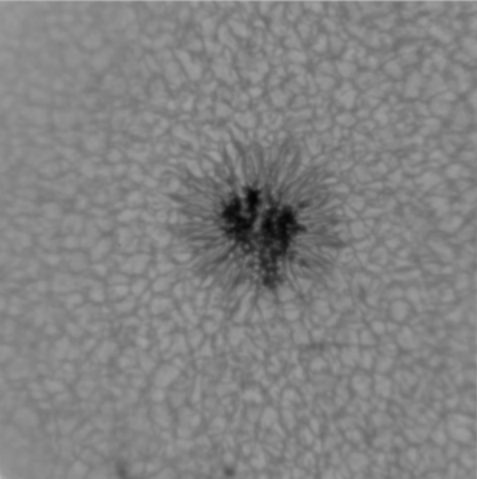
Temporal resolution: 25-45 secs, depending on the choice of wavelength sampling

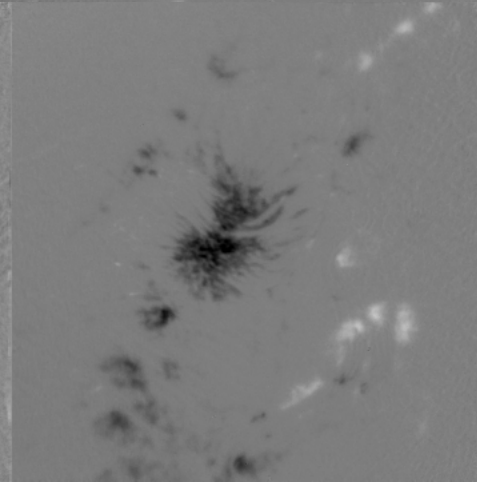
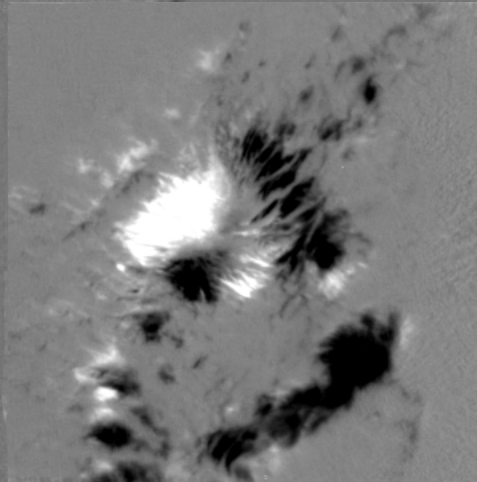
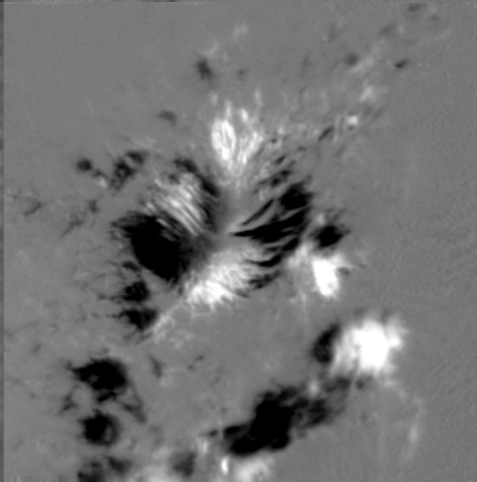
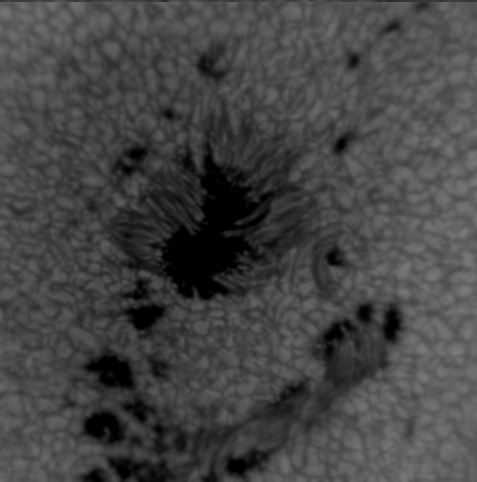
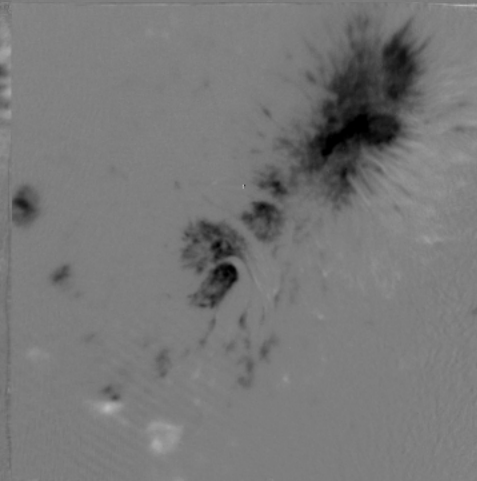
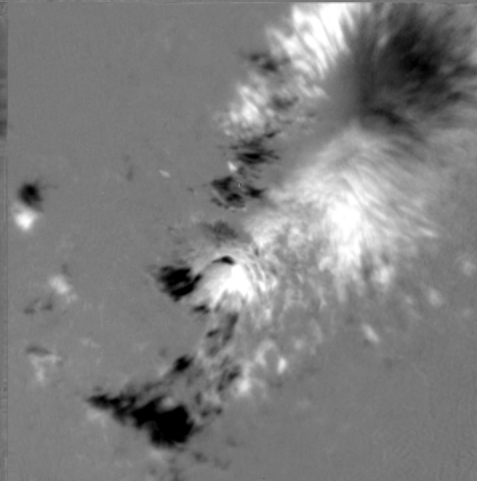
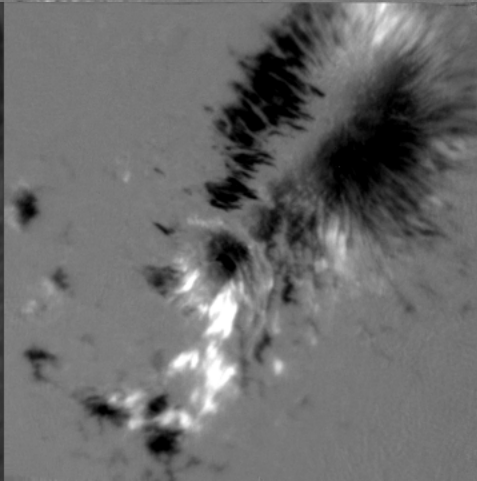
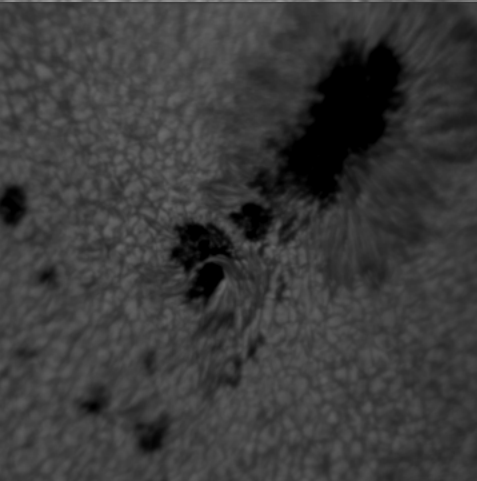
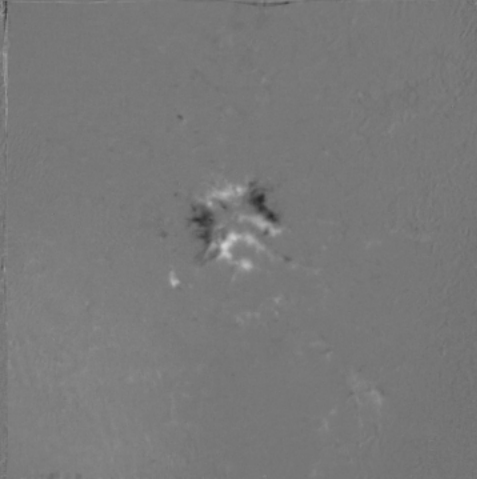
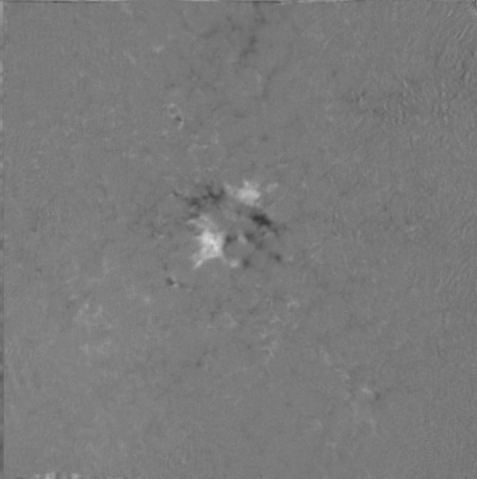
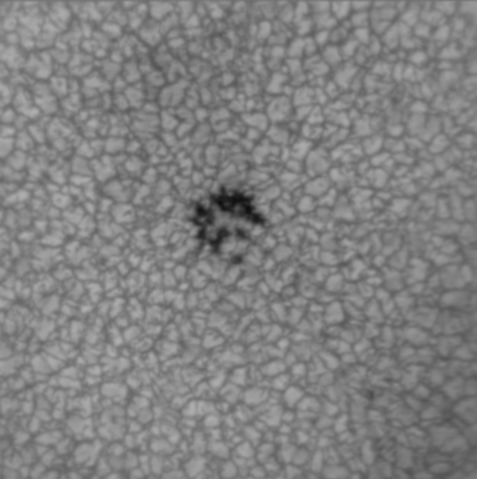


DOLLERGRAM

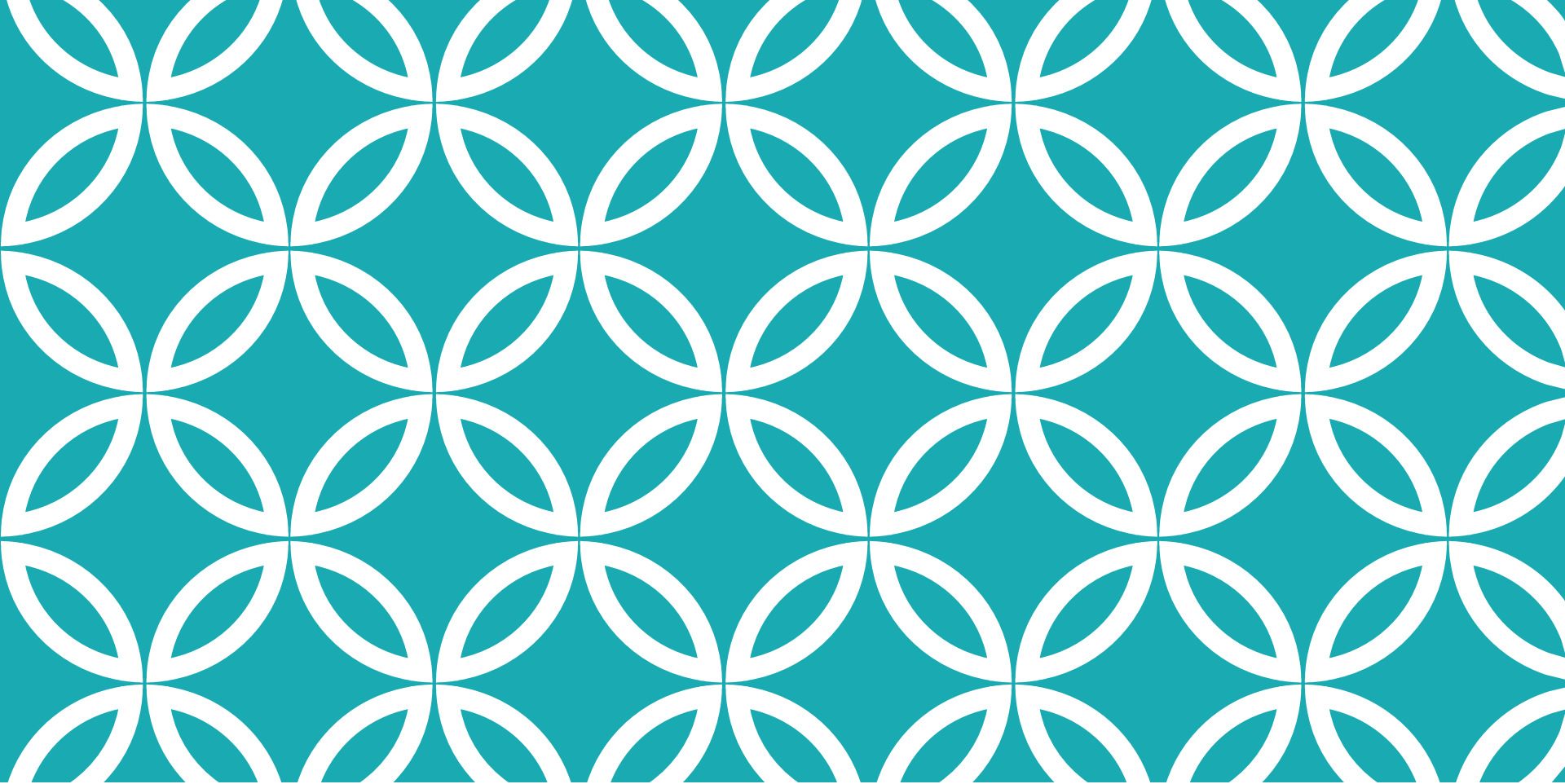


5 min oscillation?







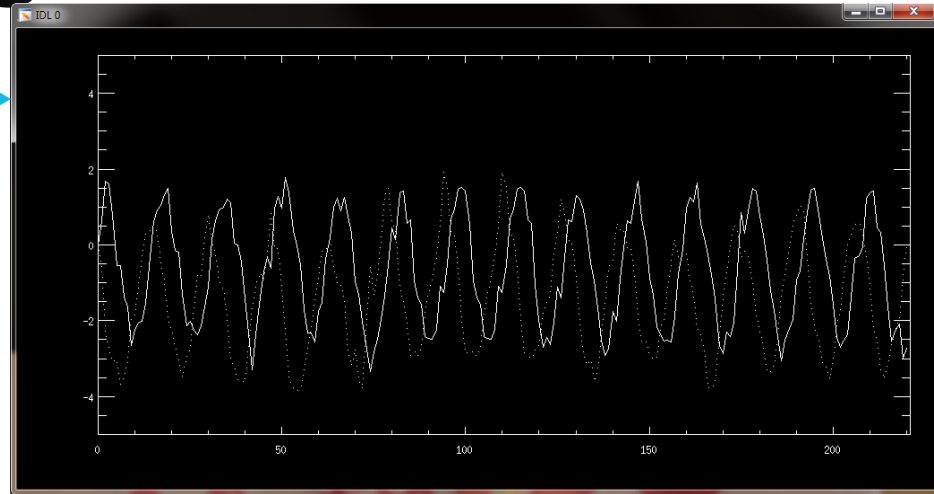


DATA PROCESSING & POLARIZATION CALIBRATION



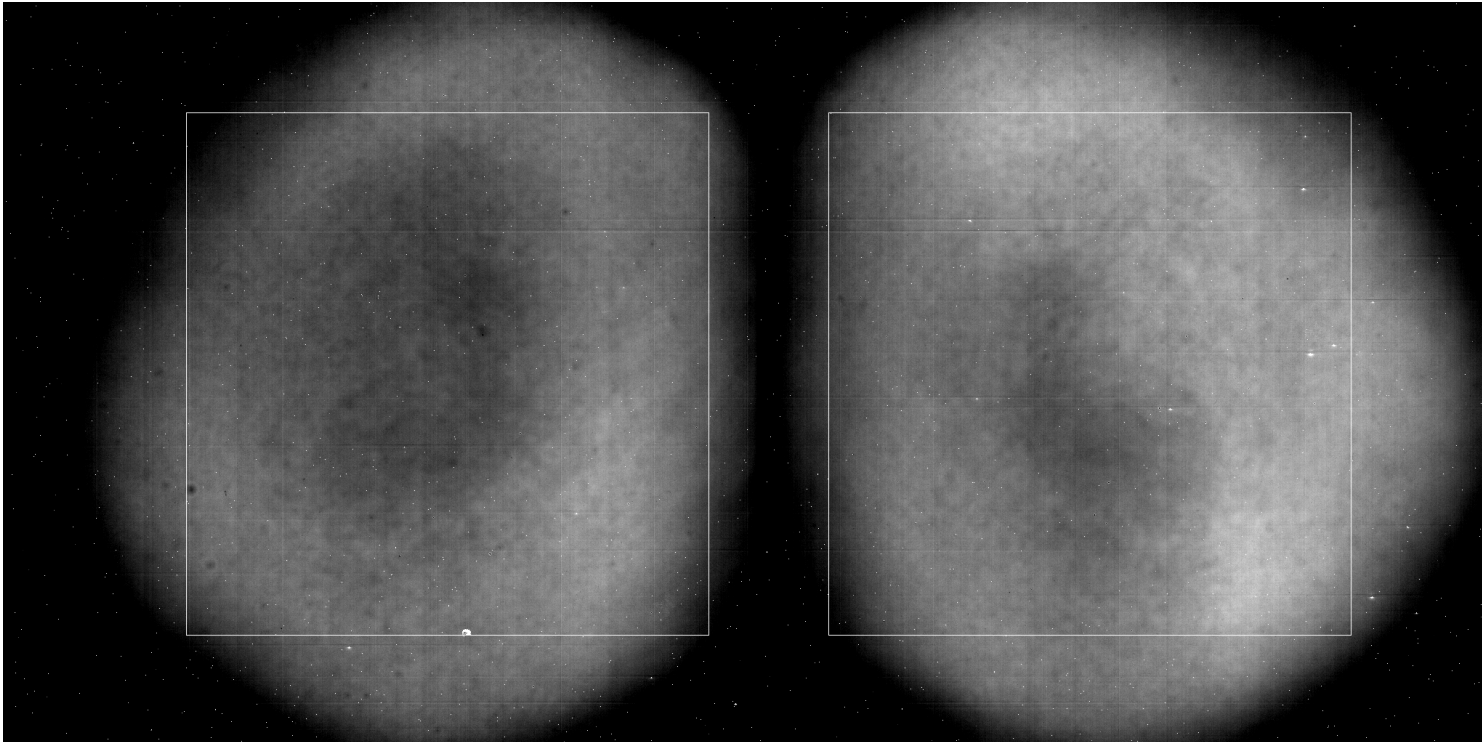
DATA PROCESSING PROCEDURES

- Dark/flat
- Align frames w/ features →
- Align dual beams
- Subtract dual beams w/ de-stretch (registration)
- Combine 16 frames to create initial Stokes profiles
- Correct for phase offset between modulator & detector
- Calibrate instrumental crosstalk



FLAT PATTERN

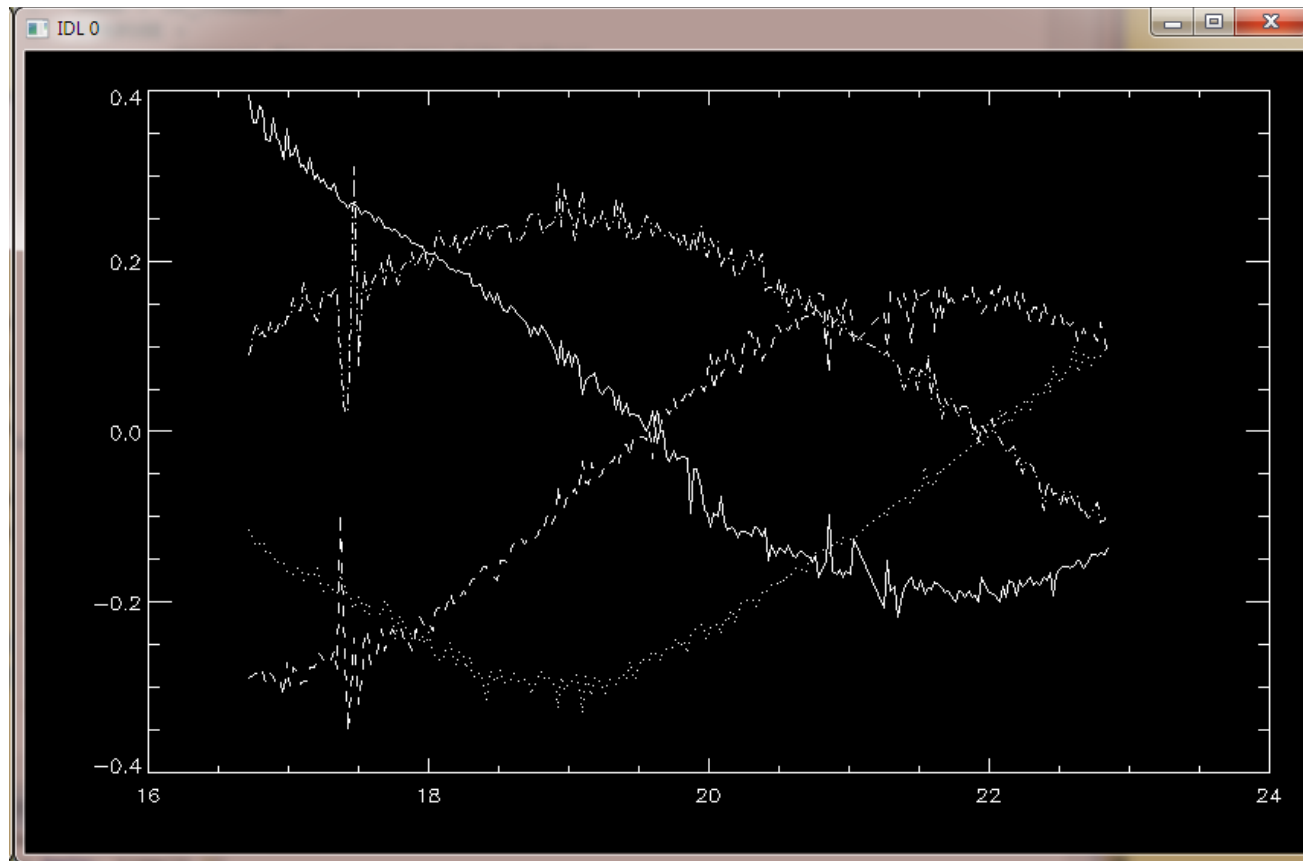
- ROI selection by default (720 x 720 pixels)



NIRIS DATA FILES

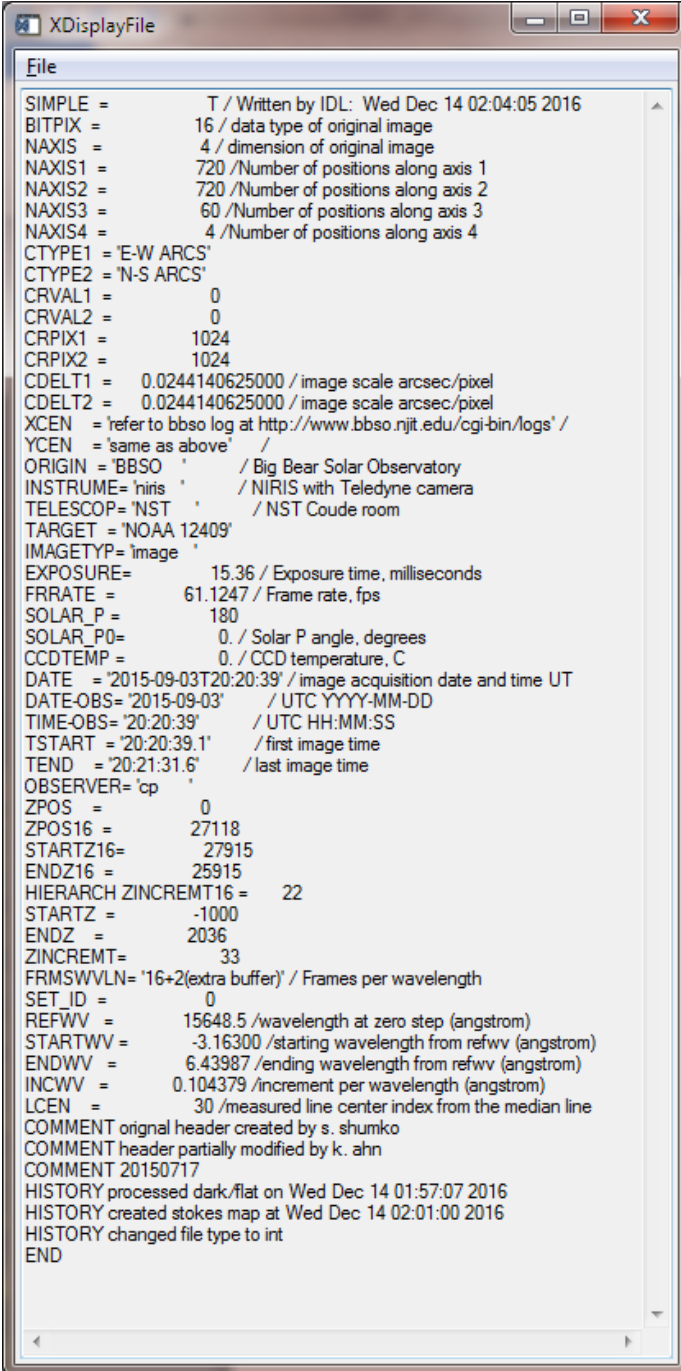
- `cals_150903_202039.fts`: Stokes I, Q, U, and V maps
- `fout150903_185524.sav`: an IDL binary file that includes some calibration parameters
- `snap_150903_173945`: snapshot images of the Stokes maps near the line center
- `nirisinv_YYMMDD_HHMMSS`: ME inversion files

SIGNIFICANT RESIDUAL CROSSTALK



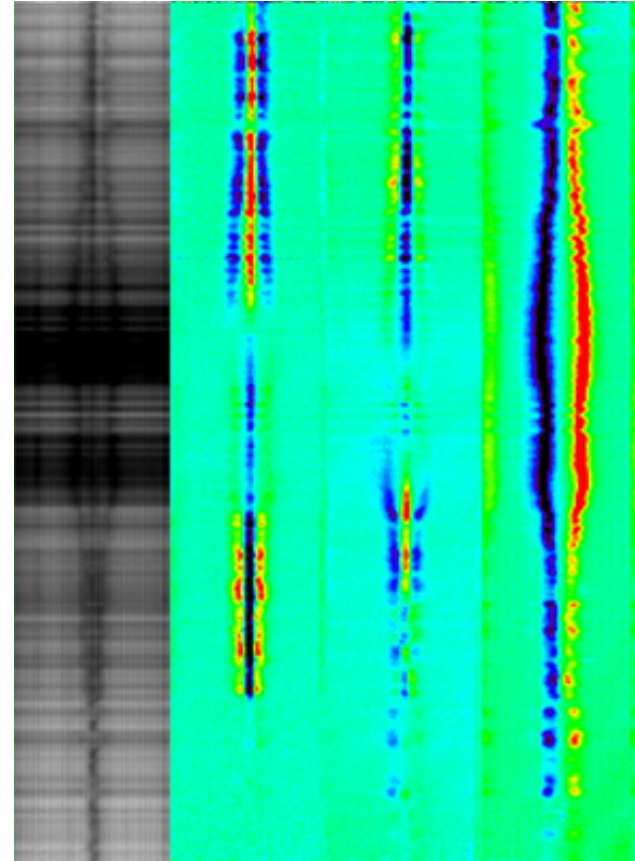
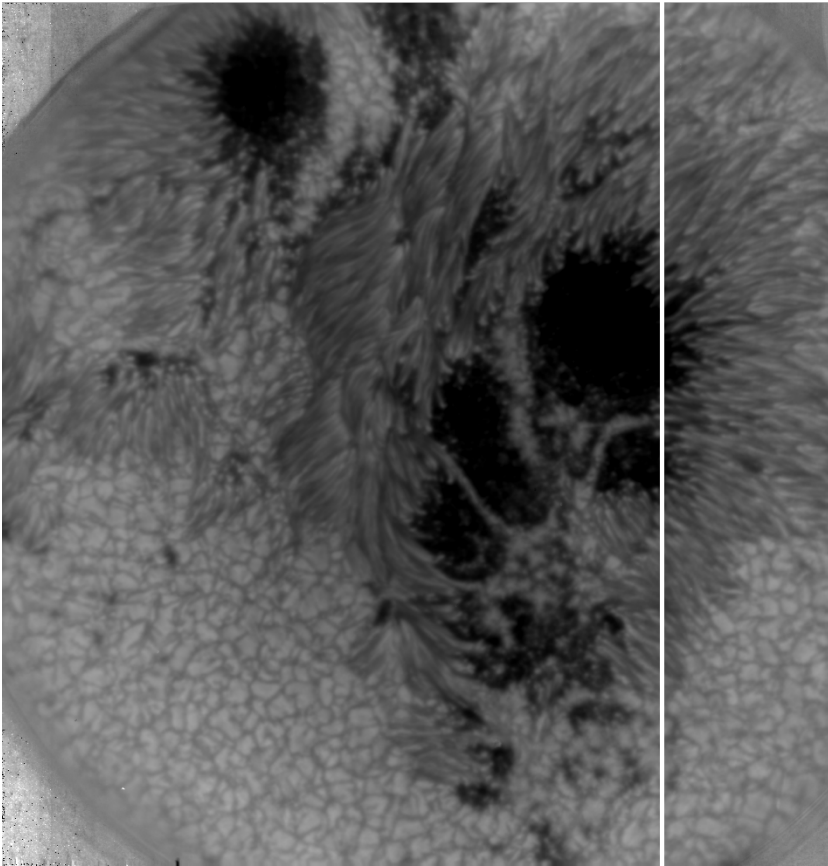
FITS HEADER OF CALS

- REFVW: the wavelength corresponding to the line center.
- STARTVW: a relative offset of wavelength from the REFVW
- ENDVW: a relative offset of wavelength from the REFVW
- INCVW: a change in wavelength for each scan step. Unit is in Angstrom.
- LCEN: This is a calculated round-up line center index in wavelength sampling sequence
- The COMMENT and HISTORY lines
- NAXIS1,2,3,4 : Each FITS file is a four-dimensional data (I, Q, U, V)
- Plot, `img[255,255,*,1]`



```
XDisplayFile
File
SIMPLE = T / Written by IDL: Wed Dec 14 02:04:05 2016
BITPIX = 16 / data type of original image
NAXIS = 4 / dimension of original image
NAXIS1 = 720 /Number of positions along axis 1
NAXIS2 = 720 /Number of positions along axis 2
NAXIS3 = 60 /Number of positions along axis 3
NAXIS4 = 4 /Number of positions along axis 4
CTYPE1 = 'E-W ARCS'
CTYPE2 = 'N-S ARCS'
CRVAL1 = 0
CRVAL2 = 0
CRPIX1 = 1024
CRPIX2 = 1024
CDELT1 = 0.0244140625000 / image scale arcsec/pixel
CDELT2 = 0.0244140625000 / image scale arcsec/pixel
XCEN = 'refer to bbsso log at http://www.bbsso.njit.edu/cgi-bin/logs/'
YCEN = 'same as above' /
ORIGIN = 'BBSO' / Big Bear Solar Observatory
INSTRUME = 'niris' / NIRIS with Teledyne camera
TELESCOP = 'NST' / NST Coude room
TARGET = 'NOAA 12409'
IMAGETYP = 'image'
EXPOSURE = 15.36 / Exposure time, milliseconds
FRRATE = 61.1247 / Frame rate, fps
SOLAR_P = 180
SOLAR_P0 = 0. / Solar P angle, degrees
CCDTEMP = 0. / CCD temperature, C
DATE = '2015-09-03T20:20:39' / image acquisition date and time UT
DATE-OBS = '2015-09-03' / UTC YYYY-MM-DD
TIME-OBS = '20:20:39' / UTC HH:MM:SS
TSTART = '20:20:39.1' / first image time
TEND = '20:21:31.6' / last image time
OBSERVER = 'cp'
ZPOS = 0
ZPOS16 = 27118
STARTZ16 = 27915
ENDZ16 = 25915
HIERARCH ZINCREMT16 = 22
STARTZ = -1000
ENDZ = 2036
ZINCREMT = 33
FRMSWVLN = '16+2(extra buffer)' / Frames per wavelength
SET_ID = 0
REFVW = 15648.5 /wavelength at zero step (angstrom)
STARTVW = -3.16300 /starting wavelength from refvw (angstrom)
ENDVW = 6.43987 /ending wavelength from refvw (angstrom)
INCVW = 0.104379 /increment per wavelength (angstrom)
LCEN = 30 /measured line center index from the median line
COMMENT original header created by s. shumko
COMMENT header partially modified by k. ahn
COMMENT 20150717
HISTORY processed dark/flat on Wed Dec 14 01:57:07 2016
HISTORY created stokes map at Wed Dec 14 02:01:00 2016
HISTORY changed file type to int
END
```

SPECTRAL PROFILES



CALIBRATION

Sources of magnetic signal errors (crosstalk)

- Image motion due to seeing
 - Faster modulation reduces seeing-induced crosstalk
 - Longer wavelength has less contamination.
- Crosstalk due to optical components
 - Mirror surface can function as both retarder & linear polarizer.
 - Retardation proportional to ϑ^2

SEEING-INDUCED CROSSTALK

Single beam : To measure Stokes V with I+V at t1 and I-V at t2

Intensity fluctuation due to image motion – bigger than pol. signals

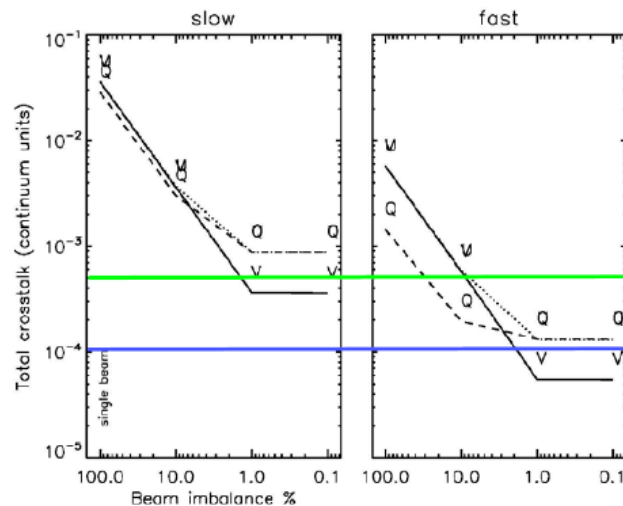


Figure 3.5: Crosstalk level compared to the line continuum according to the rotation speed of retarder and the amount of beam imbalance between two cameras (Judge et al., 2004; Elmore, 2006). The beam imbalance of 100% signifies single beam.

DUAL BEAM TO MINIMIZE SEEING

IRIM_control

Contrast: Min 4000, Max 7000, Set

Exposure time in ms: 180, TCS connect, Connected

Frame rate, fps: 10.00

Camera: FPI | Lyot | Polarizer

Scan range: Start -140, End -130, Total 240, Increment units 0, # of steps 25

pm -39.76, 28.4, 68.16, pm 2.84

Check, Connect FPI, Disconnect FPI

Status, Position, Move FPI, Z position 0, Move

Frames per Z step: 1, Average

Modes of operation: Spectroscopy (checked), Plot (checked), Polarimetry

of scans: 1

Addl. information: Observer: rjf, Image type: image, Target: , Comment: some comment

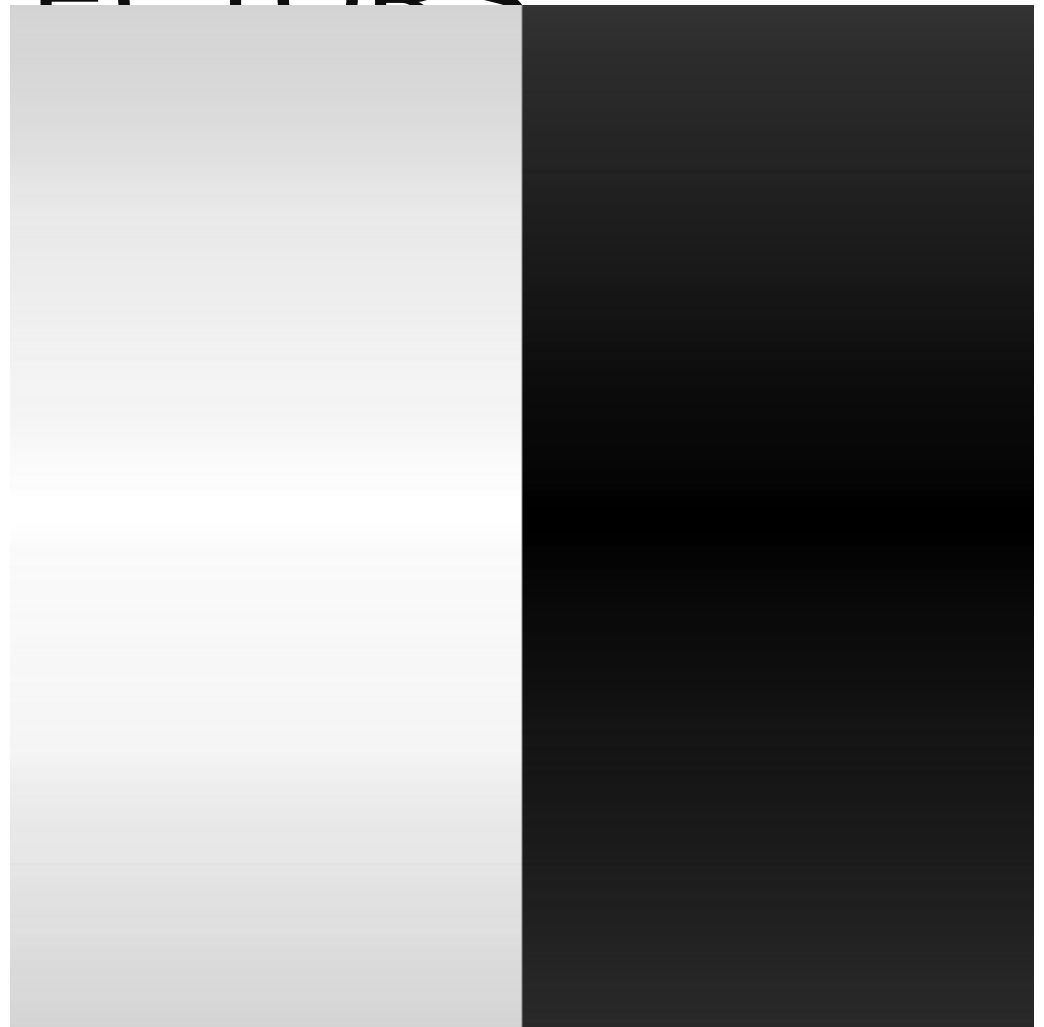
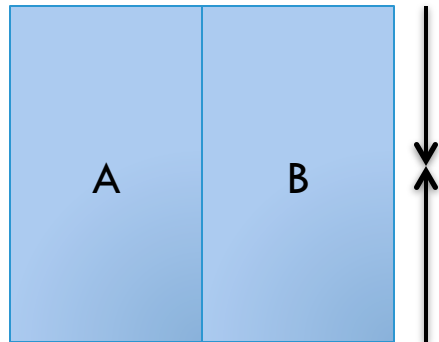
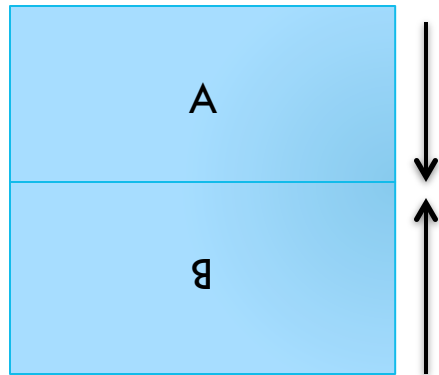
Start, Stop, Save files (checked), Dark frames: Take dark, # of frames 50

Intensity at cursor position: |x=1014 y=468 intensity=7236

Image statistics: |Min=1125, Max=14891, Overexp.=0, avg=6883

Status: |Live img frame rate 5.4 fps, 128 18 36 0

RIPPLE READOUT OF CMOS DETECTORS



CALIBRATION OF INSTRUMENTAL CROSSTALK: MUELLER MATRIX M

- A 4 x 4 matrix that describes the polarization properties of the optics
 - $(I' Q' U' V')^T = M (I Q U V)^T$
- If there are multiple optics in the beam train, M is the multiplication of Mueller matrix for each optical component.
 - $M = M_n M_{n-1} M_{n-2} \dots M_3 T$
 - $(I Q U V)^T = M^{-1} (I' Q' U' V')^T$
 - ~20 mirror elements function as a quarter-wave plate!

- Mueller matrix of a single mirror
 - r_s/r_p : reflectivity ratio between parallel & perpendicular light
 - δ : retardation

$$M = \begin{bmatrix} 1 & \frac{1 - \frac{r_s}{r_p}}{1 + \frac{r_s}{r_p}} & 0 & 0 \\ \frac{1 - \frac{r_s}{r_p}}{1 + \frac{r_s}{r_p}} & 1 & 0 & 0 \\ 0 & 0 & \frac{2\sqrt{\frac{r_s}{r_p}} \cos \delta}{1 + \frac{r_s}{r_p}} & \frac{2\sqrt{\frac{r_s}{r_p}} \sin \delta}{1 + \frac{r_s}{r_p}} \\ 0 & 0 & \frac{2\sqrt{\frac{r_s}{r_p}} \sin \delta}{1 + \frac{r_s}{r_p}} & \frac{2\sqrt{\frac{r_s}{r_p}} \cos \delta}{1 + \frac{r_s}{r_p}} \end{bmatrix}$$

CALIBRATION OF T (TELESCOPE)

$$T = M_2 M_1$$

Off-axis geometry creates non-zero polarization

Average incident angle of GST – 12 deg.

Simulation performed by S. Yuan

Our conclusion : T is not significant

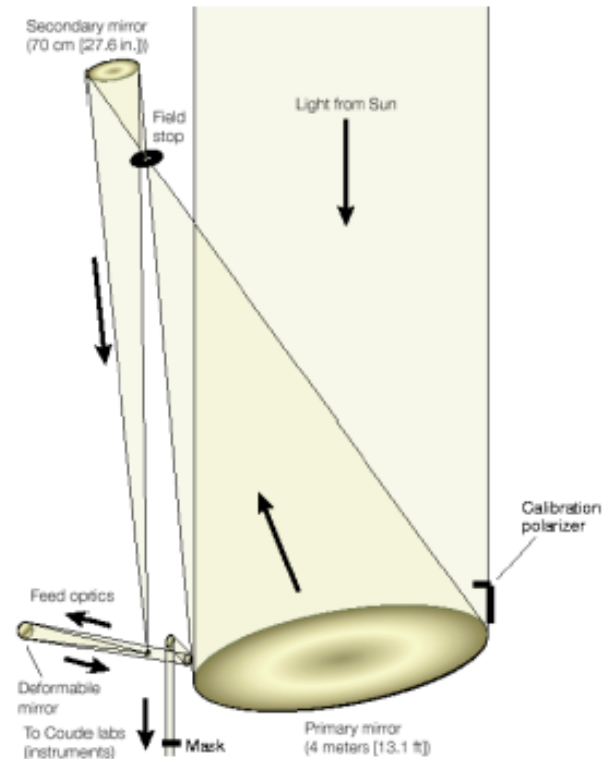
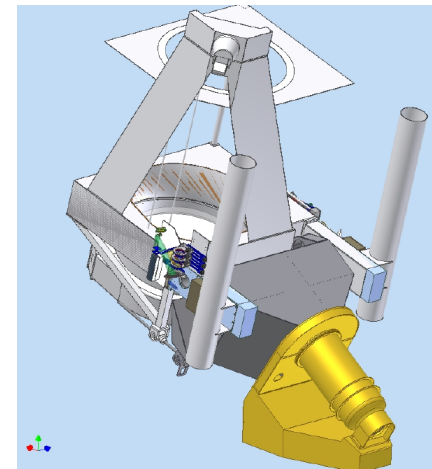


Figure 3.6: Calibration of a telescope by sub-aperture method (Socas-Navarro, 2005; Elmore, 2006). A calibration unit that is smaller than the aperture of the telescope sweeps over the aperture to measure crosstalk at a sub-field, while a mask behind the secondary mirror blocks the beam that does not pass through the calibration optics.

SIMULATING M FOR THE YEAR: GROUPING OPTICAL ELEMENTS

- Cannot perform calibration often.
- Proposed by D. Elmore
- Dec rotation between M3 & M4
- HA rotation between M4 & M5
- Add a coordinate-breaking matrix at every fast-axis change
- $M(\text{dec,ha}) = M_{\text{rest}} R(\phi_3, \text{ha}) M_4 R(\phi_2, \text{dec}) M_3 R(\phi_1) T$
- M over different HA and DEC are measured.



FINDING M_{REST} THAT IS INVARIANT OVER DEC & HA

- Assumption: T and relay optics are mature (no rapid build-up of oxidized coating).
 - $M(\text{dec,ha}) = M_{\text{rest}} R(\phi_3, \text{ha}) M_4 R(\phi_2, \text{dec}) M_3 R(\phi_1)$
 - When passing through the linear polarizer, the information of T does not transmit in most cases.
- $M_{\text{rest}} = M [R(\phi_3, \text{ha}) M_4 R(\phi_2, \text{dec}) M_3 R(\phi_1)]^{-1}$
= constant
 - \rightarrow Invariant over whole time of the year, ideally.
- Find the combination of M_3 & M_4 properties ($r_s/r_p, \delta$) that makes M_{rest} nearly constant possible
 - Minimum standard deviation of data points

M_{REST}

- Get the combination of M_3 & M_4 properties that minimizes deviation of M_{rest} through least square fitting
 - $r_s/r_p = -0.004$
 - $\delta_{M3} = -25^\circ$
 - $\delta_{M4} = -27^\circ$
- Determine M_{rest} , then multiply with $R(\phi_3, ha) M_4 R(\phi_2, dec) M_3 R(\phi_1)$ to get M for any day of year

BETTER WAY – MULTI-PARAMETER FITTING FROM MULTIPLE MEASUREMENTS

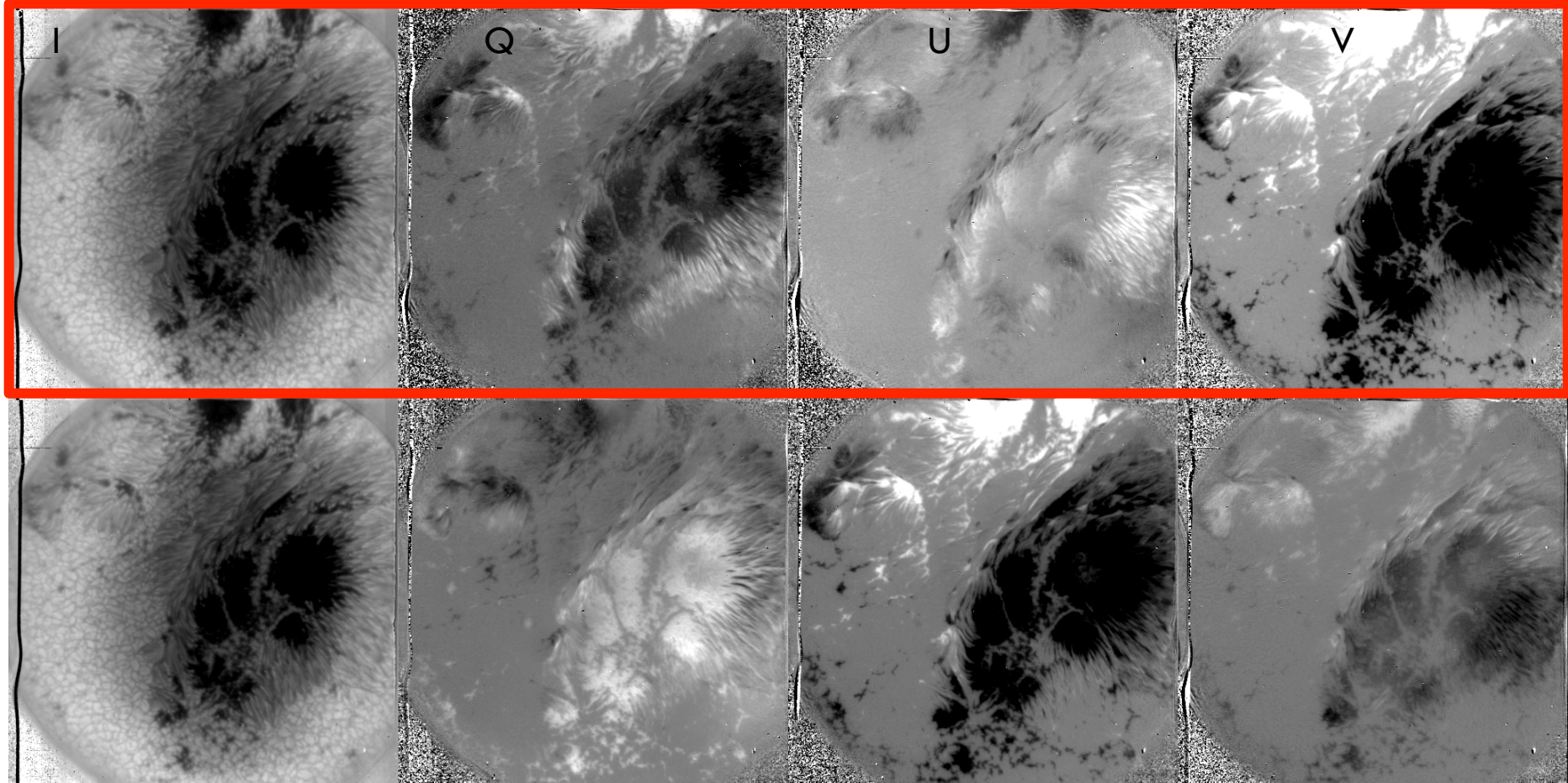
$$\mathbf{s}_1 = \mathbf{XUCs}_t + \mathbf{b} \quad (1)$$

where

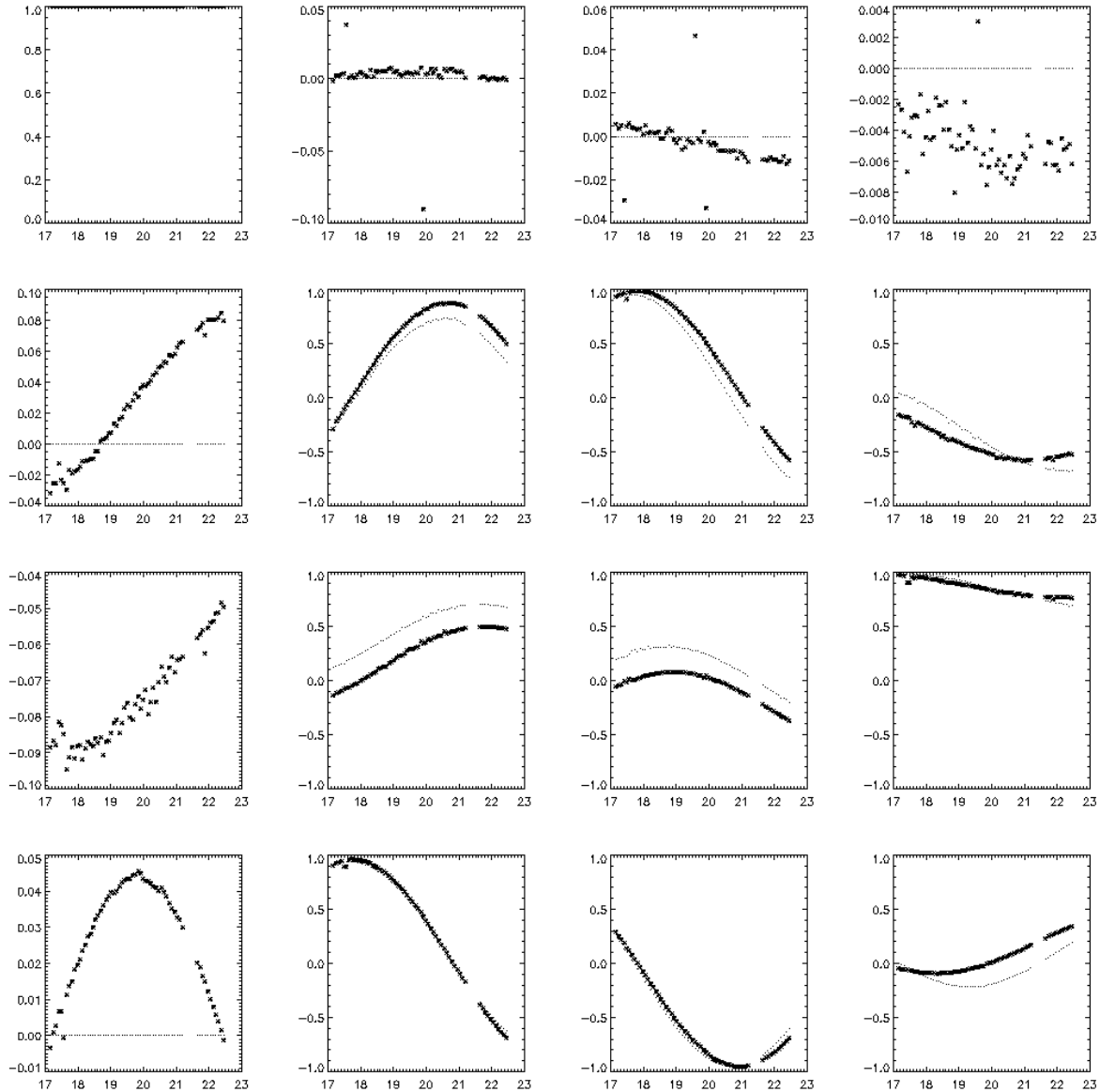
- $\mathbf{s}_1(x,y,\lambda)$ \equiv Measured instrument vector
- $\mathbf{X}(x,y,\lambda)$ \equiv Polarimeter response matrix
- $\mathbf{U}(x,y,\lambda)$ \equiv Unknown sample Mueller matrix
- $\mathbf{C}(x,y,\lambda)$ \equiv Calibration optics configuration Mueller matrix
- $\mathbf{s}_t(x,y,\lambda)$ \equiv Lamp Stokes vector (historically the telescope vector)
- $\mathbf{b}(x,y)$ \equiv Instrument bias vector
- x \equiv Horizontal spatial dimension
- y \equiv Vertical spatial dimension
- λ \equiv Wavelength

Without the sample in the beam but with a series of polarization configurations, sufficient measurements of the instrument vector are collected to allow the \mathbf{X} matrix to be calculated as described in the next sections. The same measurements are repeated with the unknown sample in the beam and a new polarimeter response matrix, $\mathbf{X}' = \mathbf{XU}$, is calculated. The unknown sample Mueller matrix is then $\mathbf{U} = \mathbf{X}^{-1}\mathbf{X}'$.

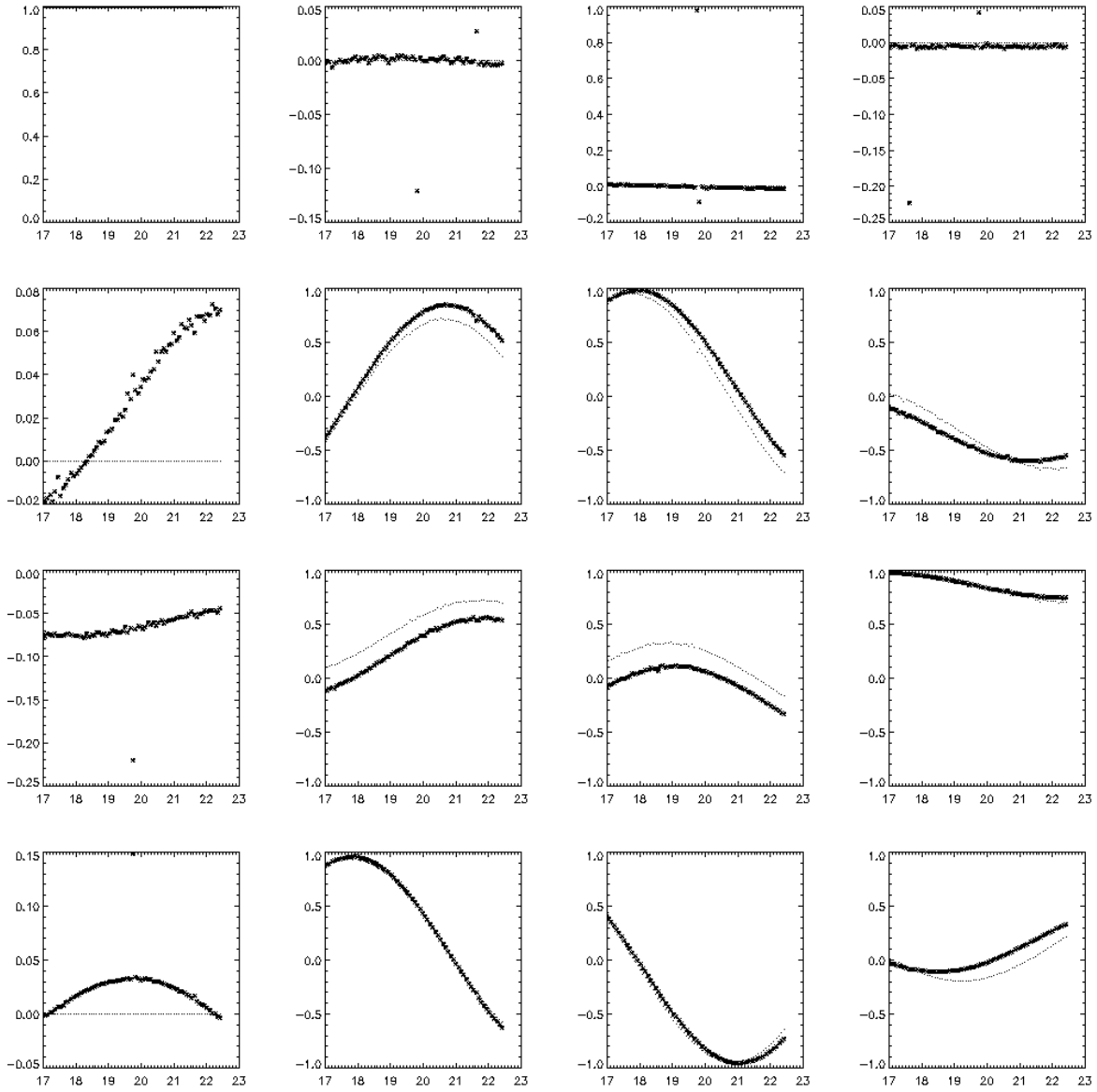
CALIBRATION OF INSTRUMENTAL



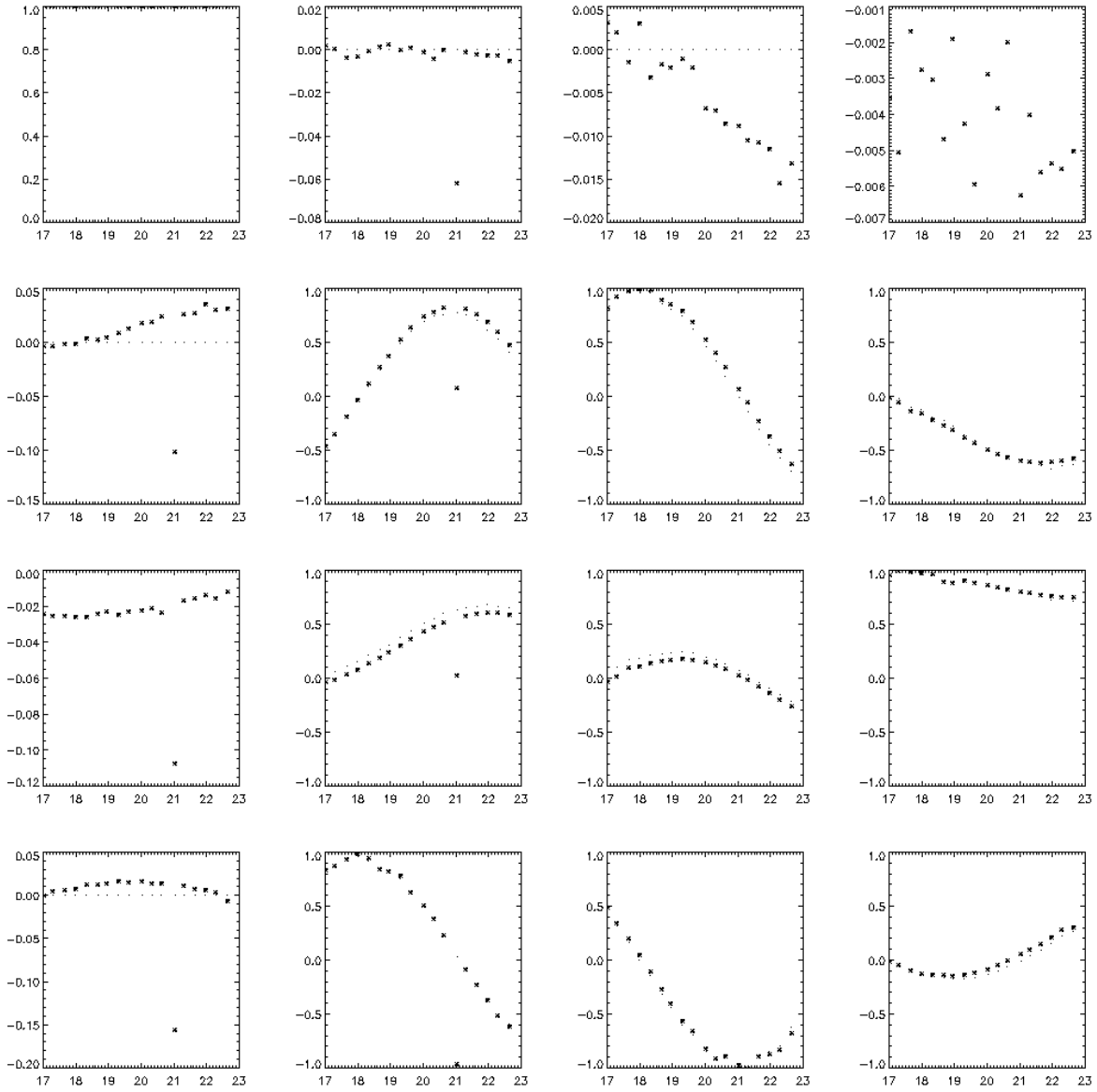
MUELLER MATRIX OF M3 AND BEHIND 05/20/12



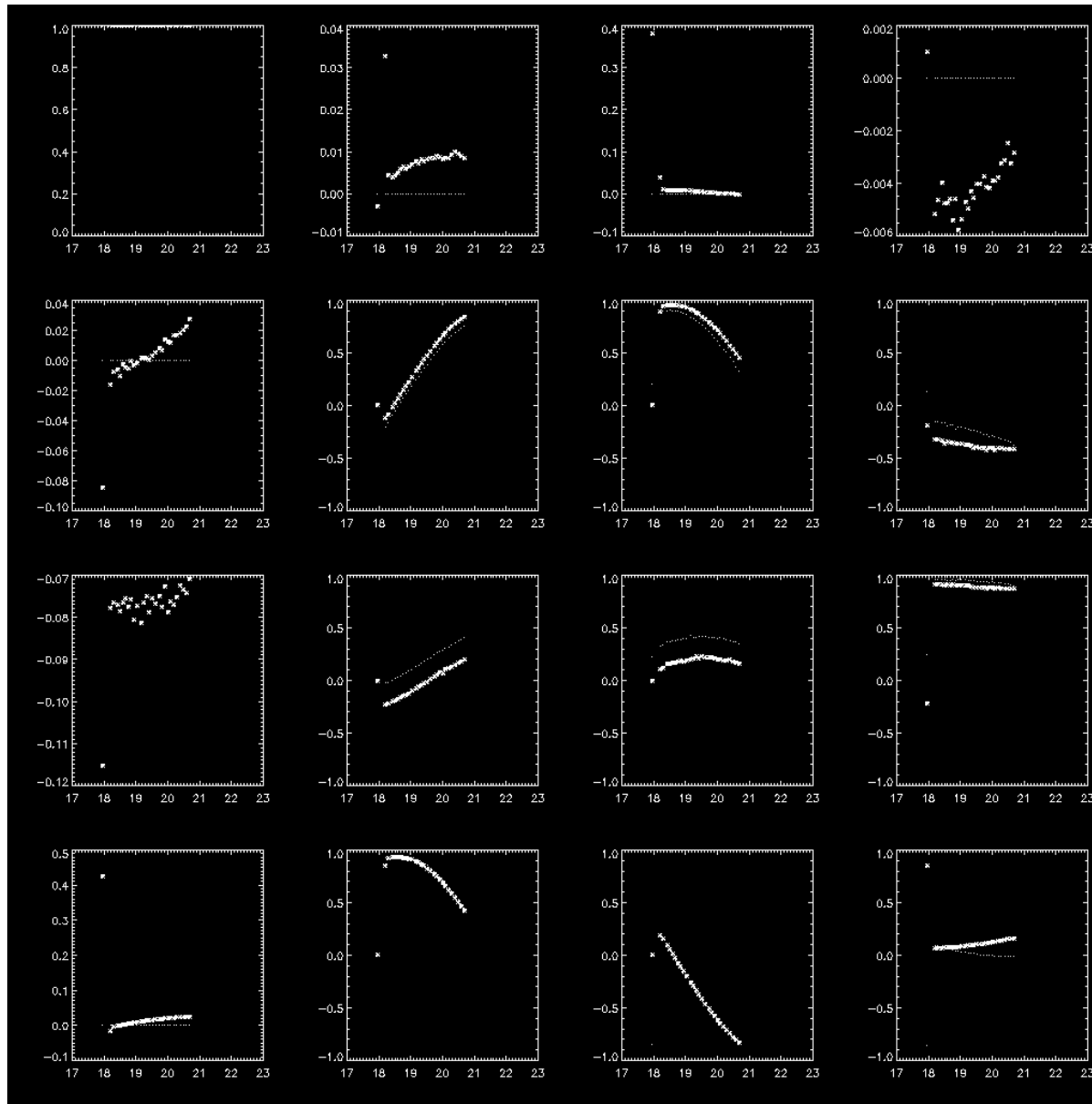
MODULATION W/ 12 HR PERIOD 06/06/12



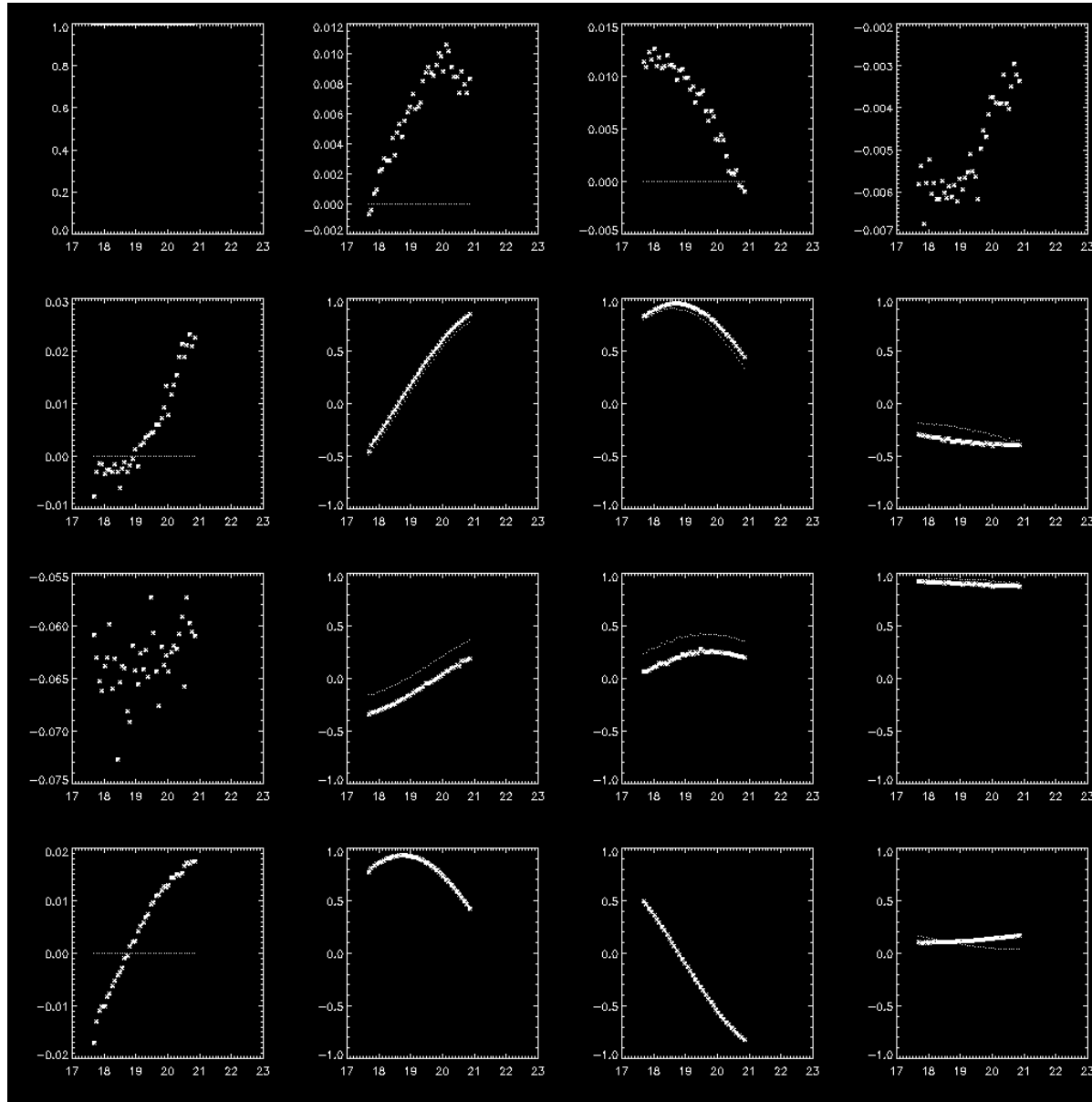
06/27/12



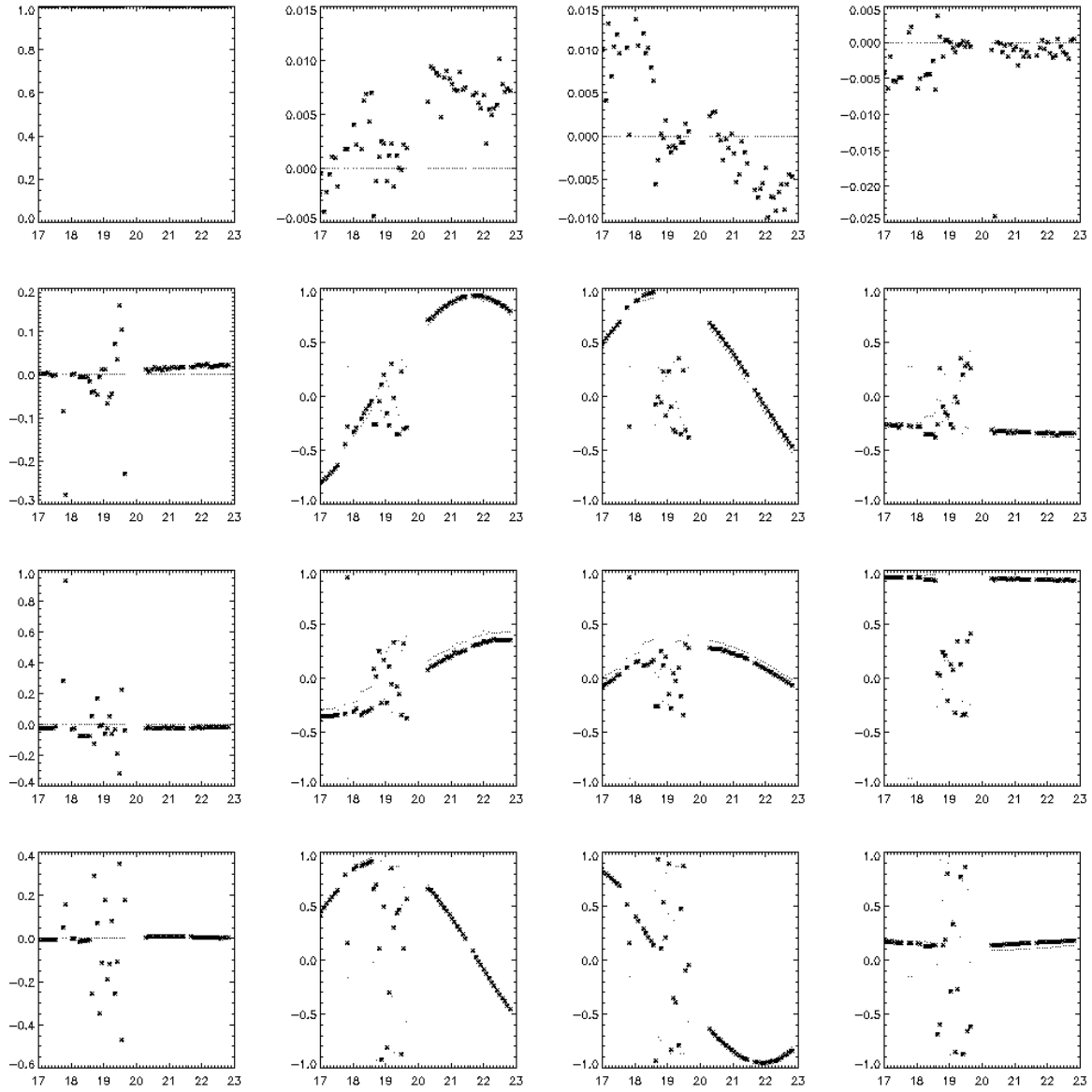
08/30/11



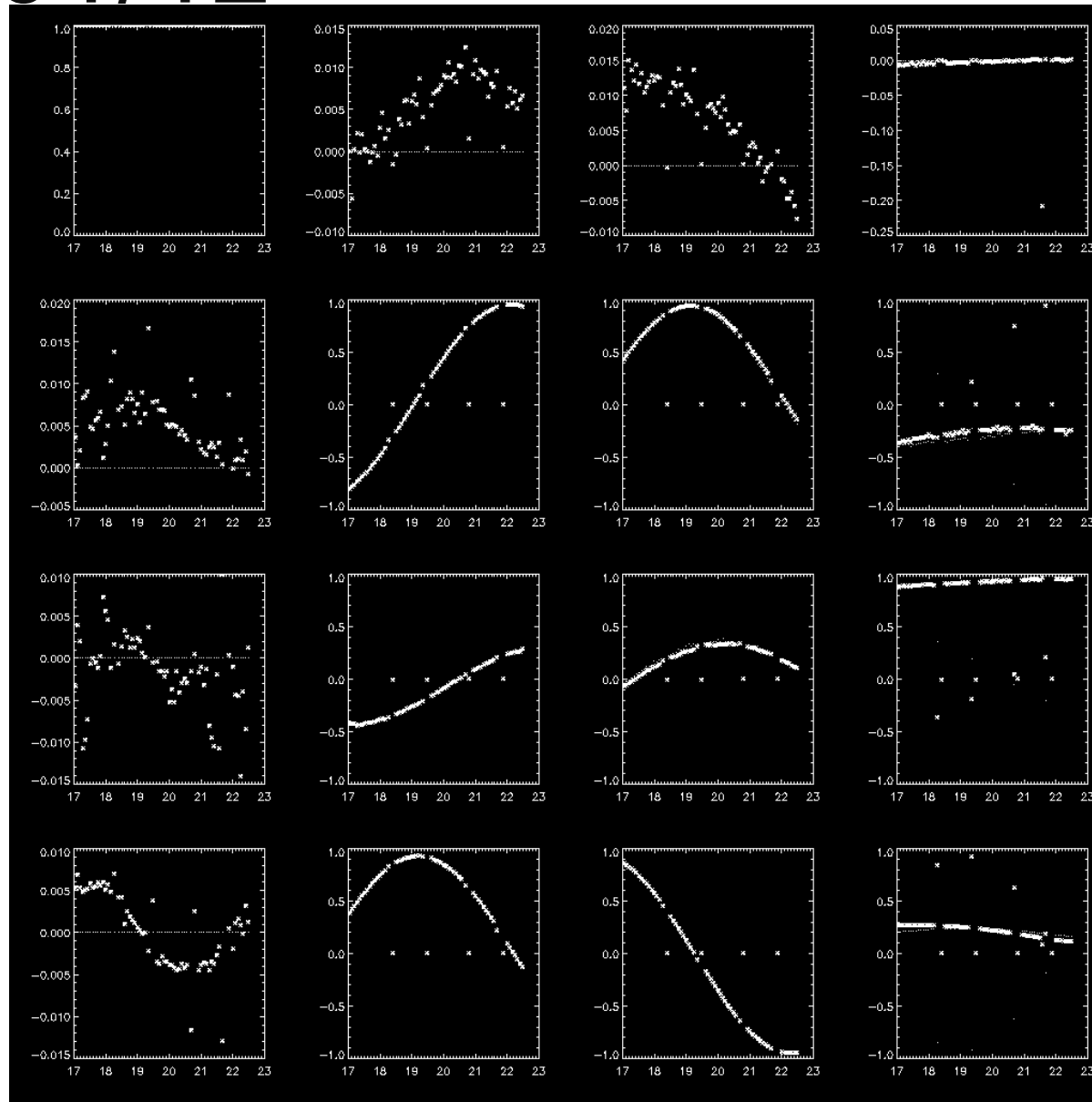
09/06/11



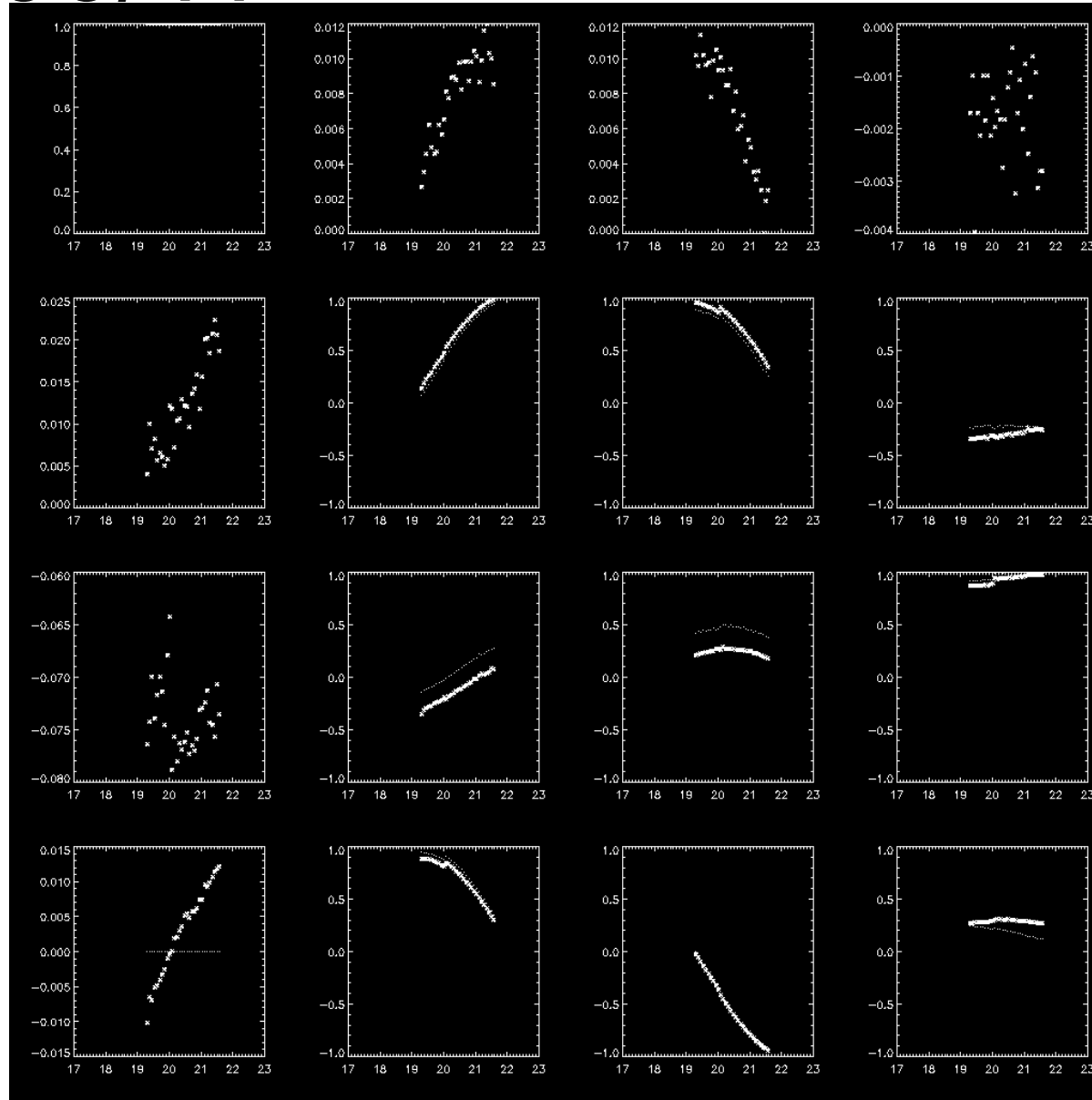
09/13/12



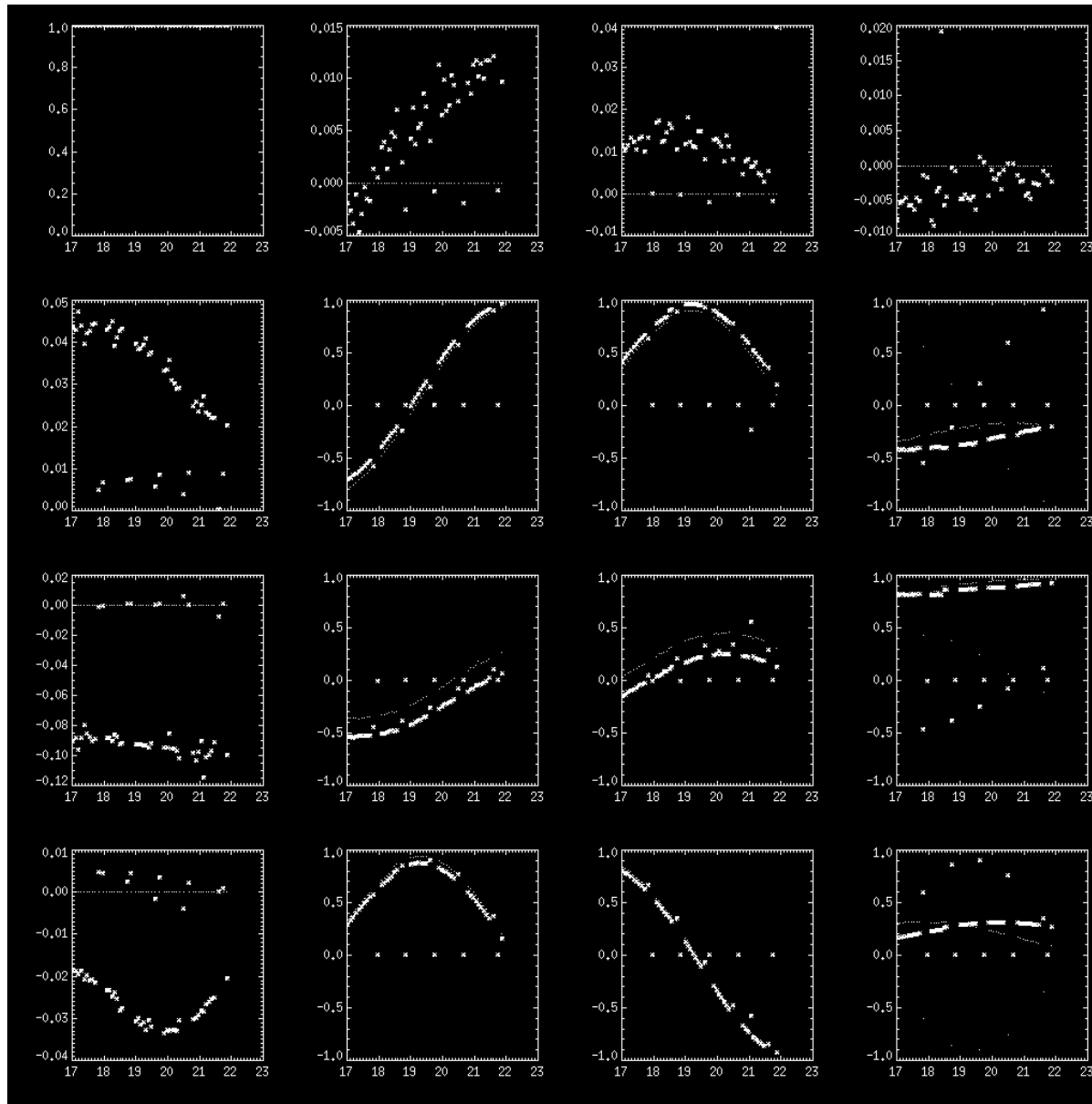
10/01/12



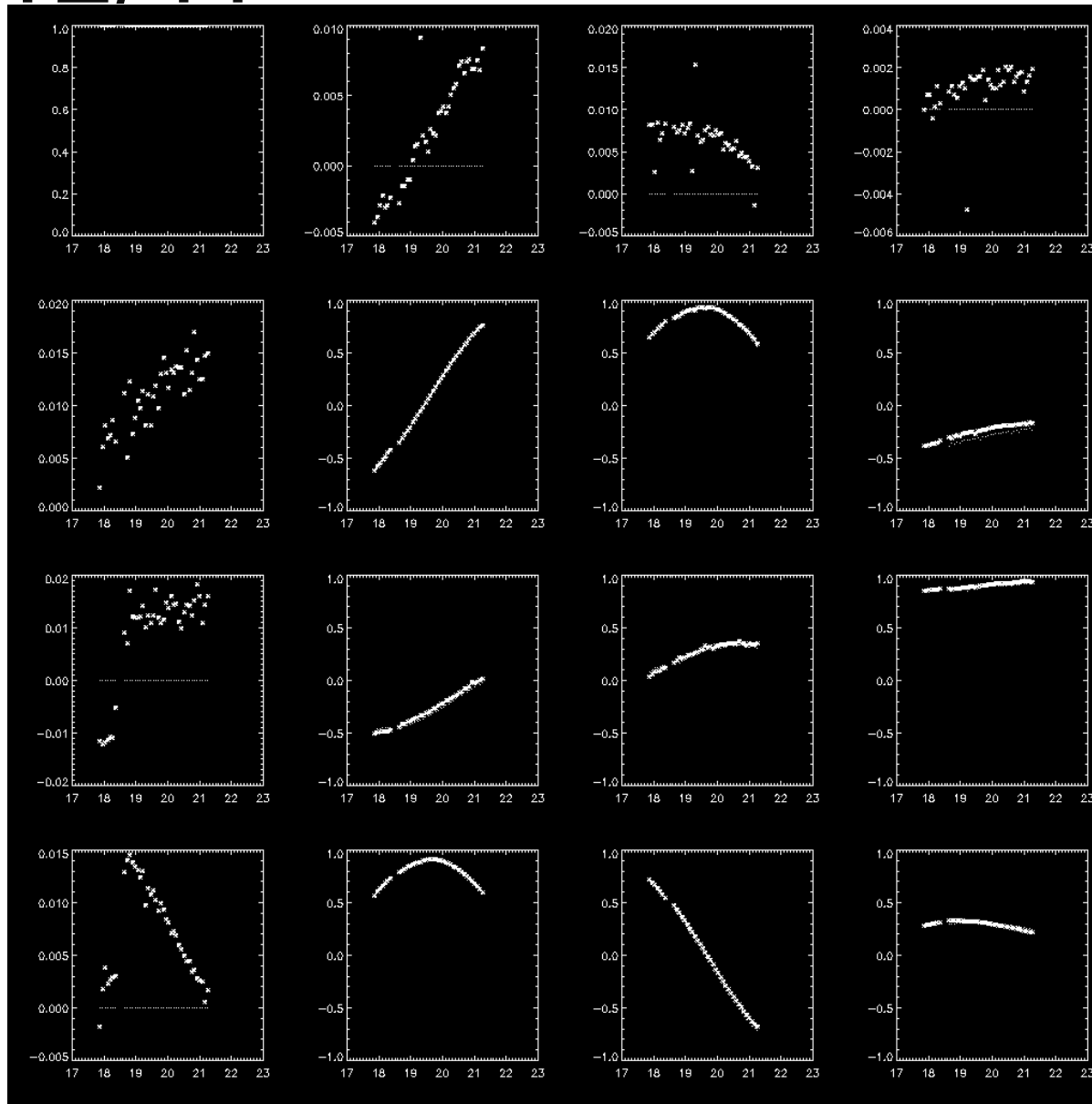
10/06/11



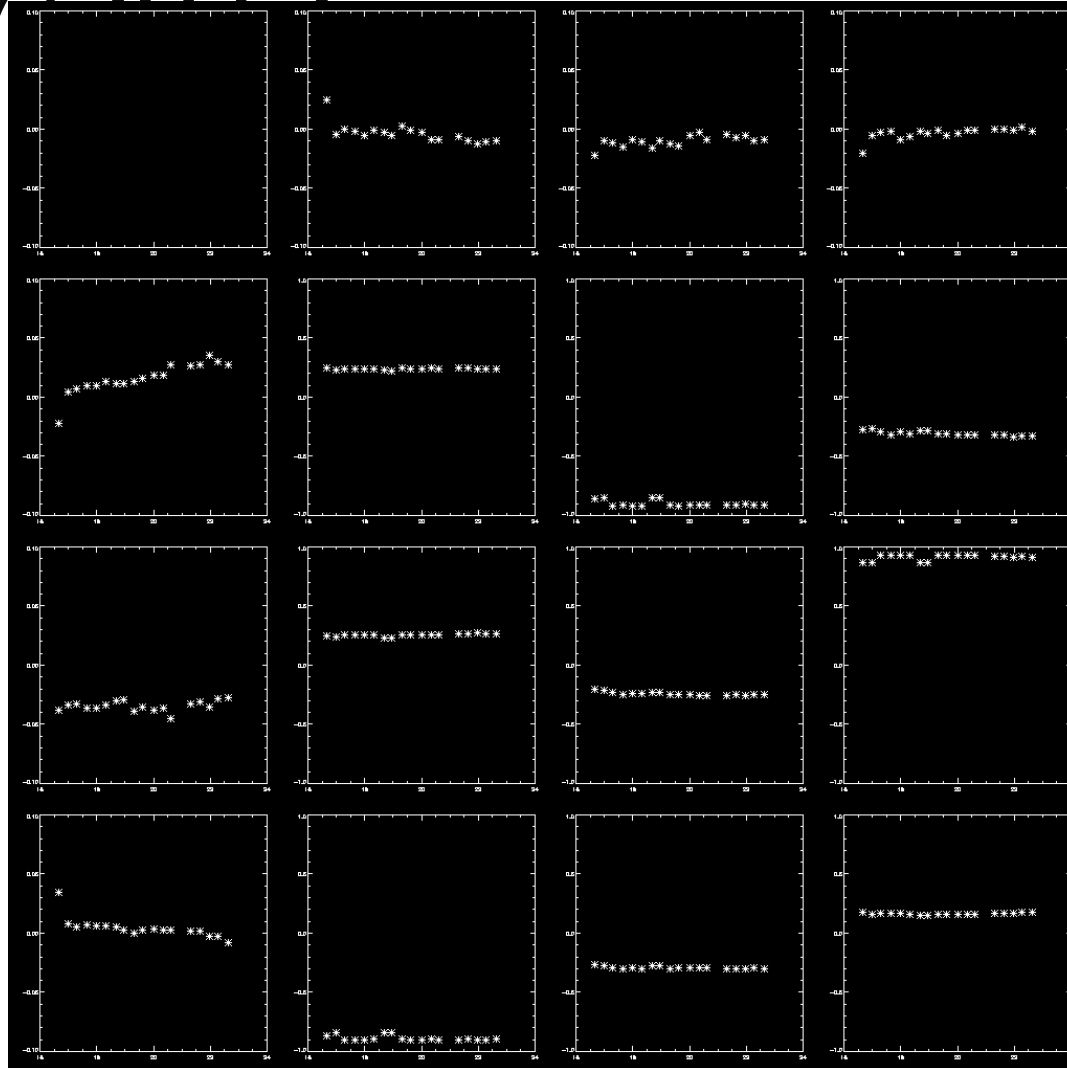
10/08/12



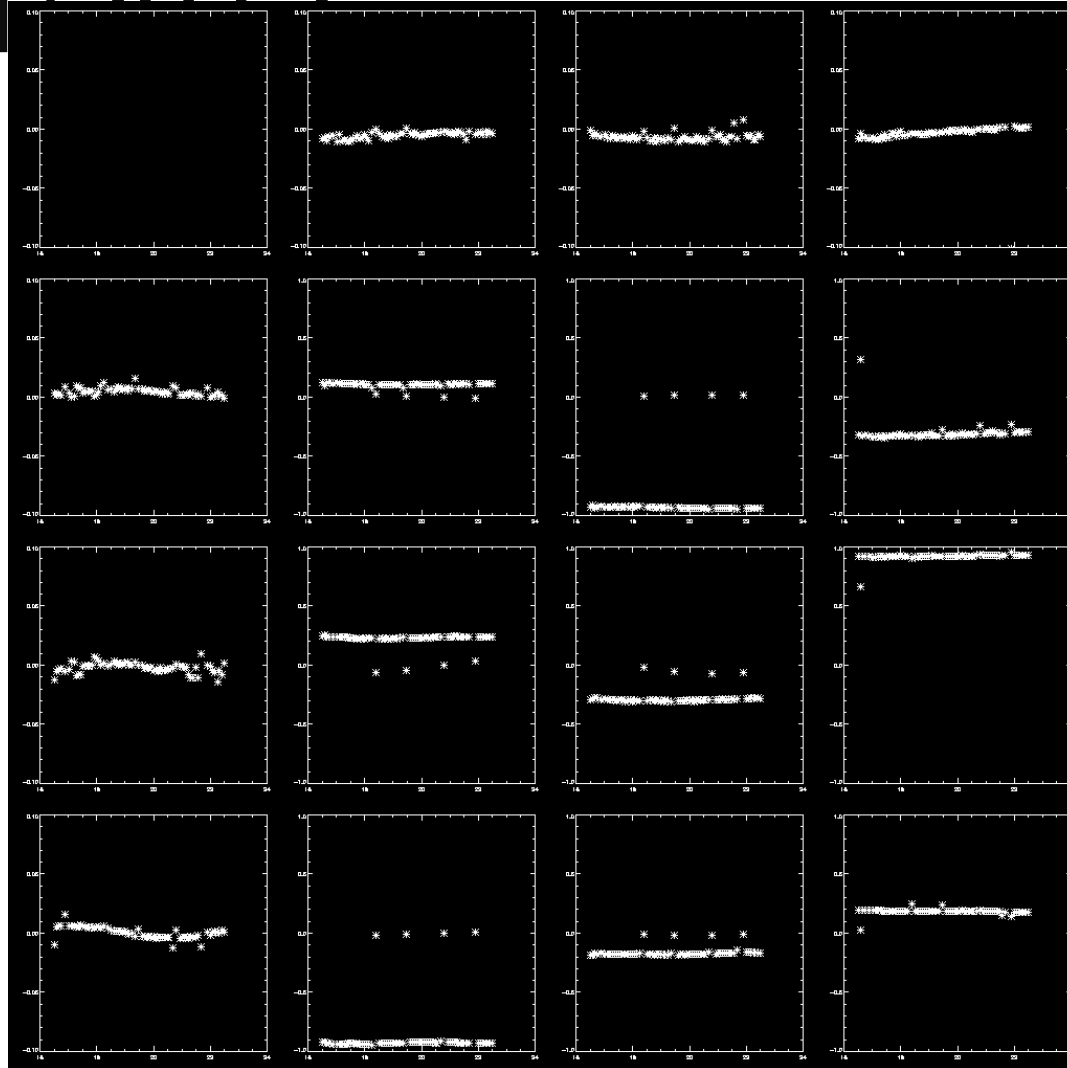
10/12/11



M_REST FROM 06/27/2012

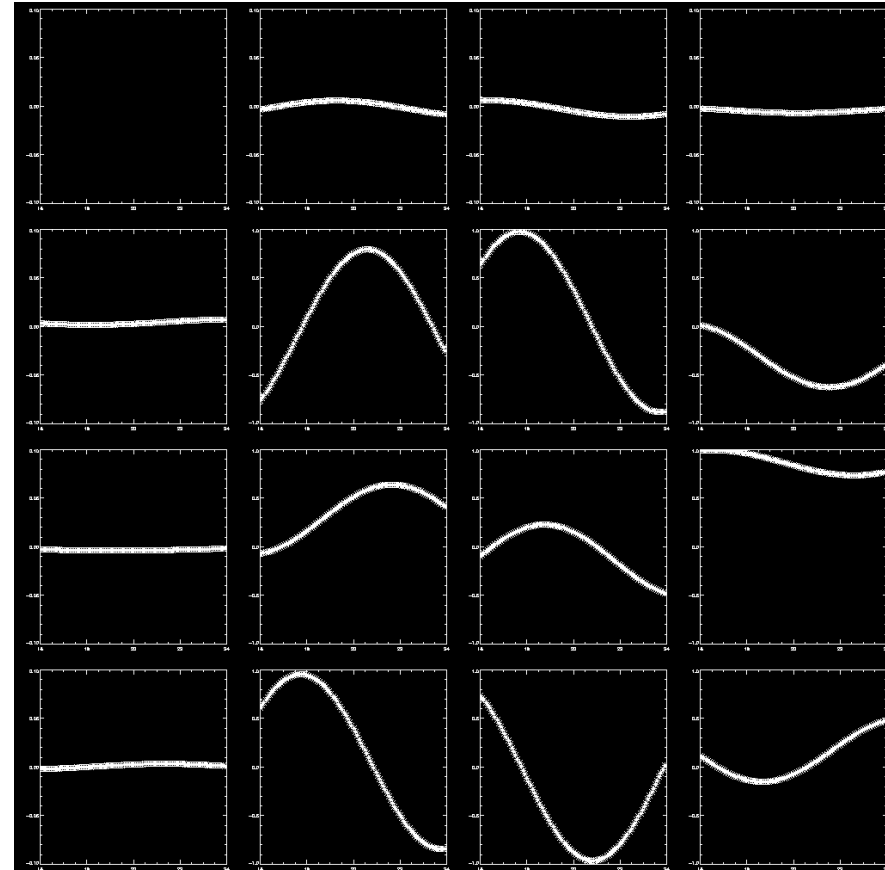
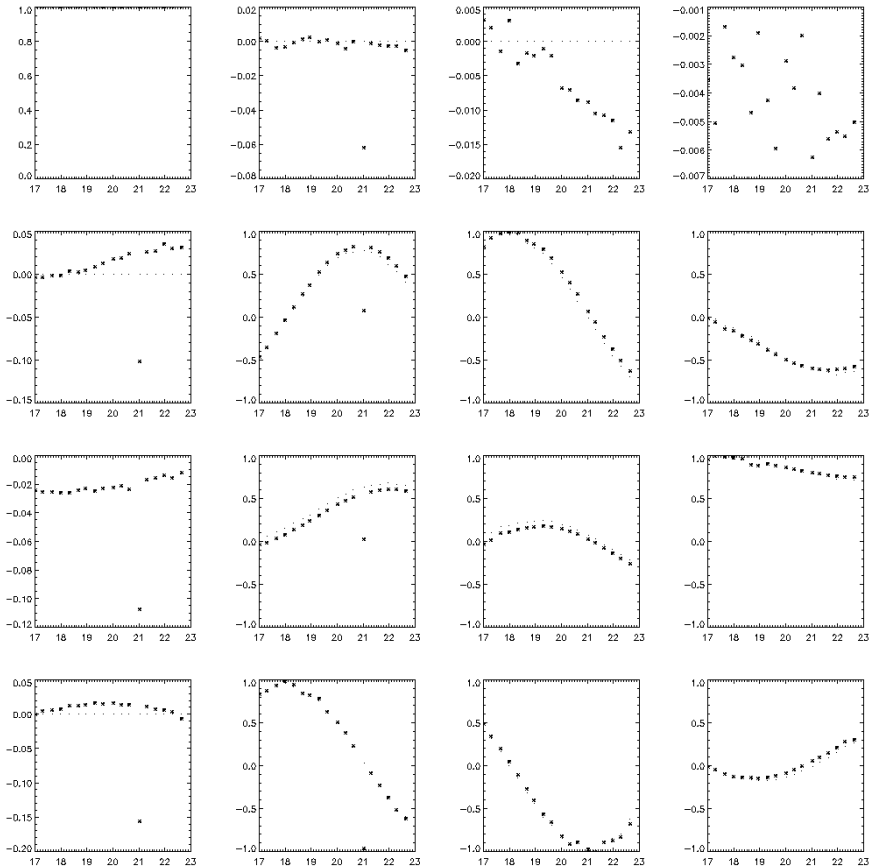


M_REST FROM 10/01/2012

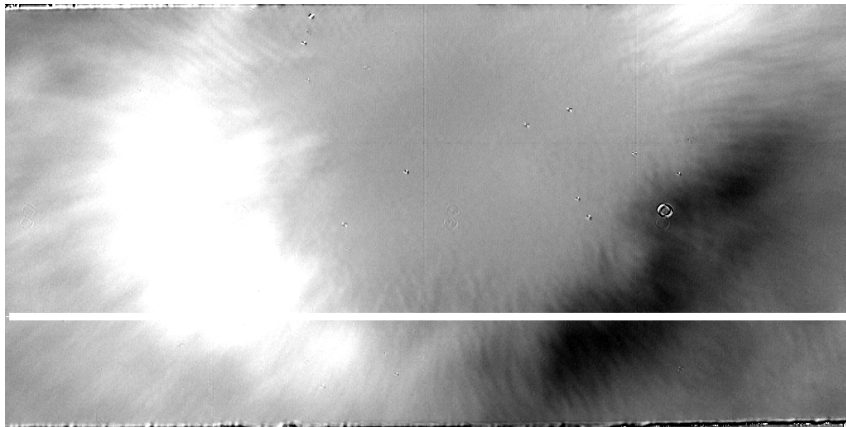


MEASURED VS. SIMULATED FROM M_REST

Calibration of 06/27 from the M_{rest} on 10/01

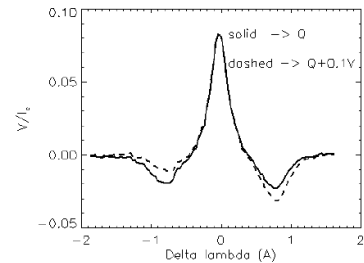
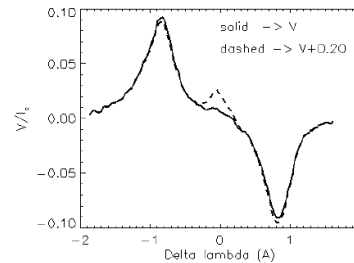
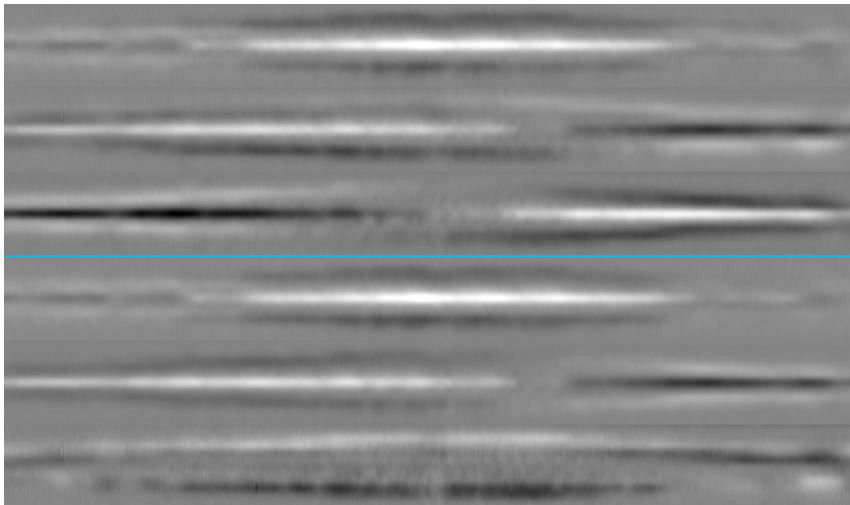


INDIRECT CALIBRATION



Kuhn et al. 1994

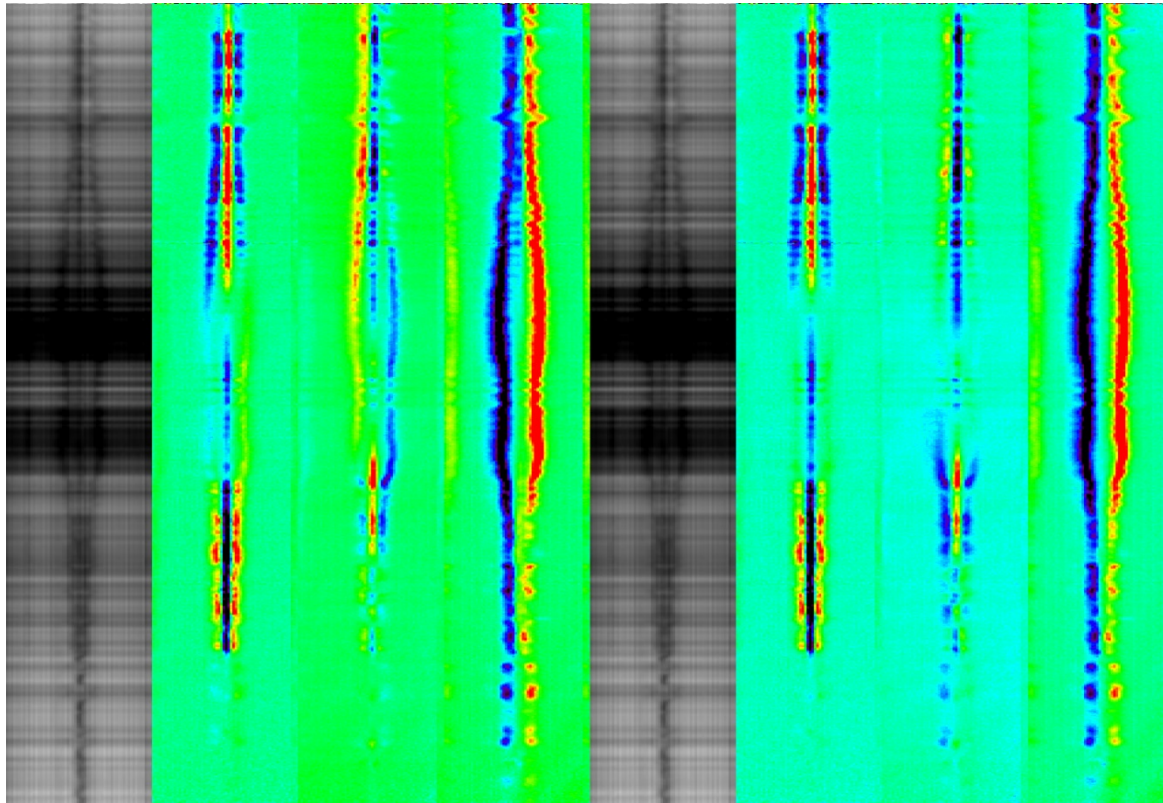
Contamination from the other Stokes parameters – breaking symmetry/anti-symmetry of spectral profiles



SECOND ORDER CALIBRATION

Subtract asymmetric contamination in Q, U

Subtract Q, U contribution from V



NIRIS STOKES PROCESSING REQUIREMENTS

IDL with astro package

Mpfit

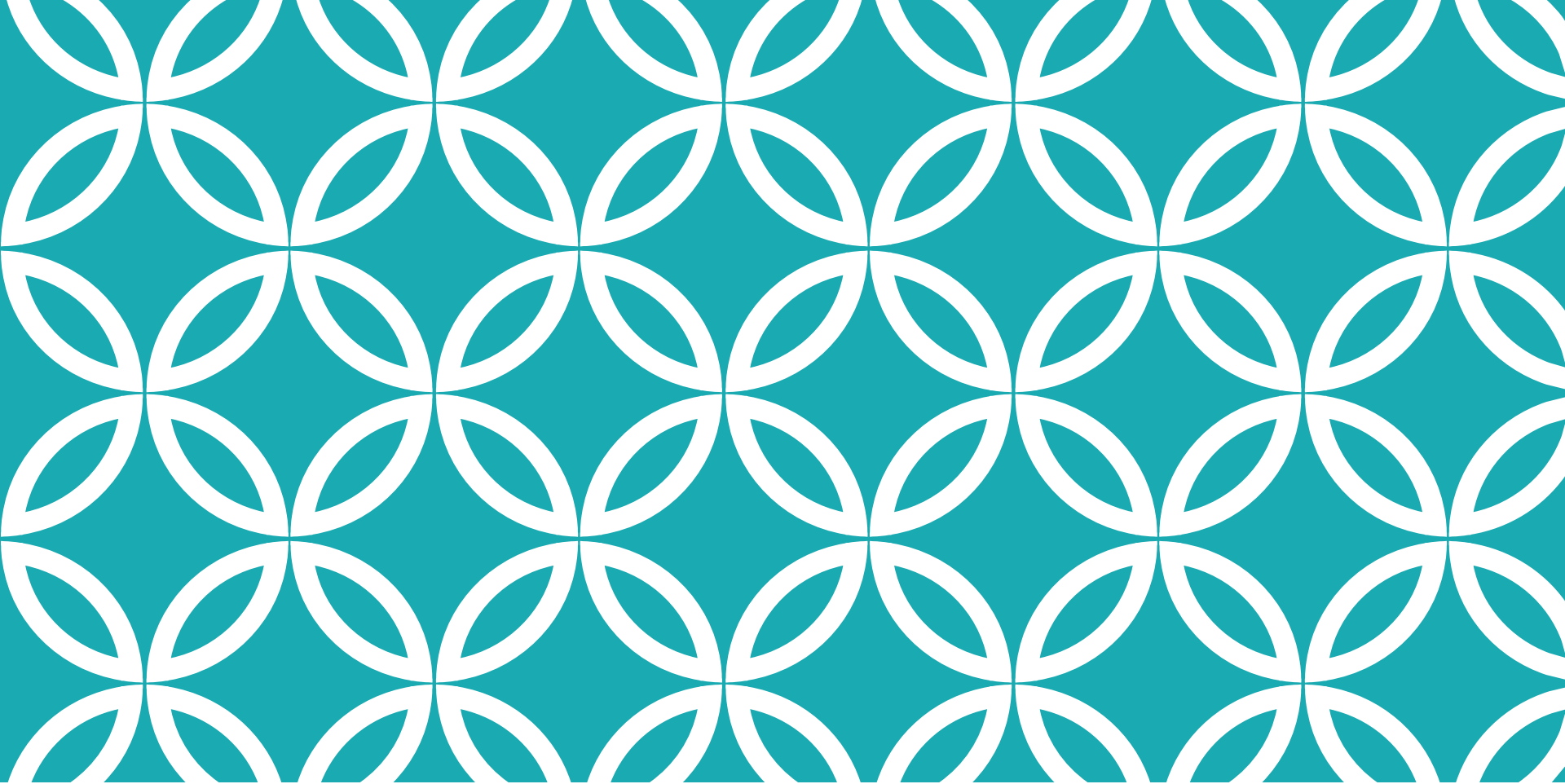
A couple of files we made

Fitsio for uncompressing

8 gb < memory space

4 < CPU cores

- For inversion, the more the better.



STOKES INVERSION TECHNIQUES



STOKES INVERSION

Fitting the model profiles into the measured profiles

The model profiles are outcome of physical parameters

The more the parameters, the more accurate fitting works, but harder to trust.

Milne-Eddington approximation

SIR – the most robust method probably for photospheric lines

STiC – non-LTE lines

Hazel – best for He 10830

And so on...

MILNE-EDDINGTON APPROXIMATION

The simplest inversion

Assumption:

1. There is no velocity gradient over optical depth – symmetric profiles
2. The source function is the 1st order polynomial over optical depth

Pros:

1. Analytical solution
2. Faster processing

Cons:

1. Cannot fit asymmetric profiles – only good for photospheric lines
2. Limited parameter outputs

which after some operation is transformed to

$$\frac{d}{d\tau} \left[-\frac{1}{4} v_B^2 \frac{\partial^2 I_0}{\partial v^2} \sin^2 \theta \cos 2\chi \right] = -\eta_0 \frac{1}{4} v_B^2 \frac{\partial^2 \phi_0}{\partial v^2} \sin^2 \theta \cos 2\chi (I - B_T) \quad (296)$$

$$-\frac{1}{4} v_B^2 (1 + \eta_0 \phi_0) \sin^2 \theta \cos 2\chi \frac{\partial^2 I_0}{\partial v^2} \quad (297)$$

We thus obtain

$$Q = -\frac{1}{4} v_B^2 \frac{\partial^2 I_0}{\partial v^2} \sin^2 \theta \cos 2\chi \quad (298)$$

and in the same way

$$U = -\frac{1}{4} v_B^2 \frac{\partial^2 I_0}{\partial v^2} \sin^2 \theta \sin 2\chi. \quad (299)$$

Finally we obtain simpler expressions

$$B_{\perp} \propto \frac{\sqrt{Q^2 + U^2}}{I} \quad (300)$$

$$\chi = \frac{1}{2} \tan^{-1} \frac{U}{Q} \quad (301)$$

5.2. Center-of-gravity method

Suppose magnetic field is aligned with the line of sight: $\theta = 0$. Then we have $\eta_Q = \eta_U = \rho_Q = \rho_U = 0$, and

$$\frac{dI}{d\tau} = \eta_I (I - B_T) + \eta_V V \quad (302)$$

$$\frac{dV}{d\tau} = \eta_V (I - B_T) + \eta_I V \quad (303)$$

which looks the same as the form derived from the first order weak field approximation. From these we obtain

$$\frac{d}{d\tau} (I + V) = (\eta_I + \eta_V) (I + V - B_T) \quad (304)$$

$$\frac{d}{d\tau} (I - V) = (\eta_I - \eta_V) (I - V - B_T) \quad (305)$$

or explicitly

$$\frac{d}{d\tau} (I + V) = (1 + \eta_0 \phi_0) (I + V - B_T) \quad (306)$$

$$\frac{d}{d\tau} (I - V) = (1 + \eta_0 \phi_0) (I - V - B_T). \quad (307)$$

The solutions of these equations are given by

$$I + V = I_0 (\lambda - g^* \lambda_B) \quad (308)$$

$$I - V = I_0 (\lambda + g^* \lambda_B) \quad (309)$$

where $I_0(\lambda)$ is the solution of the equation

$$\frac{dI_0}{d\tau} = (1 + \eta_0 \phi_0) (I_0 - B_T). \quad (310)$$

We define the center of gravity for $I + V$ by

$$\lambda_+ = \frac{\int (I_c - (I + V)) \lambda d\lambda}{\int (I_c - (I + V)) d\lambda} \quad (311)$$

and that for $I - V$ by

$$\lambda_- = \frac{\int (I_c - (I - V)) \lambda d\lambda}{\int (I_c - (I - V)) d\lambda} \quad (312)$$

where I_c is the continuum intensity. Suppose I_0 is symmetric about λ_0 , then the relations will hold

$$\lambda_{\pm} = \lambda_0 \pm g^* \lambda_B \quad (313)$$

so that we obtain

$$B_{\parallel} = \frac{1}{2G} (\lambda_+ - \lambda_-). \quad (314)$$

This expression holds even for inclined field, and does not suffer from the saturation effect.

5.3. Milne-Eddington Solution

$$\frac{d\mathbf{I}}{d\tau} = \mathbf{K} (I - B_T \mathbf{U}) \quad (315)$$

where $\mathbf{I} = (I, Q, U, V)$ and $\mathbf{U} = (1, 0, 0, 0)$.

Assumptions:

1. \mathbf{K} is constant over τ .
2. $B_T = B_0 + B_{1\tau}$

Assume a solution of the form

$$I = I_0 + I_1 \tau \quad (316)$$

$$I_1 = \mathbf{K}(I_0 - B_0 U + \tau(I_1 - B_1 U)) \quad (317)$$

$$I_1 = B_1 U \quad (318)$$

$$I_0 = B_0 U + B_1 \mathbf{K}^{-1} U \quad (319)$$

$$I = B_0 + B_1 \mathbf{K}^{-1} = B_0 + B_1 [\eta_I (\eta_I^2 + \rho_Q^2 + \rho_U^2 + \rho_V^2)] / \Delta \quad (320)$$

$$Q = B_1 \mathbf{K}_{\eta_I}^{-1} = -B_1 [\eta_I^2 \eta_Q + \eta_I (\eta_V \rho_U - \eta_U \rho_V) + \rho_Q (\eta_Q \rho_Q + \eta_U \rho_U + \eta_V \rho_V)] / \Delta \quad (321)$$

$$U = B_1 \mathbf{K}_{\eta_U}^{-1} = -B_1 [\eta_I^2 \eta_U + \eta_I (\eta_Q \rho_V - \eta_V \rho_Q) + \rho_U (\eta_Q \rho_Q + \eta_U \rho_U + \eta_V \rho_V)] / \Delta \quad (322)$$

$$V = B_1 \mathbf{K}_{\eta_V}^{-1} = -B_1 [\eta_I^2 \eta_V + \eta_I (\eta_U \rho_Q - \eta_Q \rho_U) + \rho_V (\eta_Q \rho_Q + \eta_U \rho_U + \eta_V \rho_V)] / \Delta \quad (323)$$

where $\Delta = \eta_I^2 [\eta_I^2 - \eta_Q^2 - \eta_U^2 - \eta_V^2 + \rho_Q^2 + \rho_U^2 + \rho_V^2] - (\eta_Q \rho_Q + \eta_U \rho_U + \eta_V \rho_V)^2$.

Free parameters: $B, \theta, \chi, \eta_0, \lambda_D, a, \lambda_0, B_0, B_1$.

5.3.1. Formulations for computation

Functional values

- Free parameters: $B, \theta, \chi, \eta_0, \lambda_D, a, \lambda_0, B_0, B_1$ among which $B, \eta_0, \lambda_D, a, B_0, B_1$ are positive definite:

2.

$$v = \frac{\lambda - \lambda_0}{\Delta \lambda_D} \quad (324)$$

$$v_B = c_0 \frac{B}{\Delta \lambda_D} \quad (325)$$

3.

$$\phi_p = H(a, v) \quad (326)$$

$$\phi_r = H(a, v - v_B) \quad (327)$$

$$\phi_b = H(a, v + v_B) \quad (328)$$

$$\psi_p = L(a, v) \quad (329)$$

$$\psi_r = L(a, v - v_B) \quad (330)$$

$$\psi_b = L(a, v + v_B) \quad (331)$$

4.

$$\eta_I = 1 + \eta_0 \frac{1}{2} \left[\phi_p \sin^2 \theta + \frac{\phi_b + \phi_r}{2} (1 + \cos^2 \theta) \right] \quad (332)$$

$$\eta_Q = \eta_0 \frac{1}{2} \left[\phi_p - \frac{\phi_b + \phi_r}{2} \right] \sin^2 \theta \cos 2\chi \quad (333)$$

$$\eta_U = \eta_0 \frac{1}{2} \left[\phi_p - \frac{\phi_b + \phi_r}{2} \right] \sin^2 \theta \sin 2\chi \quad (334)$$

$$\eta_V = \eta_0 \frac{1}{2} [\phi_r - \phi_b] \cos \theta \quad (335)$$

$$\rho_Q = \eta_0 \frac{1}{2} \left[\psi_p - \frac{\psi_b + \psi_r}{2} \right] \sin^2 \theta \cos 2\chi \quad (336)$$

$$\rho_U = \eta_0 \frac{1}{2} \left[\psi_p - \frac{\psi_b + \psi_r}{2} \right] \sin^2 \theta \sin 2\chi \quad (337)$$

$$\rho_V = \eta_0 \frac{1}{2} [\psi_r - \psi_b] \cos \theta \quad (338)$$

5.

$$\Delta = \eta_I^2 [\eta_I^2 - \eta_Q^2 - \eta_U^2 - \eta_V^2 + \rho_Q^2 + \rho_U^2 + \rho_V^2] - (\eta_Q \rho_Q + \eta_U \rho_U + \eta_V \rho_V)^2 \quad (339)$$

6.

$$I = B_0 + B_1 [\eta_I (\eta_I^2 + \rho_Q^2 + \rho_U^2 + \rho_V^2)] / \Delta \quad (340)$$

$$Q = -B_1 [\eta_I^2 \eta_Q + \eta_I (\eta_V \rho_U - \eta_U \rho_V) + \rho_Q (\eta_Q \rho_Q + \eta_U \rho_U + \eta_V \rho_V)] / \Delta \quad (341)$$

$$U = -B_1 [\eta_I^2 \eta_U + \eta_I (\eta_Q \rho_V - \eta_V \rho_Q) + \rho_U (\eta_Q \rho_Q + \eta_U \rho_U + \eta_V \rho_V)] / \Delta \quad (342)$$

$$V = -B_1 [\eta_I^2 \eta_V + \eta_I (\eta_U \rho_Q - \eta_Q \rho_U) + \rho_V (\eta_Q \rho_Q + \eta_U \rho_U + \eta_V \rho_V)] / \Delta \quad (343)$$

Partial derivative over η_I

$$\frac{\partial I}{\partial \eta_I} = B_1 (3\eta_I^2 + \rho_Q^2 + \rho_U^2 + \rho_V^2) / \Delta - (I - B_0) \frac{\partial \Delta}{\partial \eta_I} / \Delta \quad (344)$$

$$\frac{\partial I}{\partial \eta_Q} = -(I - B_0) \frac{\partial \Delta}{\partial \eta_Q} / \Delta \quad (345)$$

$$\frac{\partial I}{\partial \eta_U} = -(I - B_0) \frac{\partial \Delta}{\partial \eta_U} / \Delta \quad (346)$$

$$\frac{\partial I}{\partial \eta_V} = -(I - B_0) \frac{\partial \Delta}{\partial \eta_V} / \Delta \quad (347)$$

$$\frac{\partial I}{\partial \rho_Q} = B_1(2\eta_U \rho_Q) / \Delta - (I - B_0) \frac{\partial \Delta}{\partial \rho_Q} / \Delta \quad (348)$$

$$\frac{\partial I}{\partial \rho_U} = B_1(2\eta_U \rho_U) / \Delta - (I - B_0) \frac{\partial \Delta}{\partial \rho_U} / \Delta \quad (349)$$

$$\frac{\partial I}{\partial \rho_V} = B_1(2\eta_U \rho_V) / \Delta - (I - B_0) \frac{\partial \Delta}{\partial \rho_V} / \Delta \quad (350)$$

$$\frac{\partial Q}{\partial \eta_I} = -B_1[2\eta_U \eta_Q + (\eta_U \rho_U - \eta_U \rho_V)] / \Delta - Q \frac{\partial \Delta}{\partial \eta_I} / \Delta \quad (351)$$

$$\frac{\partial Q}{\partial \eta_Q} = -B_1[\eta_I^2 + \rho_Q^2] / \Delta - Q \frac{\partial \Delta}{\partial \eta_Q} / \Delta \quad (352)$$

$$\frac{\partial Q}{\partial \eta_U} = -B_1[-\eta_U \rho_V + \rho_Q \rho_U] / \Delta - Q \frac{\partial \Delta}{\partial \eta_U} / \Delta \quad (353)$$

$$\frac{\partial Q}{\partial \eta_V} = -B_1[\eta_U \rho_U + \rho_Q \rho_V] / \Delta - Q \frac{\partial \Delta}{\partial \eta_V} / \Delta \quad (354)$$

$$\frac{\partial Q}{\partial \rho_Q} = -B_1[2\eta_Q \rho_Q + \eta_U \rho_U + \eta_V \rho_V] / \Delta - Q \frac{\partial \Delta}{\partial \rho_Q} / \Delta \quad (355)$$

$$\frac{\partial Q}{\partial \rho_U} = -B_1[\eta_U \rho_U + \rho_Q \eta_U] / \Delta - Q \frac{\partial \Delta}{\partial \rho_U} / \Delta \quad (356)$$

$$\frac{\partial Q}{\partial \rho_V} = -B_1[-\eta_U \rho_U + \rho_Q \eta_V] / \Delta - Q \frac{\partial \Delta}{\partial \rho_V} / \Delta \quad (357)$$

$$\frac{\partial U}{\partial \eta_I} = -B_1[2\eta_U \eta_U + (\eta_Q \rho_U - \eta_V \rho_Q)] / \Delta - U \frac{\partial \Delta}{\partial \eta_I} / \Delta \quad (358)$$

$$\frac{\partial U}{\partial \eta_Q} = -B_1[\eta_U \rho_V + \rho_V \rho_Q] / \Delta - U \frac{\partial \Delta}{\partial \eta_Q} / \Delta \quad (359)$$

$$\frac{\partial U}{\partial \eta_V} = -B_1[\eta_I^2 + \rho_U^2] / \Delta - U \frac{\partial \Delta}{\partial \eta_V} / \Delta \quad (360)$$

$$\frac{\partial U}{\partial \eta_U} = -B_1[-\eta_U \rho_Q + \rho_U \rho_V] / \Delta - U \frac{\partial \Delta}{\partial \eta_U} / \Delta \quad (361)$$

$$\frac{\partial U}{\partial \rho_Q} = -B_1[-\eta_U \rho_V + \rho_U \eta_Q] / \Delta - U \frac{\partial \Delta}{\partial \rho_Q} / \Delta \quad (362)$$

$$\frac{\partial U}{\partial \rho_U} = -B_1[\eta_Q \rho_Q + \eta_U \rho_U + \eta_V \rho_V + \rho_U \eta_U] / \Delta - U \frac{\partial \Delta}{\partial \rho_U} / \Delta \quad (363)$$

$$\frac{\partial U}{\partial \rho_V} = -B_1[\eta_U \eta_Q + \rho_U \eta_V] / \Delta - U \frac{\partial \Delta}{\partial \rho_V} / \Delta \quad (364)$$

$$\frac{\partial V}{\partial \eta_I} = -B_1[2\eta_U \eta_V + (\eta_U \rho_Q - \eta_Q \rho_U)] / \Delta - V \frac{\partial \Delta}{\partial \eta_I} / \Delta \quad (365)$$

$$\frac{\partial V}{\partial \eta_Q} = -B_1[-\eta_U \rho_V + \rho_V \rho_Q] / \Delta - V \frac{\partial \Delta}{\partial \eta_Q} / \Delta \quad (366)$$

$$\frac{\partial V}{\partial \eta_U} = -B_1[\eta_U \rho_Q + \rho_V \rho_U] / \Delta - V \frac{\partial \Delta}{\partial \eta_U} / \Delta \quad (367)$$

$$\frac{\partial V}{\partial \eta_V} = -B_1[\eta_I^2 + \rho_V^2] / \Delta - V \frac{\partial \Delta}{\partial \eta_V} / \Delta \quad (368)$$

$$\frac{\partial V}{\partial \rho_Q} = -B_1[\eta_U \eta_V + \rho_V \eta_Q] / \Delta - V \frac{\partial \Delta}{\partial \rho_Q} / \Delta \quad (369)$$

$$\frac{\partial V}{\partial \rho_U} = -B_1[-\eta_U \eta_Q + \rho_U \eta_U] / \Delta - V \frac{\partial \Delta}{\partial \rho_U} / \Delta \quad (370)$$

$$\frac{\partial V}{\partial \rho_V} = -B_1[\eta_U \rho_U + \eta_U \rho_U + 2\eta_V \rho_V] / \Delta - V \frac{\partial \Delta}{\partial \rho_V} / \Delta \quad (371)$$

$$(372)$$

$$\frac{\partial \Delta}{\partial \eta_I} = 2\eta_U[2\eta_I^2 - \eta_Q^2 - \eta_U^2 - \eta_V^2 + \rho_Q^2 + \rho_U^2 + \rho_V^2] \quad (373)$$

$$\frac{\partial \Delta}{\partial \eta_Q} = -2\eta_I^2 \eta_Q - 2\rho_Q(\eta_Q \rho_Q + \eta_U \rho_U + \eta_V \rho_V) \quad (374)$$

$$\frac{\partial \Delta}{\partial \eta_U} = -2\eta_I^2 \eta_U - 2\rho_U(\eta_Q \rho_Q + \eta_U \rho_U + \eta_V \rho_V) \quad (375)$$

$$\frac{\partial \Delta}{\partial \eta_V} = -2\eta_I^2 \eta_V - 2\rho_V(\eta_Q \rho_Q + \eta_U \rho_U + \eta_V \rho_V) \quad (376)$$

$$\frac{\partial \Delta}{\partial \rho_Q} = 2\eta_I^2 \rho_Q - 2\eta_Q(\eta_Q \rho_Q + \eta_U \rho_U + \eta_V \rho_V) \quad (377)$$

$$\frac{\partial \Delta}{\partial \rho_U} = 2\eta_I^2 \rho_U - 2\eta_U(\eta_Q \rho_Q + \eta_U \rho_U + \eta_V \rho_V) \quad (378)$$

$$\frac{\partial \Delta}{\partial \rho_V} = 2\eta_I^2 \rho_V - 2\eta_V(\eta_Q \rho_Q + \eta_U \rho_U + \eta_V \rho_V) \quad (379)$$

$$(380)$$

partial derivative over B

$$\frac{\partial I}{\partial B} = \left[\frac{\partial I}{\partial \eta_I} \frac{\partial \eta_I}{\partial v_B} + \frac{\partial I}{\partial \eta_Q} \frac{\partial \eta_Q}{\partial v_B} + \frac{\partial I}{\partial \eta_U} \frac{\partial \eta_U}{\partial v_B} + \frac{\partial I}{\partial \eta_V} \frac{\partial \eta_V}{\partial v_B} \right. \quad (381)$$

$$\left. + \frac{\partial I}{\partial \rho_Q} \frac{\partial \rho_Q}{\partial v_B} + \frac{\partial I}{\partial \rho_U} \frac{\partial \rho_U}{\partial v_B} + \frac{\partial I}{\partial \rho_V} \frac{\partial \rho_V}{\partial v_B} \right] \frac{\partial v_B}{\partial B} \quad (382)$$

GOOD LUCK!

- 38 -

Partial derivative over B_0

$$\frac{\partial I}{\partial B_0} = 1 \quad (383)$$

$$\frac{\partial Q}{\partial B_0} = 0 \quad (384)$$

$$\frac{\partial U}{\partial B_0} = 0 \quad (385)$$

$$\frac{\partial V}{\partial B_0} = 0 \quad (386)$$

Partial derivative over B_1

$$\frac{\partial I}{\partial B_1} = (I - B_0)/B_1 \quad (387)$$

$$\frac{\partial Q}{\partial B_1} = Q/B_1 \quad (388)$$

$$\frac{\partial U}{\partial B_1} = U/B_1 \quad (389)$$

$$\frac{\partial V}{\partial B_1} = V/B_1 \quad (390)$$

5.3.2. Simultaneous Fitting of Doublets

The magnetic parameters B , θ , χ and atmospheric parameters B_0 , B_1 are independent of the lines. For doublets, λ_D and a are the same in both the lines.

If the central wavelength position of Fe I 6301.5 is denoted by λ_0 , then the central wavelength position of Fe I 6302.5 is $\lambda_0 + \delta\lambda$ with $\delta\lambda = 0.991 \text{ \AA}$.

If the ratio of the line center opacity of Fe I 6301.5 is η_0 , then that of Fe I 6302.5 is $q\eta_0$ with $q = 0.5$.

A very important feature is that the two lines have different values of effective Lande-g factor.

Functional values

- Free parameters: B , θ , χ , η_0 , λ_D , a , λ_0 , B_0 , B_1 among which B , η_0 , λ_D , a , B_0 , B_1 are positive definite.

- 39 -

$$2. \quad v = \frac{\lambda - \lambda_0}{\Delta\lambda_D}, \quad v_1 = \frac{\lambda - \lambda_0 - \delta\lambda}{\Delta\lambda_D} \quad (391)$$

$$v_B = c_0 \frac{B}{\Delta\lambda_D}, \quad v_{B1} = r v_B \quad (392)$$

$$3. \quad \phi_p = H(a, v) + qH(a, v_1) \quad (393)$$

$$\phi_r = H(a, v - v_B) + qH(a, v_1 - v_{B1}) \quad (394)$$

$$\phi_b = H(a, v + v_B) + qH(a, v_1 + v_{B1}) \quad (395)$$

$$\psi_p = L(a, v) + qL(a, v_1) \quad (396)$$

$$\psi_r = L(a, v - v_B) + qL(a, v_1 - v_{B1}) \quad (397)$$

$$\psi_b = L(a, v + v_B) + qL(a, v_1 + v_{B1}) \quad (398)$$

5.4. Filling factor effect

Suppose an areal fraction α of the spatial resolution element is occupied by an unresolved magnetic structure and the rest by non-magnetic structures. Then observed Stokes parameters are given by

$$I = \alpha I_m + (1 - \alpha) I_{nm} \quad (399)$$

where $I_{nm} = (I_{nm}, 0, 0, 0)$. Explicitly we have

$$I = \alpha I_m + (1 - \alpha) I_{nm} \quad (400)$$

$$V = \alpha V_m \quad (401)$$

$$Q = \alpha Q_m \quad (402)$$

$$U = \alpha U_m \quad (403)$$

Using the weak field solution

$$V_m = -CB_2 \frac{d(I_0)_m}{d\lambda}, \quad (404)$$

we find

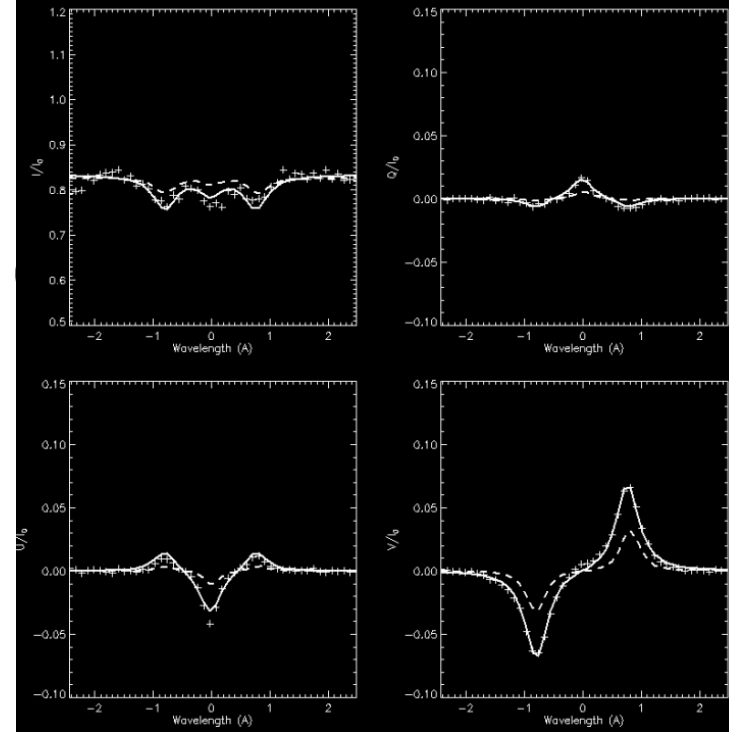
$$V = \alpha V_m = -\alpha\beta CB_2 \frac{d(I_0)_{nm}}{d\lambda} \quad (405)$$

and

$$(B_1)_{app} = \alpha\beta B_1 \quad (406)$$

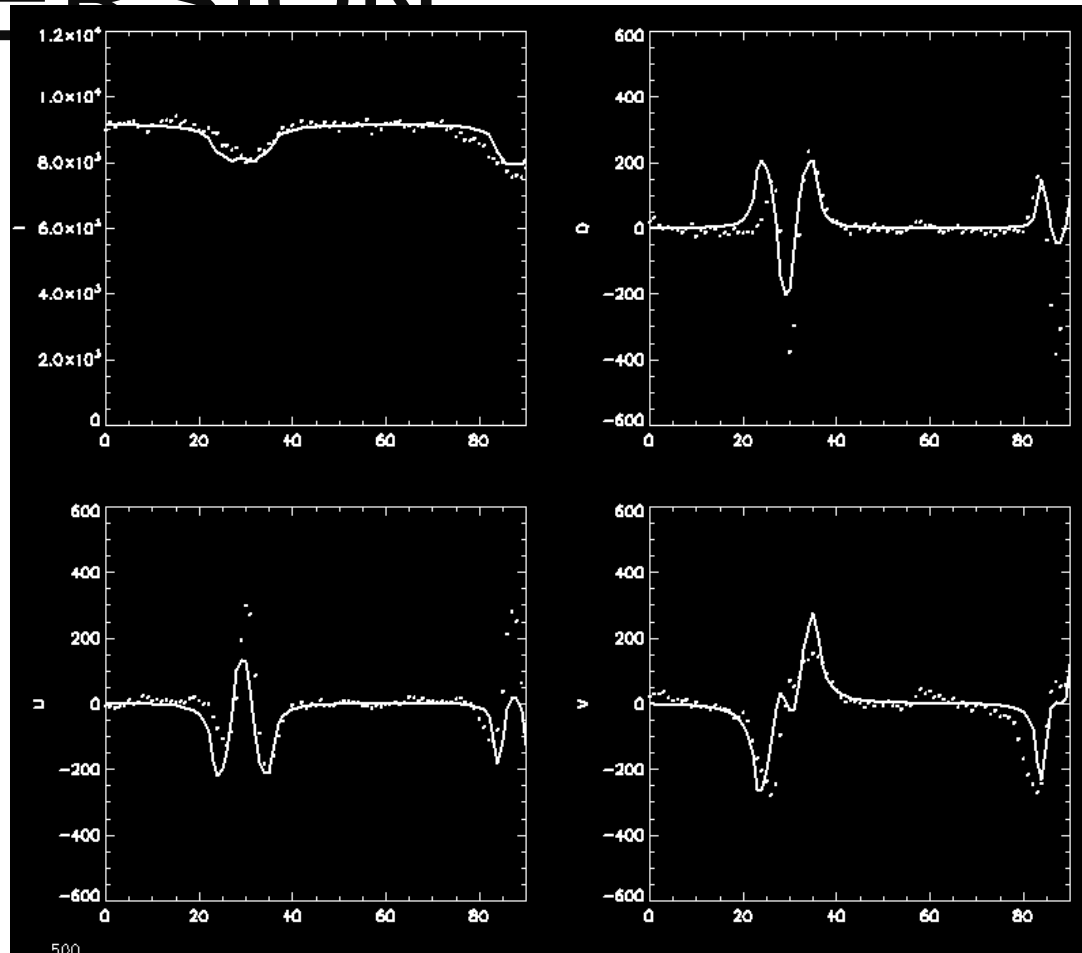
STOKES INVERSI

Applying Chae's ME singlet inversion code
used for Hinode/SP

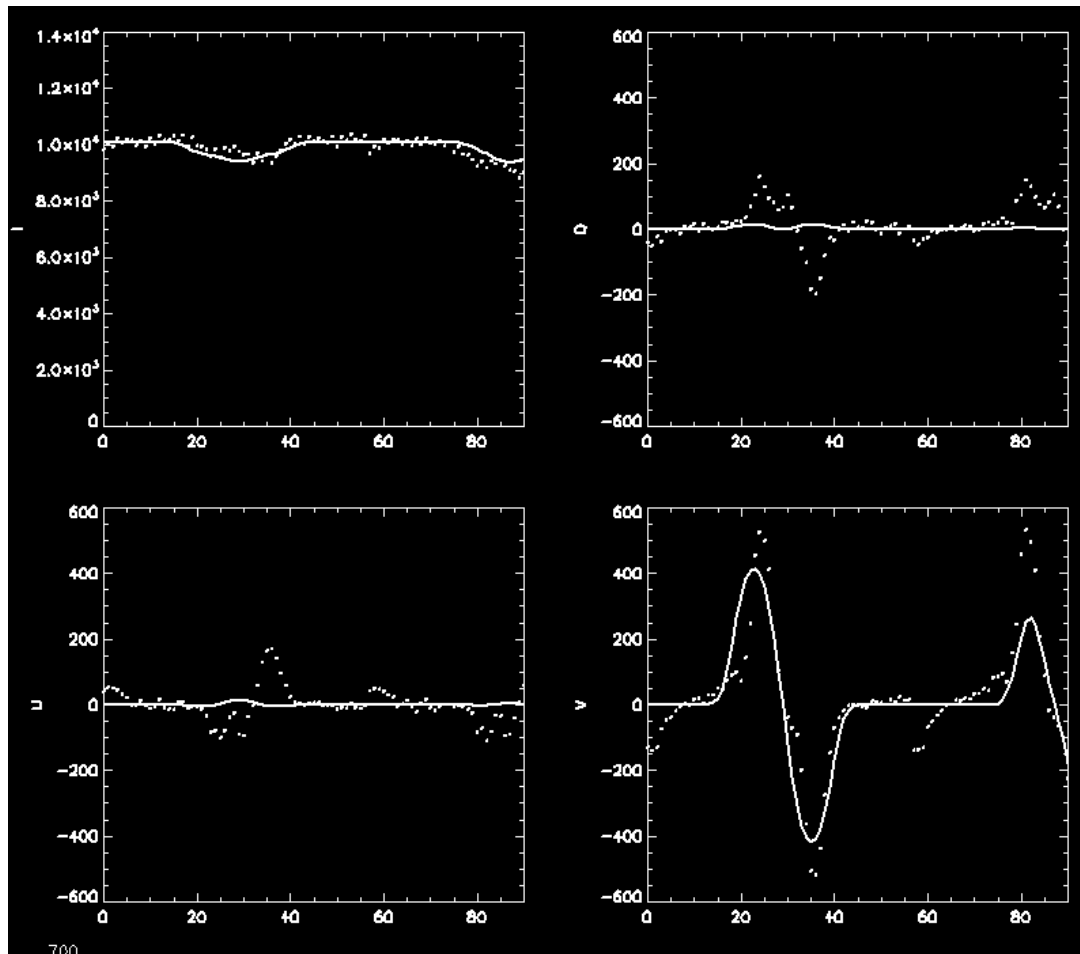


- B = par[0] ; magnetic field strength in Gauss
- theta = par[1] ; inclination in radian
- chi = par[2] ; azimuth in radian
- eta0 = par[3] ; ratio of line center opacity to the continuum one
- dlambdaD= par[4] ; Doppler width in angstrom
- a = par[5] ; damping parameter
- lambda0 = par[6] ; line center in A (Doppler shift)
- B0 = par[7] ; zeroth order of the source function
- B1 = par[8] ; first order of the source function
- I = par[9] ; intensity in ADU

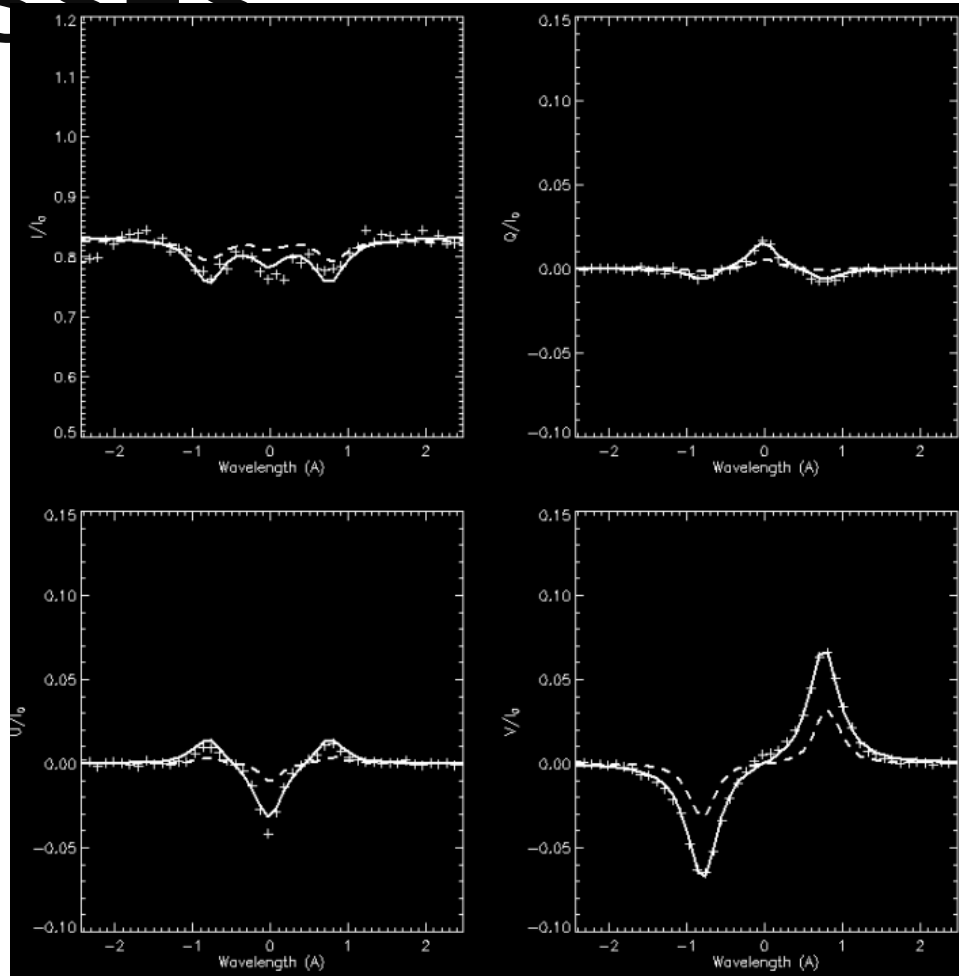
SUCCESSFUL INVERSION



INVERSION FAILURE

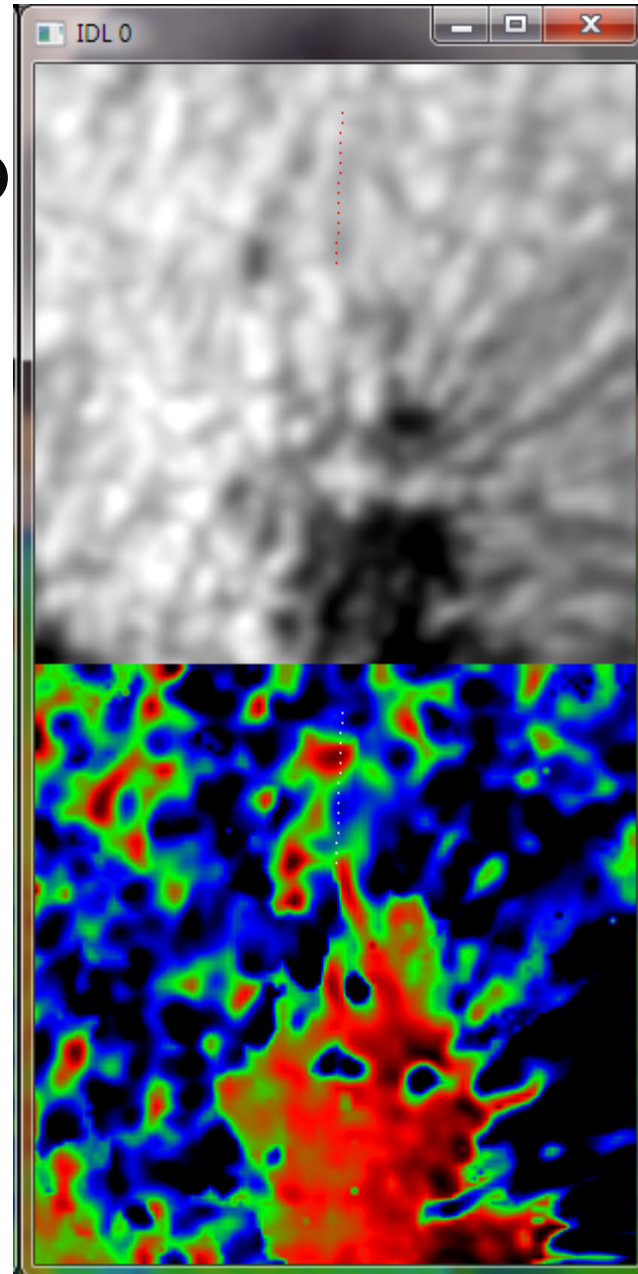


SUCCESSFUL INVERSION WITH ADAPTIVE INITIAL GUESSES

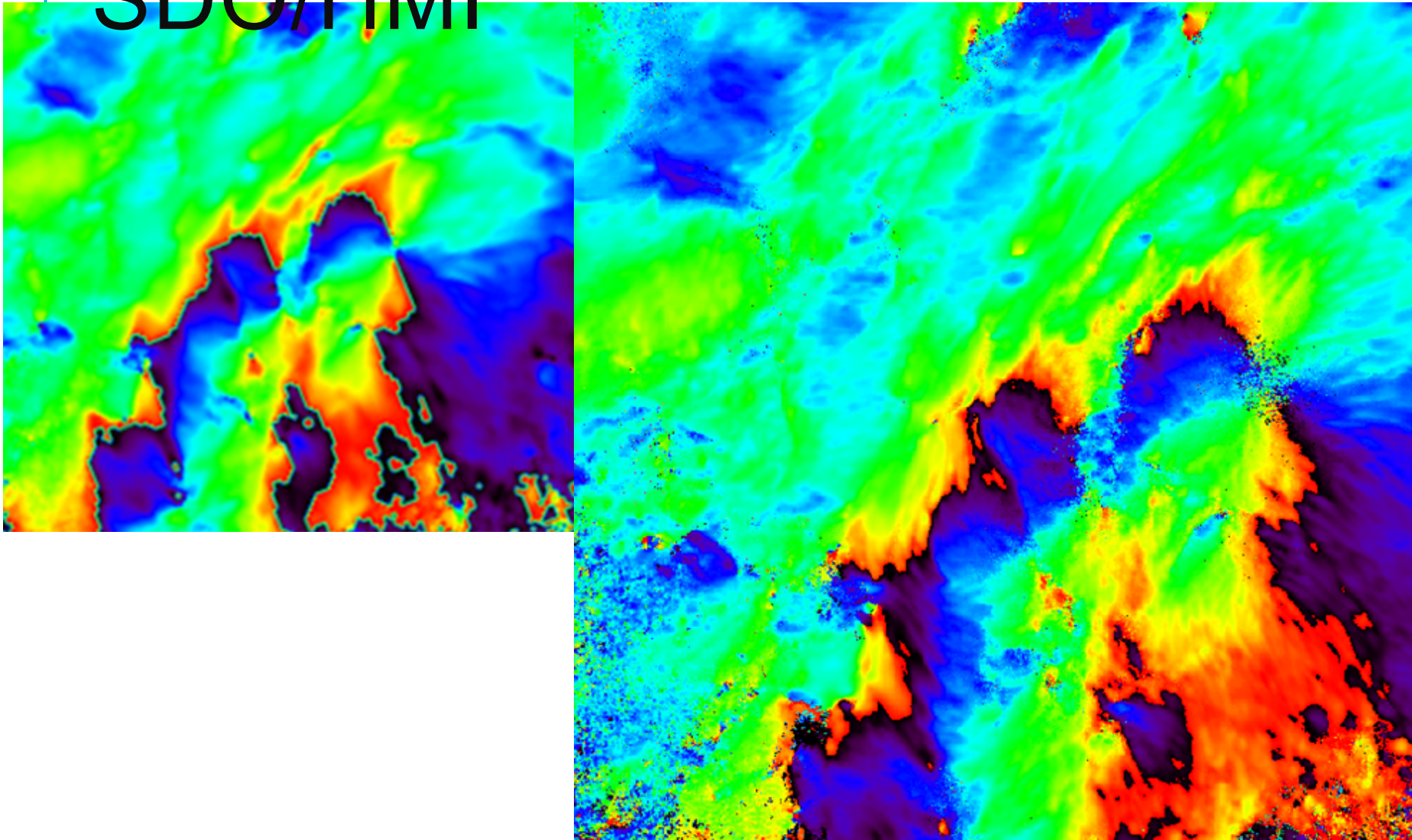


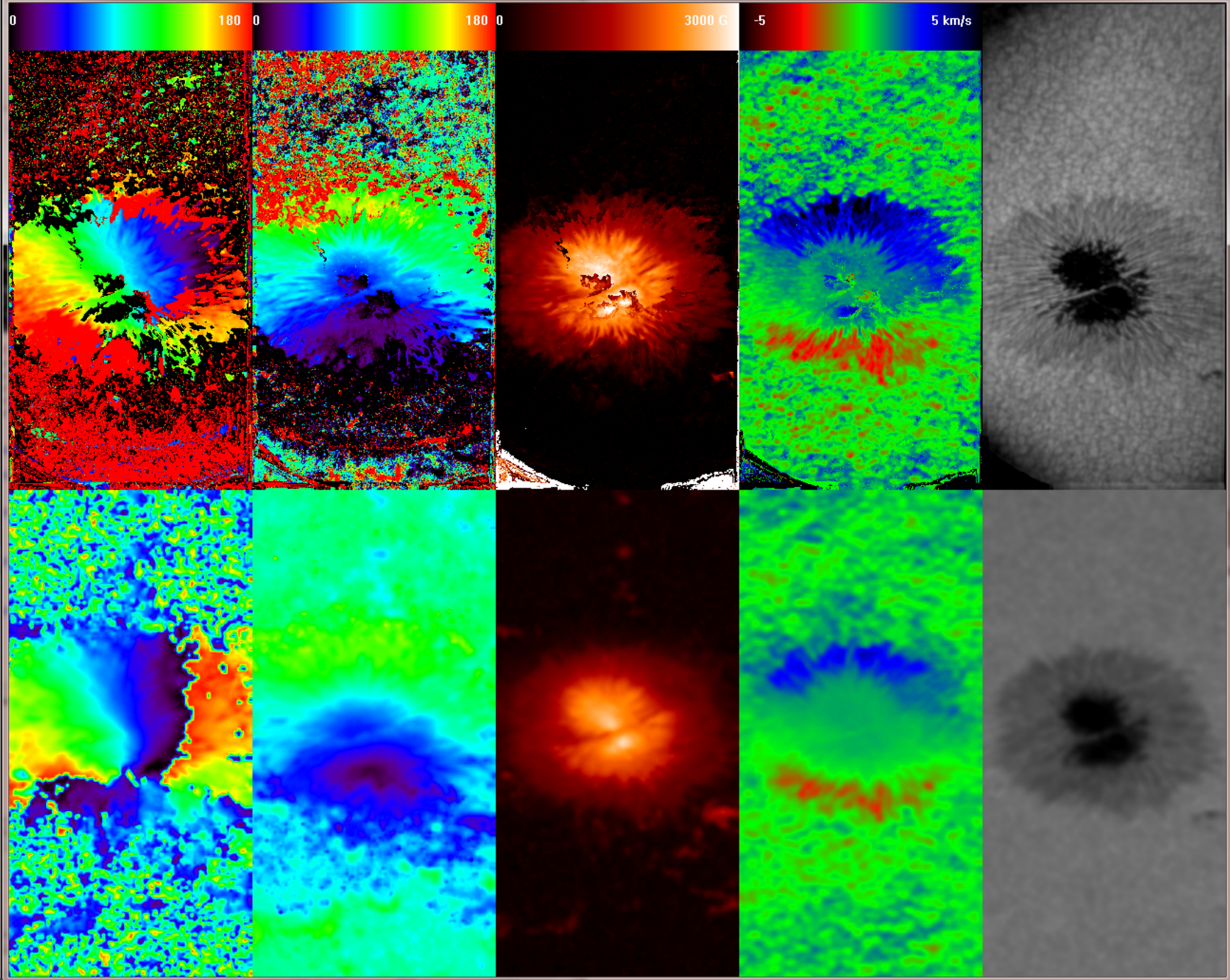
DOPPLER MAP

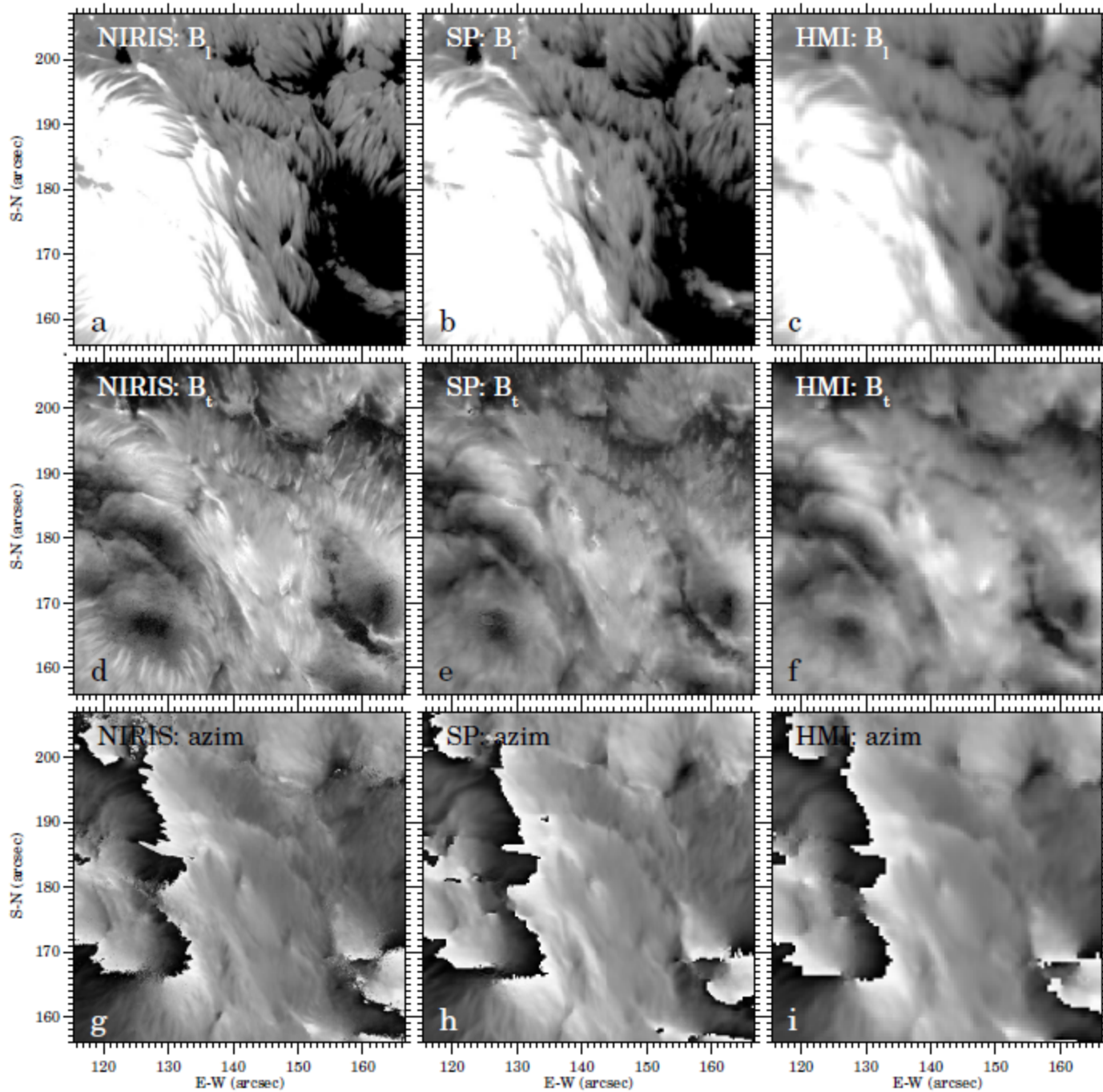
Chances for higher resolution velocity analysis



COMPARISON WITH SDO/HMI







Reasonable
Inversion
Outcome

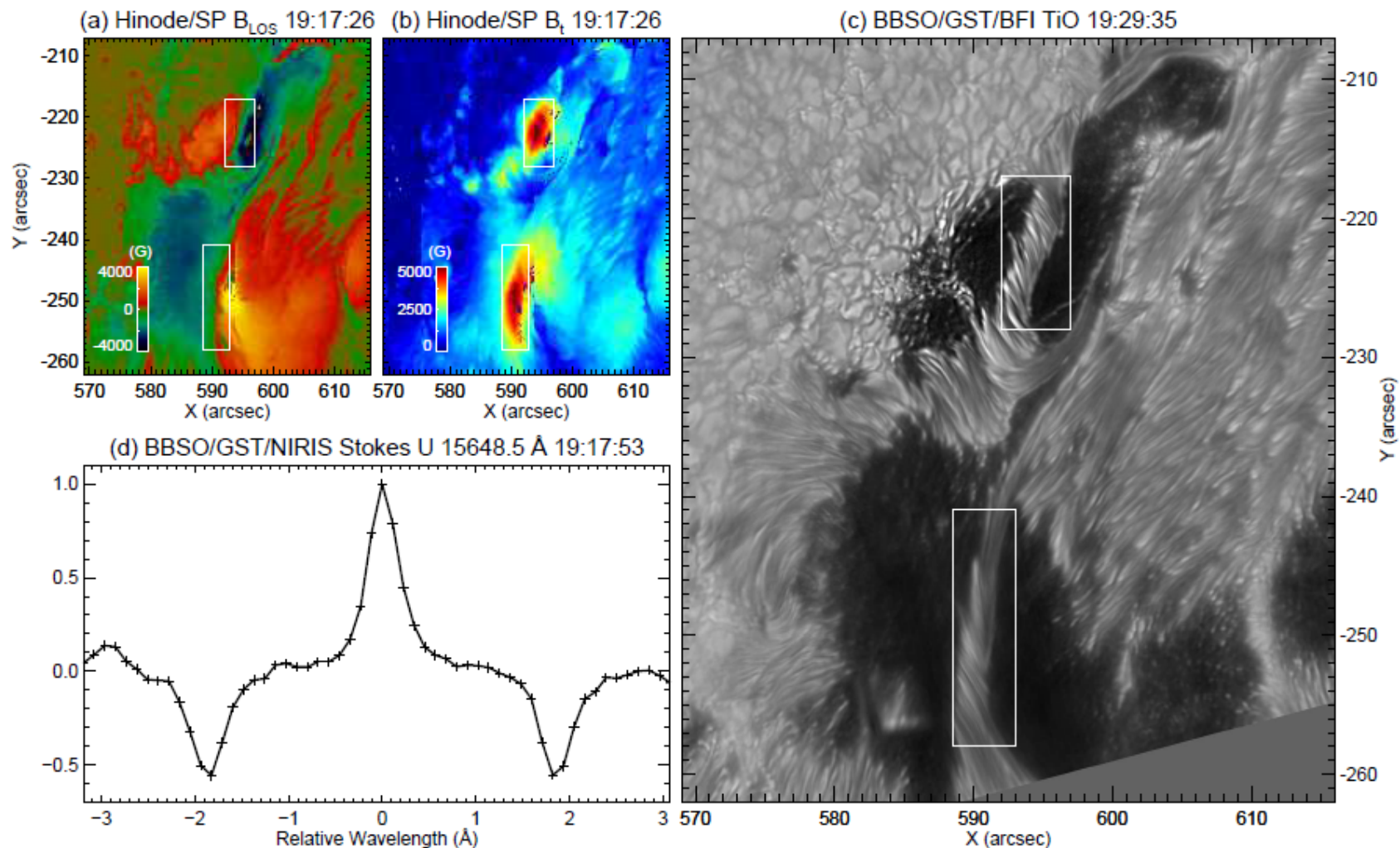






Fig. 1.— Unusual structures of AR 12673. (a) and (b) Hinode/SP LOS and transverse magnetic field strength. Note that in many pixels near the PIL, transverse fields are saturated at 5000 G. (c) BBSO/GST TiO image. The two white boxes in (a)–(c) mark the two strong transverse field areas at the PIL, where twisted photospheric LB structures of the δ configuration are present. (d) NIRIS Stokes U profile of a selected strong transverse field pixel at the PIL within the northern box. The direct measurement of Zeeman splitting yields a field strength of 5570 G.

Dark Structures in Sunspot Light Bridges

Jingwen Zhang¹, Hui Tian¹ , Sami K. Solanki^{2,3}, Haimin Wang^{4,5,6} , Hardi Peter², Kwangsu Ahn⁵, Yan Xu^{4,5,6}, Yingjie Zhu¹, Wenda Cao^{4,5,6}, Jiansen He¹ , and Linghua Wang¹ 

¹ School of Earth and Space Sciences, Peking University, 100871 Beijing, People's Republic of China; huitian@pku.edu.cn

² Max-Planck Institute for Solar System Research, Justus-von-Liebig-Weg 3, D-37077 Göttingen, Germany

³ School of Space Research, Kyung Hee University, Yongin, 446-701, Republic of Korea

⁴ Space Weather Research Laboratory, New Jersey Institute of Technology, University Heights, Newark, NJ 07102-1982, USA

⁵ Big Bear Observatory, New Jersey Institute of Technology, 40386 North Shore Lane, Big Bear City, CA 92314-9672, USA

⁶ Center for Solar-Terrestrial Research, New Jersey Institute of Technology, University Heights, Newark, NJ 07102-1982, USA

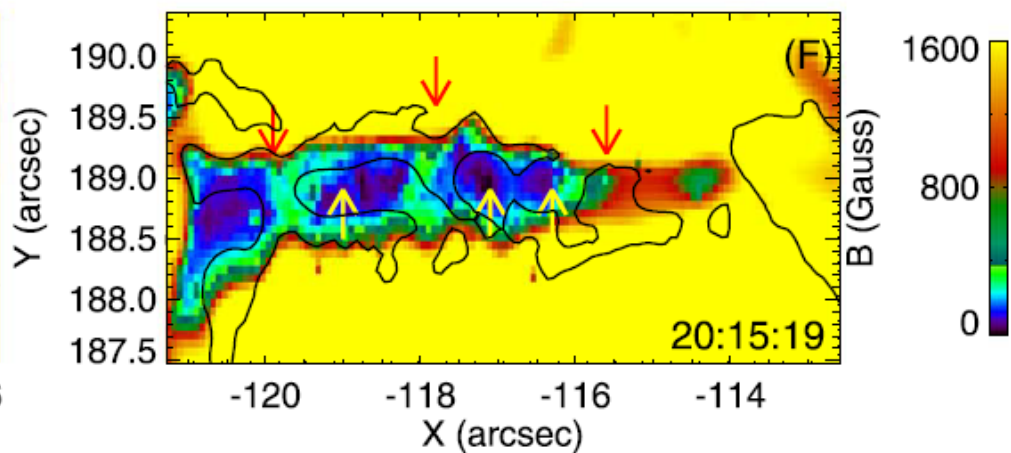
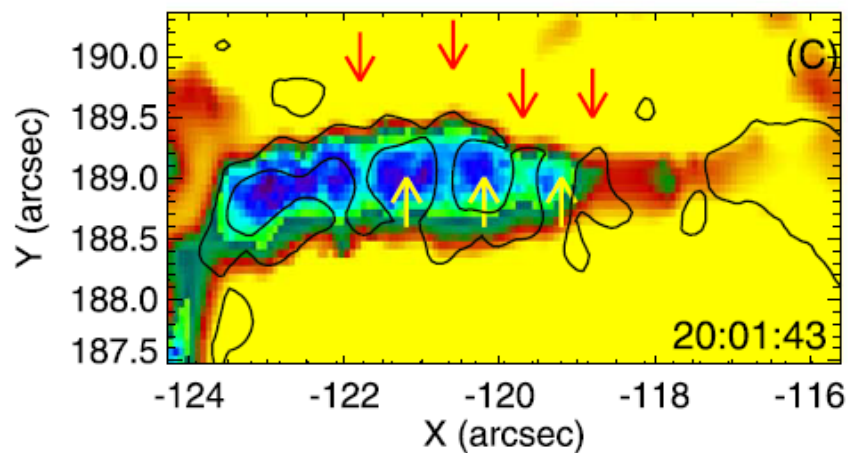
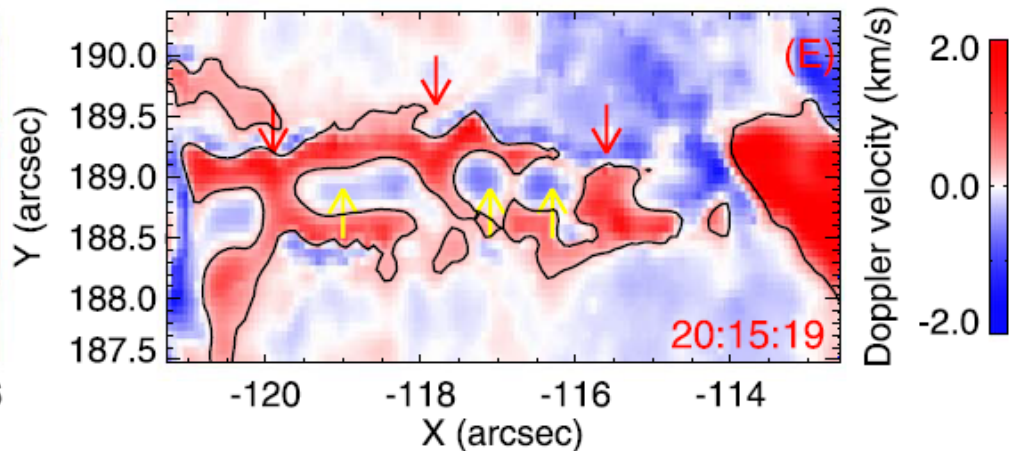
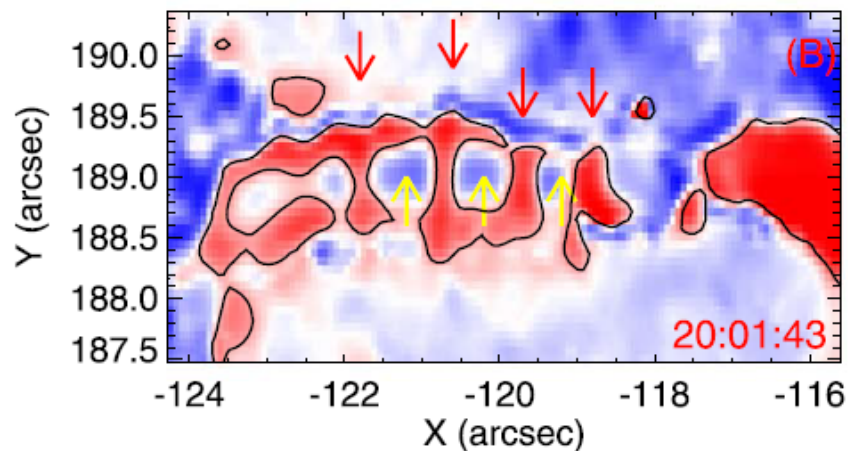
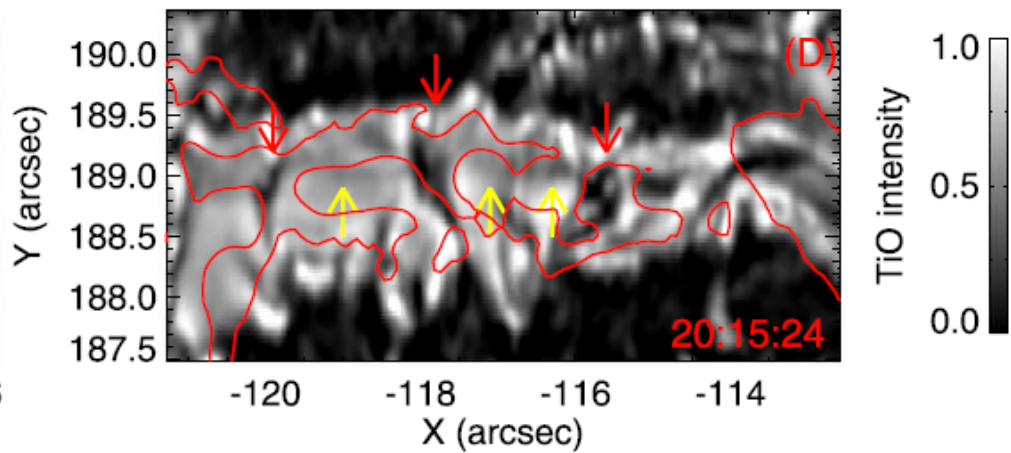
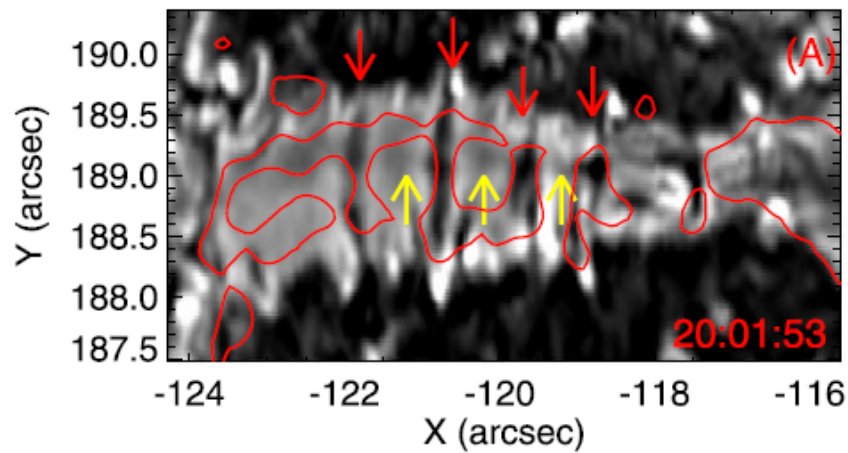
Received 2018 June 14; revised 2018 August 7; accepted 2018 August 11; published 2018 September 18

Abstract

We present unprecedented high-resolution TiO images and FeI 1565 nm spectropolarimetric data of two light bridges taken by the 1.6 m Goode Solar Telescope at Big Bear Solar Observatory. In the first light bridge (LB1), we find striking knot-like dark structures within the central dark lane. Many dark knots show migration away from the penumbra along the light bridge. The sizes, intensity depressions, and apparent speeds of their proper motion along the light bridges of 33 dark knots identified from the TiO images are mainly in the ranges of 80 ~ 200 km, 30% ~ 50%, and 0.3 ~ 1.2 km s⁻¹, respectively. In the second light bridge (LB2), a faint central dark lane and striking transverse intergranular lanes were observed. These intergranular lanes have sizes and intensity depressions comparable to those of the dark knots in LB1 and also migrate away from the penumbra at similar speeds. Our observations reveal that LB2 is made up of a chain of evolving convection cells, as indicated by patches of blueshift surrounded by narrow lanes of redshift. The central dark lane generally corresponds to blueshifts, supporting the previous suggestion of central dark lanes being the top parts of convection upflows. In contrast, the intergranular lanes are associated with redshifts and located at two sides of each convection cell. The magnetic fields are stronger in intergranular lanes than in the central dark lane. These results suggest that these intergranular lanes are manifestations of convergent convective downflows in the light bridge. We also provide evidence that the dark knots observed in LB1 may have a similar origin.

Key words: Sun: granulation – Sun: magnetic fields – Sun: photosphere – sunspots

Supporting material: animation



High-resolution observations of flare precursors in the low solar atmosphere

Haimin Wang^{1,2,3*}, Chang Liu^{1,2,3}, Kwangsu Ahn², Yan Xu^{1,2,3}, Ju Jing^{1,2,3}, Na Deng^{1,2,3}, Nengyi Huang^{1,2,3}, Rui Liu^{4,5}, Kanya Kusano⁶, Gregory D. Fleishman³, Dale E. Gary³ and Wenda Cao^{2,3*}

Solar flares are generally believed to be powered by free magnetic energy stored in the corona¹, but the build up of coronal energy alone may be insufficient to trigger the flare to occur². The flare onset mechanism is a critical but poorly understood problem, insights into which could be gained from small-scale energy releases known as precursors. These precursors are observed as small pre-flare brightenings in various wavelengths³⁻¹³ and also from certain small-scale magnetic configurations such as opposite-polarity fluxes¹⁴⁻¹⁶, where the magnetic orientation of small bipoles is opposite to that of the ambient main polarities. However, high-resolution observations of flare precursors together with the associated photospheric magnetic field dynamics are lacking. Here we study precursors of a flare using the unprecedented spatiotemporal resolution of the 1.6-m New Solar Telescope, complemented by new microwave data. Two episodes of precursor brightenings are initiated at a small-scale magnetic channel¹⁷⁻²⁰ (a form of opposite-polarity flux) with multiple polarity inversions and enhanced magnetic fluxes and currents, lying near the footpoints of sheared magnetic loops. Microwave spectra corroborate that these precursor emissions originate in the atmosphere. These results provide evidence of low-atmospheric small-scale energy release, possibly linked to the onset of the main flare.

The long-duration 22 June 2015 M6.5 flare occurred near the disk centre (8° W, 12° N) at NOAA active region 12371. Time profiles of flare emissions in different wavelengths (including hard X-ray, soft X-ray and microwave) clearly show that shortly before the flare impulsive phase starting from ~17:51 UT, there are two short episodes of smaller-magnitude emissions at ~17:24 UT and ~17:42 UT, which we denote as P1 and P2, respectively (see Supplementary Fig. 1). We find that these emissions can only stem from the active region of the imminent M6.5 flare, and that simultaneous H α brightenings are observed with NST in the flaring core region (see Supplementary Video 1). Thus they can be regarded as precursors of the M6.5 flare. Fine-structural evolution of the associated precursor brightenings in NST H α and the surface magnetic structure are presented in Fig. 1. Specifically, the brightening associated with the precursor episode P1 first appears as a kernel, P1a, in NST at 17:23:21 UT (also discernible in ultraviolet and extreme ultraviolet; see Supplementary Fig. 2a,d), then quickly turns into an elongated structure with another kernel, P1b (Fig. 1a and Supplementary Fig. 2b). Later, from ~17:38 UT, fine-scale brightening starts to be seen in the south and travels northeastward, apparently along the previously brightened regions in P1. The precursor episode P2 starts around 17:42 UT as kernel P2a (Fig. 1b), and then another, P2b, is formed in the south (Fig. 1c). All the above brightenings exhibit little propagation towards the east. From ~17:46 UT, one of the main flare rib-

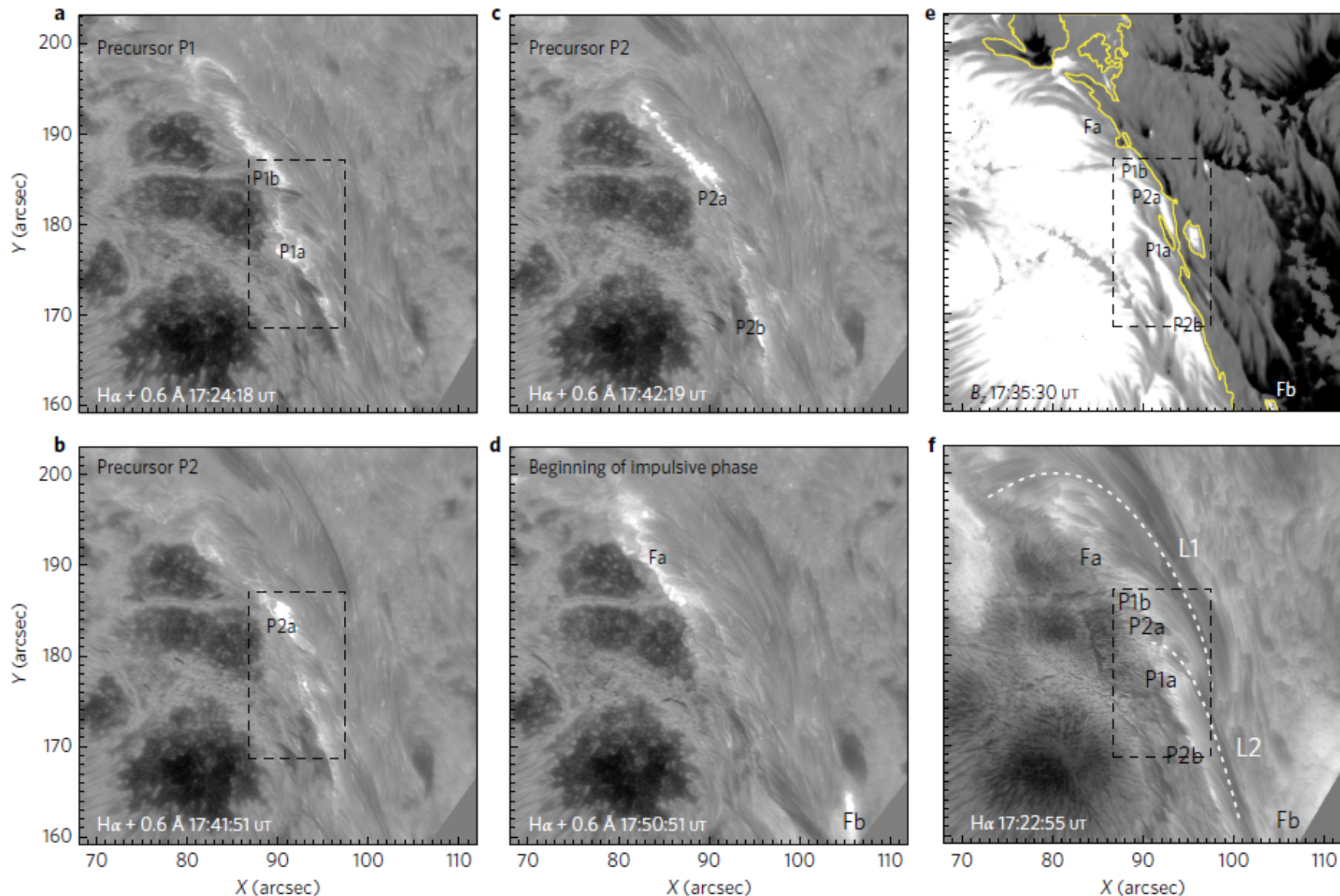




Figure 1 | Precursor brightenings. BBSO/NST chromospheric $H\alpha + 0.6 \text{ \AA}$ (a-d) and $H\alpha$ centre-line (f) images (in logarithmic greyscale) in comparison with NIRIS photospheric vertical magnetic field B_z (e; scaled between $\pm 1,500 \text{ G}$), showing the core region structure of the 22 June 2015 M6.5 flare. Brightenings labelled P1a/P1b, P2a/P2b and Fa/Fb appear during the precursor episodes P1, P2, and at the beginning of the flare impulsive phase, respectively, the timings of which are indicated in Supplementary Fig. 1. The dashed box in a, b, e and f denotes the field of view of Figs 2b and 3a-c. The yellow contour in e indicates the polarity inversion line. The dashed lines in f illustrate sheared arcade loops L1 and L2 (also see Supplementary Fig. 2e). All the images were registered with respect to 22 June 2015 17:24 UT.

High-resolution Observations of Flares in an Arch Filament System

Yingna Su^{1,2} , Rui Liu^{3,4} , Shangwei Li^{1,5}, Wenda Cao^{6,7}, Kwangsu Ahn⁶, and Haisheng Ji^{1,2}

¹ Key Laboratory of DMSA, Purple Mountain Observatory, Chinese Academy of Sciences, Nanjing 210008, People's Republic of China; ynsu@pmo.ac.cn

² School of Astronomy and Space Science, University of Science and Technology of China, Hefei, Anhui 230026, People's Republic of China

³ CAS Key Laboratory of Geospace Environment, Department of Geophysics and Planetary Sciences, University of Science and Technology of China, Hefei 230026, People's Republic of China; rliu@ustc.edu.cn

⁴ Collaborative Innovation Center of Astronautical Science and Technology, Hefei 230026, People's Republic of China

⁵ University of CAS, Beijing 100049, People's Republic of China

⁶ Big Bear Solar Observatory, New Jersey Institute of Technology, 40386 North Shore Lane, Big Bear City, California 92314-9672, USA

⁷ Center for Solar-Terrestrial Research, New Jersey Institute of Technology, University Heights, Newark, New Jersey 07102-1982, USA

Received 2017 June 11; revised 2018 January 18; accepted 2018 January 28; published 2018 MM DD

Abstract

We study five sequential solar flares (SOL2015-08-07) occurring in Active Region 12396 observed with the Goode Solar Telescope (GST) at the **Big Bear Solar Observatory**, complemented by *Interface Region Imaging Spectrograph* and *SDO* observations. The main flaring region is an arch filament system (AFS) consisting of multiple bundles of dark filament threads enclosed by **semicircular** flare ribbons. We study the magnetic configuration and evolution of the active region by constructing coronal magnetic field models based on *SDO/HMI* magnetograms using two independent methods, i.e., the nonlinear force-free field (NLFFF) extrapolation and the flux rope insertion method. The models consist of multiple flux ropes with mixed signs of helicity, i.e., positive (negative) in the northern (southern) region, which is consistent with the GST observations of multiple filament bundles. The footprints of quasi-separatrix layers (QSLs) derived from the extrapolated NLFFF compare favorably with the observed flare ribbons. An interesting double-ribbon fine structure located at the east border of the AFS is consistent with the fine structure of the QSL's footprint. Moreover, magnetic field lines traced along the **semicircular** footprint of a dome-like QSL surrounding the AFS are connected to the regions of significant helicity and Poynting flux injection. The maps of magnetic twist show that positive twist became dominant as time progressed, which is consistent with the injection of positive helicity before the flares. We hence conclude that these circular shaped flares are caused by 3D magnetic reconnection at the QSLs associated with the AFS possessing mixed signs of helicity.

Key words: Sun: chromosphere – Sun: corona – Sun: evolution – Sun: filaments, prominences – Sun: flares – Sun: magnetic fields

Supporting material: animations

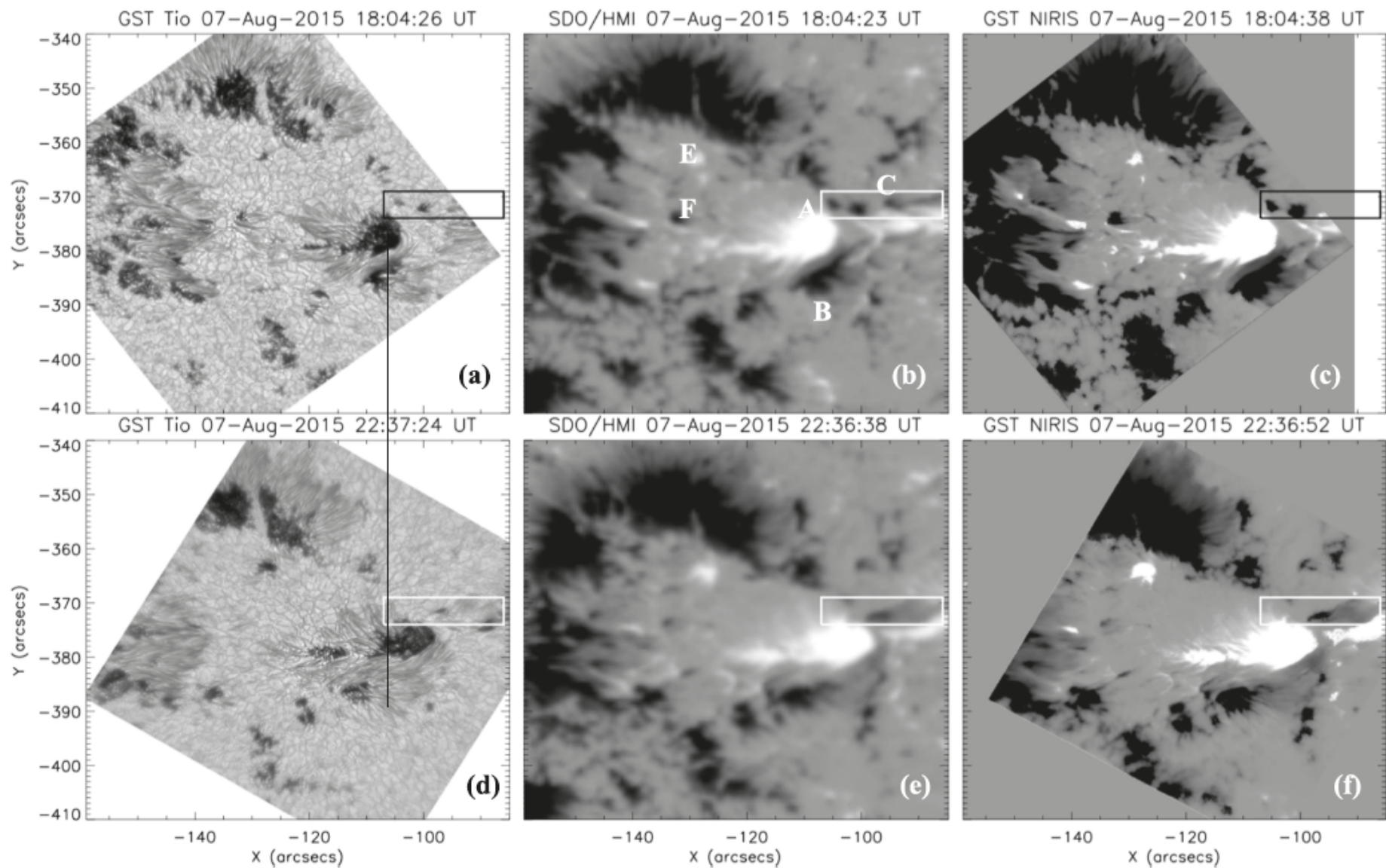

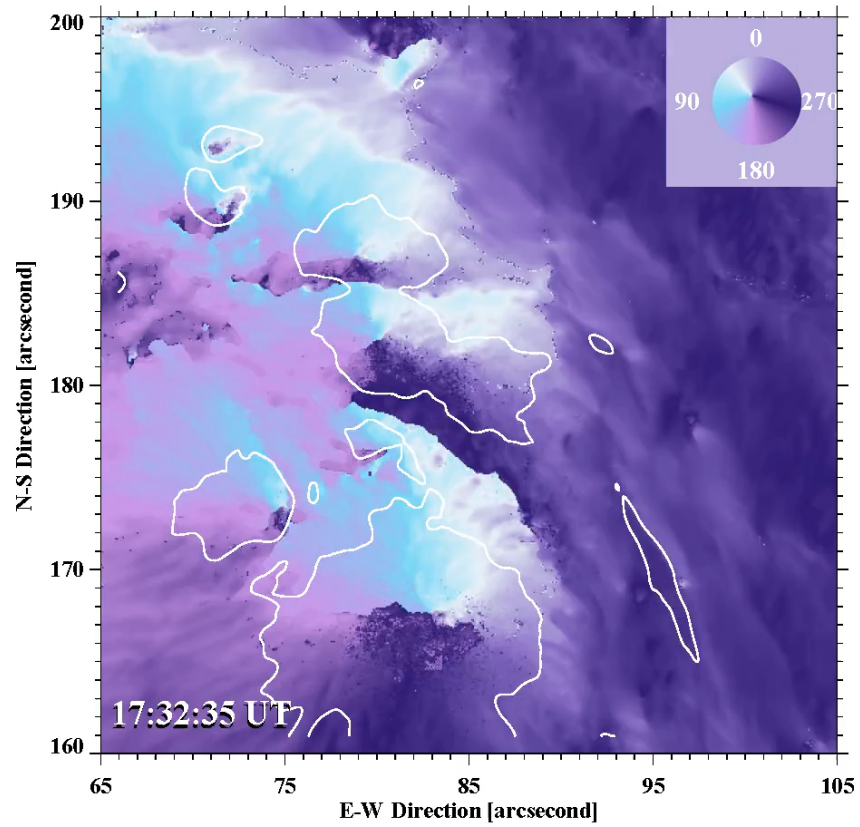


Figure 9. GST/TiO images (first column) and photospheric magnetograms observed by HMI (second column) and GST (third column) at 18:04 UT (top row) and 22:36 UT (bottom row). Significant flux cancellations occur in the region enclosed by black and white boxes.

Transient rotation of photospheric vector magnetic fields associated with a solar flare

Yan Xu^{1,2,3}, Wenda Cao^{2,3}, Kwangsu Ahn², Ju Jing^{1,2,3}, Chang Liu ^{1,2,3}, Jongchul Chae⁴, Nengyi Huang^{1,3}, Na Deng^{1,2,3}, Dale E. Gary³ & Haimin Wang^{1,2,3}

As one of the most violent eruptions on the Sun, flares are believed to be powered by magnetic reconnection. The fundamental physics involving the release, transfer, and deposition of energy have been studied extensively. Taking advantage of the unprecedented resolution provided by the 1.6 m Goode Solar Telescope, here, we show a sudden rotation of vector magnetic fields, about 12–20° counterclockwise, associated with a flare. Unlike the permanent changes reported previously, the azimuth-angle change is transient and cospatial/temporal with H α emission. The measured azimuth angle becomes closer to that in potential fields suggesting untwist of flare loops. The magnetograms were obtained in the near infrared at 1.56 μm , which is minimally affected by flare emission and no intensity profile change was detected. We believe that these transient changes are real and discuss the possible explanations in which the high-energy electron beams or Alfvén waves play a crucial role.



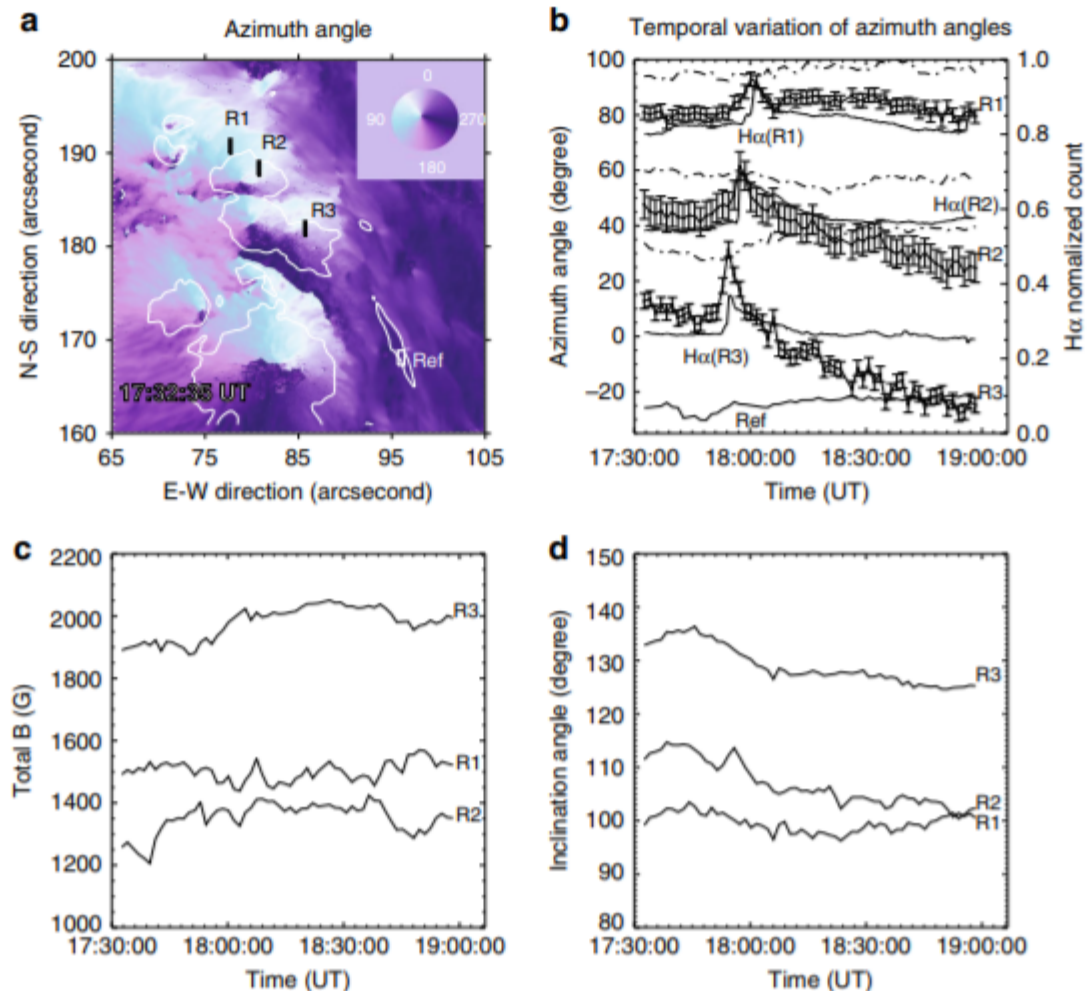


Fig. 3 Temporal evolution of azimuth angle deviation. **a** Azimuth angle map taken before the flare at 17:32:35 UT. Three slits are put on the regions of interest (R1-3), plus a reference region in the lower right corner. The white contours outline the sunspot umbral areas (>1800 G). **b** The curves with error bars are the temporal variation of averaged azimuth angle within regions of R1-3. The uncertainties are estimated using the standard deviation of the preflare data points. The peaks are more than three times of the uncertainties rendering themselves statistically significant. The flare time is determined by the H α light curve, for instance, the dashed line is the H α light curve of R3, in which the peak matches with azimuth angle peak in R3. All H α light curves are in natural log space and self-normalized to their peak emission. In the bottom, the temporal variation of the azimuth angle in the reference region is plotted, which is manually increased by 50° to match the plotting range ($50\text{--}190^\circ$). The dotted-dash curves are the azimuth angles of extrapolated potential fields that remain certain levels above the azimuth angles of real fields. **c** Temporal variation of averaged magnetic flux strength within the representative areas. **d** Temporal variation of averaged inclination within the representative areas

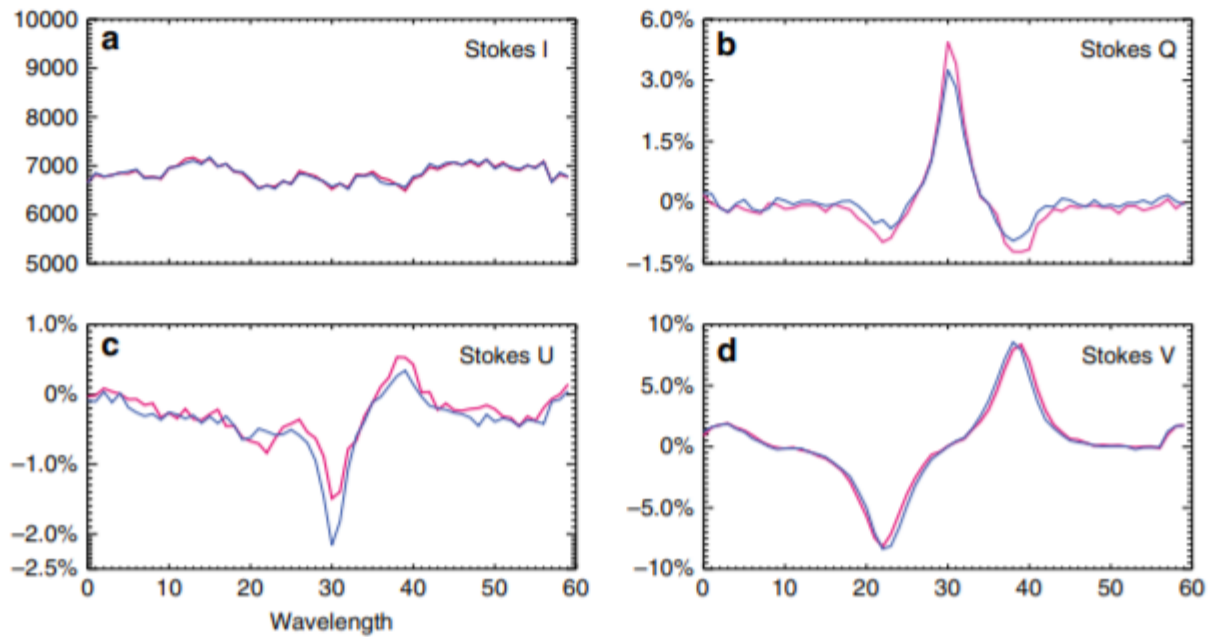


Fig. 5 Stokes profiles before and during the flare. Stokes components (I, Q, U, and V) taken near R3 before (blue) and during (pink) the flare. **a** Stokes I. **b** Stokes Q. **c** Stokes U. **d** Stokes V. It is clear that the Stokes I and V components remain almost unchanged but Q and U components are significantly affected during the flare

FUTURE PLAN

SIR inversion code for more scrutinized analysis of the magnetic fields

Machine learning for inversion for better accuracy and scaling with high processing speed

10830 polarimetry will be operational next summer

An aerial photograph of a winding road through a forested landscape. The road curves through a dense forest of evergreen trees. In the background, a large body of water, likely a lake or reservoir, is visible, surrounded by more forested hills. The entire image has a blue tint. The text 'THANK YOU!' is overlaid in white, bold, sans-serif font in the upper left quadrant.

THANK YOU!